Clausthal University of Technology
Institute of Geo-Engineering

Proof of a locally limited imperfection of the diaphragm wall based on the numerical method Smoothed-Particle Hydrodynamics (SPH)

DISSERTATION

to be awarded the degree
Doctor of Engineering (Dr.-Ing.)

Submitted by
M.Sc. Iman Zanganeh
from Mashhad, Iran

Approved by the Faculty of Energy and Economic Sciences,
Clausthal University of Technology,

Date of oral examination
14.12.2022

Dekan
Prof. Dr. mont. Leonhard Ganzer

Vorsitzende/Vorsitzender der Promotionskommission:

Betreuer
Prof. Dr.-Ing. Norbert Meyer

Gutachterin
Prof. Dr.-Ing. habil. Eleni Gerolymatou

Acknowledgements

Above all, I am grateful to God for providing me the opportunity, health and ability to accomplish this research.

I would like to express my greatest gratitude to my supervisor, Professor Dr.-Ing. Norbert Meyer for his support and trust on my work. Also, I would like to thank Dr.-Ing. Ansgar Emersleben.

A particular thank to my parents and my family, without all of them my life simply didn't have any sense. They remember me every day how lucky I am.

Dedicated to my wife Asieh and my daughter Ronia.
Their smiles remind me to always keep doing what I
love and never give up on my dreams.

Abstract

Due to the insufficient space to construct new facilities and tall buildings in the developing cities, it is required to use the underground space vastly. In the planning and executing a construction in underground space, deep excavation and deep foundation play an important role, specially in the areas with high groundwater level and limited construction's site by reason of the densely built-up neighboring buildings.

Many different retaining systems are developed over time. They are appropriate für various type of soil material and different ground water level as well as various boundary conditions. One of the most common retaining systems to construct deep foundations are diaphragm walls. They are constructed as reinforced concrete wall. Their advantages as watertightness, high stability and sufficient stiffness, great load bearing capacity, design depth up to 100 m, construction possibility in various type of soil and in different shapes as well as the low long-term movement and less noise and vibration are the main reasons that diaphragm walls are one of the popular and common system to construct deep foundations.

Despite of the many advantages, the construction of the diaphragm walls requires many attentions and continuous controlling. Many damages are appeared every year because of the mistaking in designing, lack of the knowledge of tremie method and/or insufficient quality control during and after the constructions. The collapse of the Cologne Archive and the accident at the underground metro line U2 in Berlin are two catastrophic event in Germany.

In this dissertation, the imperfections of diaphragm walls are investigated and numerically simulated. The simulation is carried out based on a numerical method "Smoothed Particle Hydrodynamics (SPH)". The SPH method is a meshfree method, which is originally invented for numerical simulation of the astronomical problems. This method is also often applied in the last decade in the geotechnical problems, especially the problems with large

deformations, which are very difficult and complicated to simulate in the conventional grid-based methods as like as Finite Element method.

In this research, a Fortran-Code for simulation of the imperfections in diaphragm walls with SPH method is developed. To validate this code, various geotechnic problems are modelled and the results compared with the different known experiments.

Furthermore, an Experiment is carried out earlier in the Institute of Geo-Engineering in Technical University of Clausthal in order to observe the collapse of the historical archive building of the city Cologne in Germany. This experiment is also simulated, to present the capabilities of the SPH method for simulating the imperfections in diaphragm walls even with high groundwater level.

Contents

List of Figures

List of Tables

1 Introduction

Continuous developing the big cities and lack of the space to construct the required Infrastructure, transport systems, tall buildings, etc. is the main reason to increase the use of the underground space immensely. Nowadays, the depth of the used space can be up to 100 m. Constructing in such depth needs a special planning and execution methods, particularly by retaining systems. Retaining systems play an important role in constructing deep constructions, since they are the main element to retain against soil and groundwater pressure in the excavation pit.

They are many different types of retaining systems, which are applied in various projects with different situations. From all these retaining systems, diaphragm wall is one of the common systems, which is utilized in many projects yearly. This system has a lot of advantages and is suitable for constructing in various types of soils and high groundwater level. In spite of all praiseworthy advantages, many damages are happened by the reason of defects in diaphragm walls. The collapse of the Cologne Archive and the accident at the underground metro line U2 in Berlin are two famous instances in Germany. As a result, the Quality control during the constructions and testing the completed works prior to commencement of excavation are the essential steps to prevent the imperfections and defects in diaphragm walls.

Insignificant imperfections are normally occurred by the construction of diaphragm walls. In such cases, it should be decided about the status of the imperfections. An important

task in the construction's site is to decide, which imperfections is a defect and whether a repairing work is required. In order to support the assessment in such situations, applying of the numerical methods is prevalent.

Numerical methods have developed increasingly in the last decades. Nowadays the simulation of very complicated problems can easily perform with the help of powerful computers. Numerical simulations are the best alternative to the experiments. Experiments can be done only for some limited situations, but a wide spectrum of situations can be investigated in numerical modeling. Furthermore, it is possible to measure different parameters in the computational simulations, which are impossible or dangerous in the experiments.

In order to prove a new theory and appropriate simulation, the model must be validated. To validate the theories for a new phenomenon, a simple experiment should be carried out primarily. After that, the problem should be simulated with numerical methods. With comparing the results of experiments, Simulations and theoretical solutions, the accuracy of the developed simulation's methods can be estimated. If the difference between results is significant, the applied approach has to be corrected. In this case, the process will be repeated till when the resulting error by simulation is very low and acceptable. Thereafter, the developed method can be utilized to simulate the complicated problems. The Figure 1.1 shows the relation between theories, Simulations and experiments (Liu & Liu, 2003).

The numerical methods can be divided into two groups. The first group are the grid-based methods. All the famous traditional methods like Finite Difference Methods (FDM), Finite Element Method (FEM), Finite Volume Method (FVM), etc. are Mesh-Based methods, which a suitable Mesh generation at the beginning of the calculation is necessary. Such methods are suitable for many applications. But applying the grid-based method for the problems with large deformations, variable boundaries etc. are very difficult. However, some technics for remeshing has been developed to overcome this problem, but the implementation of such algorithms is complicated.

The second groups of numerical methods are called meshfree or meshless methods, which recently applied in many problems with large deformation and post-failure. Due to the lack of the grid in meshfree methods, simulating of models with complicated geometry and large deformations are without much effort possible.

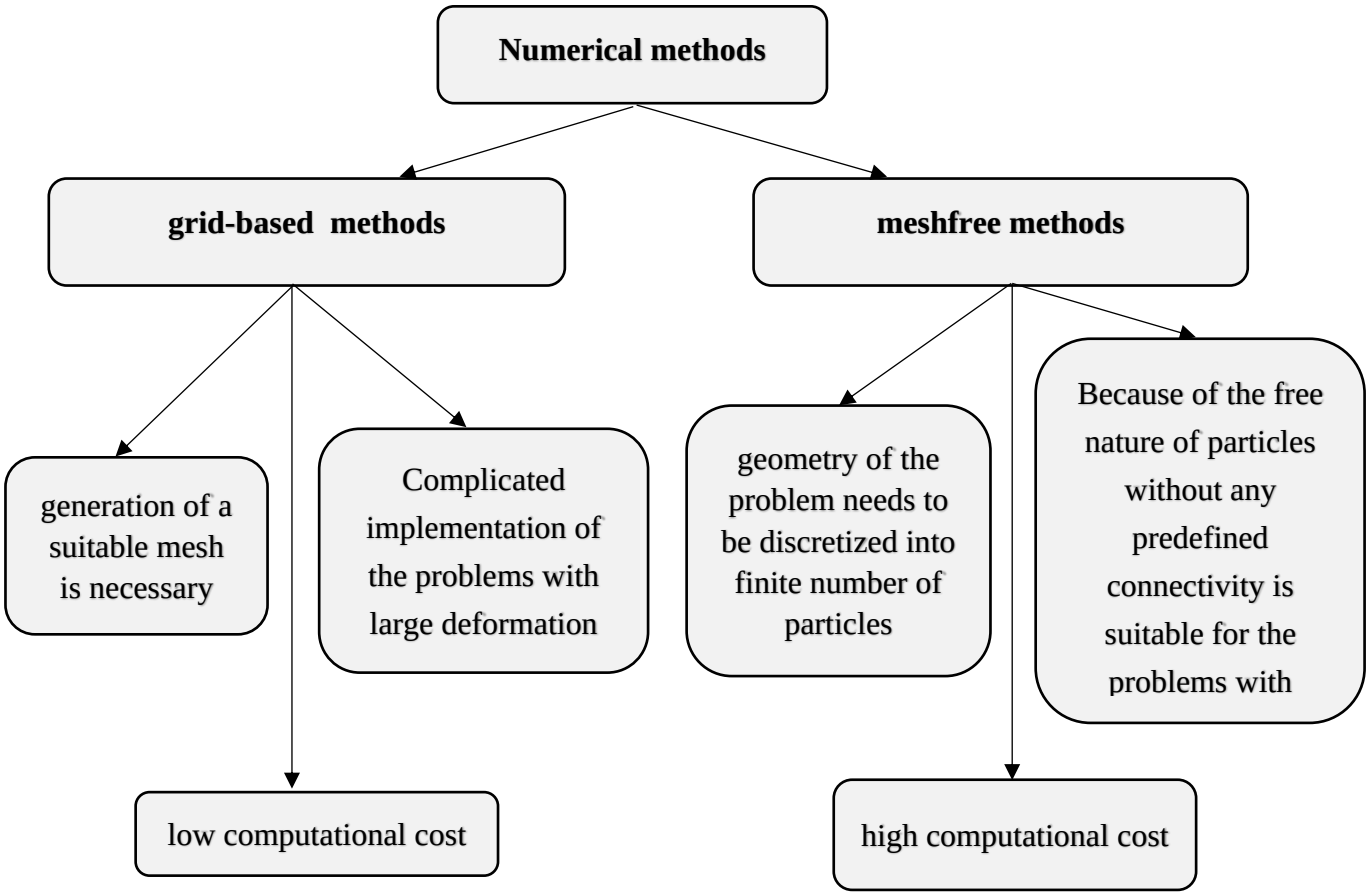

Figure 1.1: Numerical methods, grid-based methods and meshfree methods

For many years, the grid-based Finite Element Method used as a standard numerical method to simulate geotechnical problems. In the last two decades, many researchers tried to use the popular meshless method “Smoothed Particle Hydrodynamics” for solving geotechnical problems. The previous researches show the ability of this meshless method to simulate problem in this field, especially the problems with large deformation and post-failure. Another main advantage of SPH method over FEM method is the ability to

simulate discontinuous soil failure and modelling the entire slope failure process (Bui H. , Fukagawa, Sako, & Wells, 2011).

In the present research, the ability of the SPH-method in the Simulation of geotechnical problems was proved. For this reason, a Fortran-Code is based on the meshless numerical method SPH developed and validated by comparing the results of numerical simulation with some benchmark experiments as failure process of granular material in different forms, collapse of a water-saturated granular column into water and hydraulic heave. In this way, the numerical algorithm was validated firstly. After that, several famous geotechnical problems as Failure process of the granular material in a Silo, water jet, two-sided slope embankment are simulated and the results are observed. At the end of the research, the imperfections of the diaphragm wall in Cologne in Germany, which caused the collapse of the Cologne Archive in 2009 (see Figure 1.2), is investigated. The simulation and validation of the modelling of this problem is done based on the experiments, which earlier were carried out in Institute of Geo-Engineering in Technical University of Clausthal.

Figure 1.2: Collapse of the Cologne's historical archives (www.stadt-koeln.de, 2009), ©Stadt Köln/Jürgen Schütze

2 Deep foundation excavation

2.1 General

Todays, the big cities developing rapidly and therefore, it is needed to utilize the underground space for different purposes, e.g., constructions of tall buildings with underground parking lots, underground transport system, etc. They are specially required for excavation in areas with high groundwater level and limited construction's site, closely to the neighbouring buildings. Because of the complexity of such projects, many case studies carried out about the planning, execution methods as well as the imperfections and defects of the deep foundations in recent years (Chai, Ni, Ding, Qiao, & Lu, 2021), (Alipour & Eslami, 2019), (You, Yan, Xu, Liu, & Che, 2018), (Calin, Radu, & Bica, 2017), (Tomczak & Mielczarek, 2016), (Mangushev, Rybnov, Lashkova, & Osokin, 2016), (Weng, Xu, Wu, & Liu, 2016).

Diaphragm walls are one of the most common retaining systems for deep excavations. They can be constructed mostly deeper than other often methods. Furthermore, generally less noise and vibration are produced by constructing diaphragm walls. They are used mostly as foundation walls, dam cut-off walls, retaining walls or quayside wall. They are also an ideal solution in top-down construction method (www.sb-canada.com, n.d.).

In the following, the construction methods of diaphragm walls as well as the occurred imperfections are described. Furthermore, the methods to control the quality of diaphragm walls during and after the construction are presented.

2.2 Diaphragm wall

Diaphragm walls are commonly used in the deep excavation in the cities. They are constructed as reinforced concrete. This approach is especially appropriate for the regions with high groundwater level. The construction of the diaphragm walls is a low-noise and low-vibration procedure. In this method, the Walls can be built close to the boundary of the construction's site (Boley, 2019).

Moreover, in order to support the open trench during the construction's time, the trench is filled with bentonite temporarily (Schneider, 2013).

The diaphragm walls provide many advantages as below (www.sb-canada.com, n.d.):

- They meet all requirements for a deep construction pit as earth retention, load bearing foundation and watertightness.
- With this technique, it can be reached more depth and thickness than another method as Secant piled walls or Caisson. The design depth can be up to 100 m. The thickness can be varied from 0.50 – 3.20 m.
- Diaphragm walls can be built in different type of soil.
- They can be constructed in different shape.
- The long-term movement of the diaphragm walls are low

2.2.1 Construction

The construction of the diaphragm wall is a complicated task and requires special knowledge and experience. Moreover, it should be planned in advance, in which sequence the panels should be constructed. In the following, the typical sequence of work for building the diaphragm walls are listed as follows (https://railsystem.net, n.d.), (www.sb-canada.com, n.d.), (https://www.geotech.net.au, n.d.):

- Construction of the guide wall to control panel alignment.
- Excavation to form the diaphragm wall trench.
- Pumping bentonite or polymer slurry into the trench to support the trench from collapse.
- Install required stop-ends between neighboring panels.
- Lowering of the reinforcement cage in the trench.
- Pouring concrete in the trench and simultaneously collecting the bentonite mixture in a tank on the ground surface.

These steps are repeated to construct each panel. With building successive panels side by side, the continuous diaphragm wall is constructed.

They are various techniques to construct the panels of the diaphragm walls, especially in choosing the sequence of constructing panels. In the following figure 2.1, the different steps to construct the diaphragm walls (work steps) are shown.

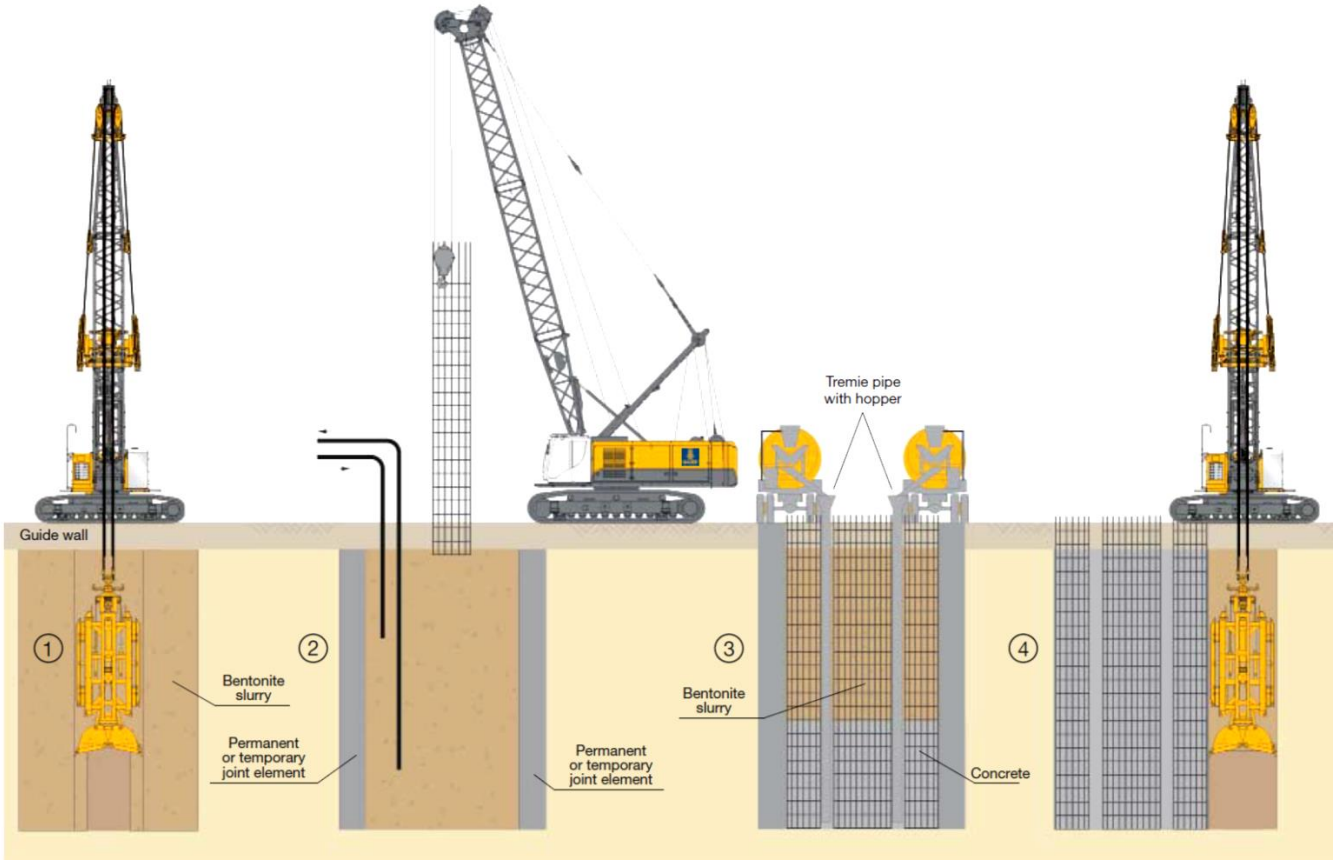

Figure 2.1: Work steps to manufacturing Diaphragm walls (reprint from (https://video.bauer.de, n.d.)).

The excavation of the trench for construction of the diaphragm walls are carried out in most soils and very weak rocks with cutter wheels, mechanical or hydraulic grab (www.balfourbeatty.com, n.d.).

The hydraulic grab is more preferred, because they produce lower noise and less vibration than mechanical grabs (https://bauerfoundations.com, n.d.). Moreover, the hydraulic grabs are faster and more precision. It should be mentioned, that hydraulic grabs are more expensive and they need more maintenance than mechanical grabs (https://www.eiengineering.com.au, n.d.).

In the Figure 2.2, the most used excavation grabs are shown.

(www.model-co.com, n.d.)

(www.bauer.de, n.d.)

Figure 2.2: Mechanical grab (left) and hydraulic grab (right) for excavation of Diaphragm walls

For excavation in very hard and dense soils or strong rock, it is required to employ hydromill system (www.balfourbeatty.com, n.d.). Application of Hydromill has noticeable advantages over using common grabs (www.brasfond.com, n.d.), (https://www.liebherr.com, n.d.):

- The system can be applied for very deep excavation up to 120 m.
- Excavation in very high strength rocks is possible.
- Hydromill can work continuously during the excavation, in contrast to grabs
- Continuous alignment of the Hydromill in the trench

In the following Figure 2.3, the Hydromill system is represented:

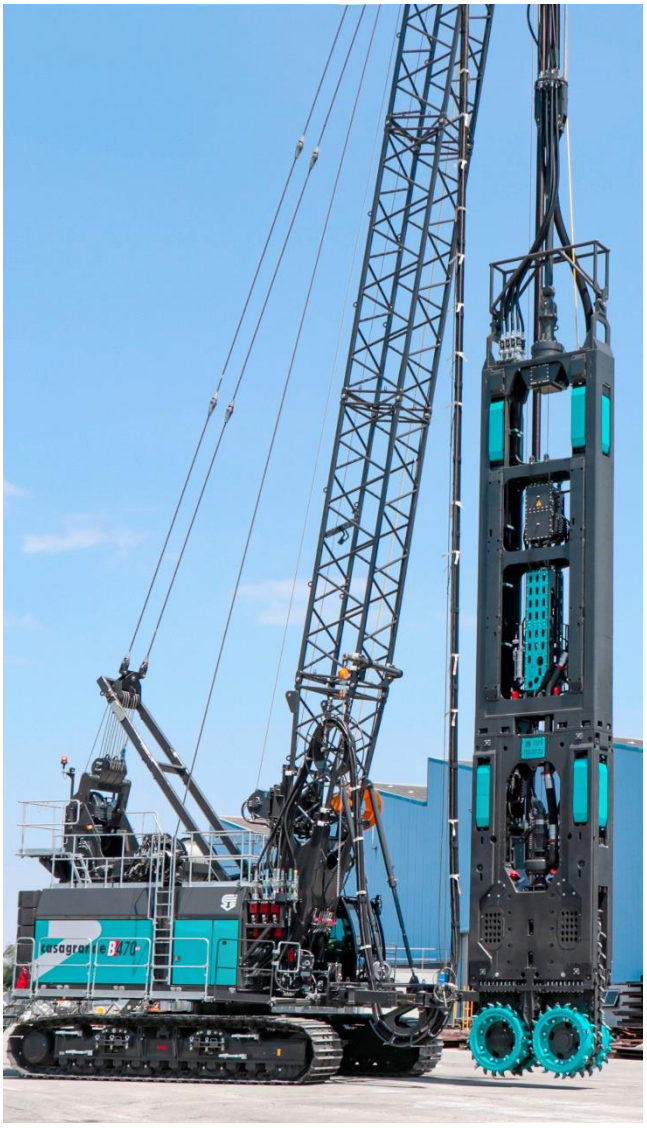

(www.casagrandegroup.com, n.d.)

(www.bauer.de, n.d.)

Figure 2.3: Hydromill system

In order to interlock the panels to form a continuous diaphragm wall, joint elements are used between the panels. These elements are installed during the construction of the primary panels (Schneider, 2013).

These joint elements can be divided into two groups (www.jointinspector.com, n.d.):

- Reusable end-stops: They are the common form of the joint element in the constructions of the diaphragm walls. They are removed after the construction of the primary panels.
- Lost End-stop: They are not needed to pull out after the construction. They are remained in the wall permanently after the construction. The lost joint element can be made from steel or pre-cast elements.

In the figure 2.4 some common joint elements are presented (Schneider, 2013):

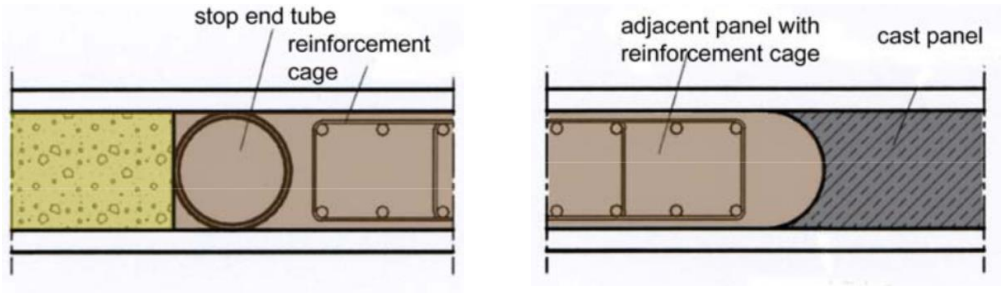

stop end – stop end tube

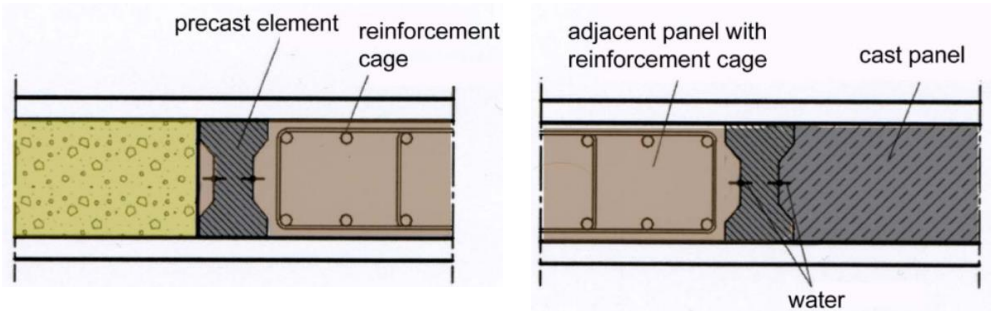

stop end – precast element

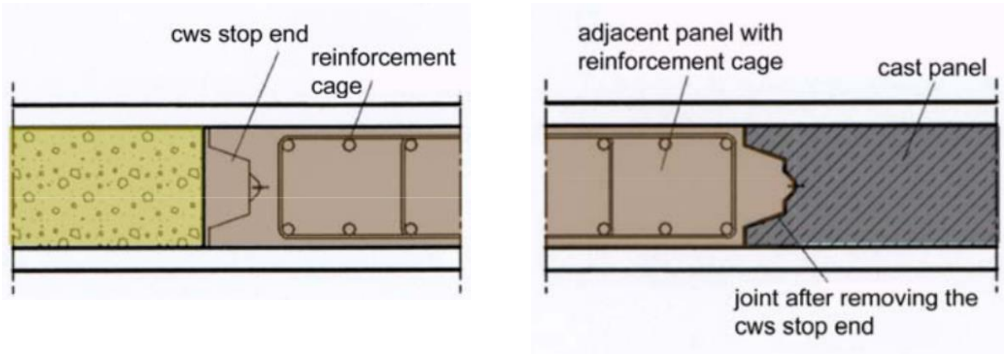

stop end – CWS stop end

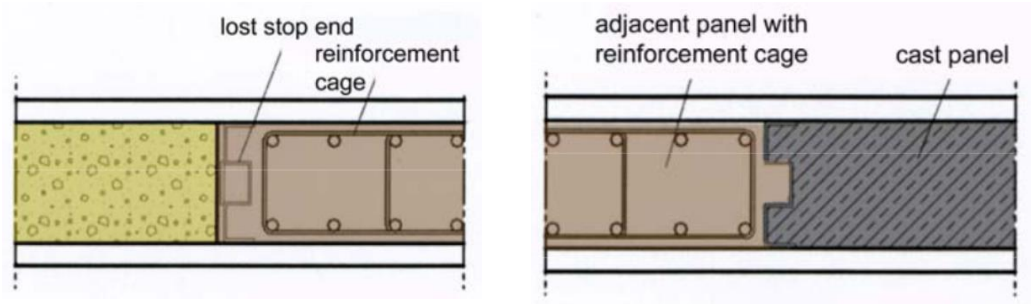

stop end – lost steel joint

Figure 2.4: Some common joint elements in diaphragm walls (reprint from (Schneider, 2013)).

To pouring the concrete in the trench, the tremie technique is used. Before the commencement of pouring concrete, it should be controlled, whether the base of the excavation is free of loose debris (EFFC/DFI Guide, 2018). By the concreting with the tremie technique, the dip tube will be used and it will begin to concrete from the bottom of the panel excavation. The great difficulty is pushing the bentonite upwards during the whole time of the concreting in the entire width of the panel (El Zein, Vanhove, Djelal, Madec, & Gotteland, 2021). The process of the placing concrete in diaphragm wall is in the following figure 2.5 schematic presented:

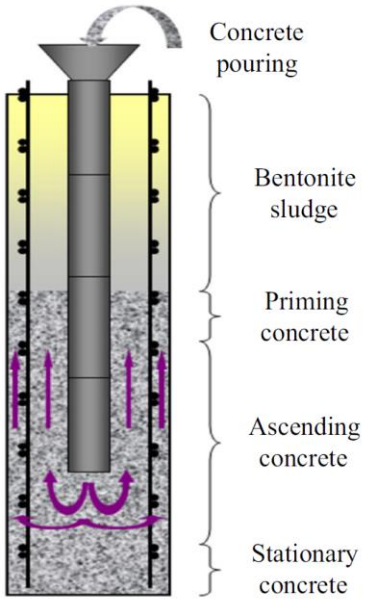

Figure 2.5: Schematic representation of the concrete casting in diaphragm walls (reprint from (El Zein, Vanhove, Djelal, Madec, & Gotteland, 2021)).

Prior to beginning of the implementation, it is recommended to implement one or more full-scale test elements. The time and cost of constructing the full-scale trials have to be scheduled in the tender documents, so that the appointed Constructor will build the Trials before the beginning the real work. To construct the Trials, it should be noted that the same technique, materials and instrument have to be utilized as intended for the permanent work. The construction of Trials prior to the main work can avoid many imperfections in the permanent work. It is often more economical to spend more time and effort in constructing the Trials than the expensive quality control after the completion of the permanent work. If due to the cost or schedule, the construction of Trials is not accepted by client, it is advisable to carry out more test on the first panel, in order to avoid a mistake to be repeated in the whole work (EFFC/DFI Guide, 2018).

2.2.2 Quality Control during the construction

Quality control checks play an important role to avoid the occurrence of imperfections in the constructions of diaphragm walls.

To control the quality of the construction, all the work steps have to be checked. The main quality controls are listed below (Libano, 2014), (EFFC/DFI Guide, 2018):

- the verticality as well as the alignment along X and Y axes of the excavation must be controlled continuously during the excavation in order to correct the deviation early.
- Quality control of the manufacturing process of the concrete
- Testing of the characteristic of the fresh concrete
- Suitability testing to find out the properties of concrete (fresh and hardened), e.g., Workability, durability, stability, rate of strength gain, thixotropy and workability retention time
- Conformity testing to proof whether the fresh concrete fulfils the designed properties

Todays, there are many new cost-effective equipment that simplify the quality control, e.g. Shaft Area Profile Evaluator (SHAPE®) (see Figure 2.6). This device is able to present a visual 3D representation of an excavation prior to the commencement of pouring concrete (www.pile.com, n.d.).

Figure 2.6: Excavation's quality control device: Shaft Area Profile Evaluator (SHAPE®) (reprint from (www.grlengineers.com, n.d.)) (Copyright © GRL Engineers, Inc.)

Another new method to control the quality of the joints between two panels of the diaphragm walls is joint inspector method. After excavation of the adjacent panel, the joint to the neighboring panel is exposed. So, it is the best time to control the quality of the joints. At this time, the joint inspector method can be applied (Schneider, 2013).

For example, if by excavation, the grab leaves the verticality in an area, it causes excess concrete in the primary panel and therefore, adequate joint overlapping will not be established and consequently the joint will not be waterproof. If the grab excavates the secondary panel with distance to the primary panel's joint as well, the joint cannot be constructed as a watertight joint (Ewald & Schneider, 2015) (see Figure 2.7).

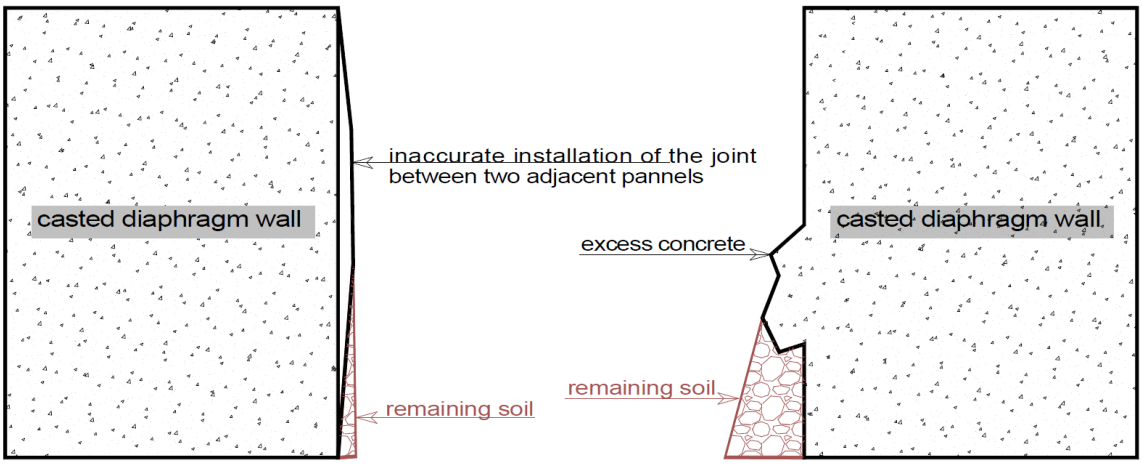

Figure 2.7: Deviation due to excess concrete (left) deviation due to miss-aligned joint element (right) for excavation of Diaphragm walls

In such circumstances, the inspector method can be utilized to measure the width of the panel in the different depth. So, the accuracy of the location of the joints can be checked. After excavating of the secondary panel, the joint inspector with mechanical sensors will be mounted to the grab. It will move along the excavation and with help the installed sensors scans the joint profile and measure the wall's width. The data will be sent via Bluetooth to a laptop in the near of the inspector. Afterwards, the results can be displayed immediately after measurement in order to be assessed (https://fugeninspektor.de/, n.d.).

In the following figures 2.8, the joint inspector method as well as the application's area is represented.

reprint from (https://fugeninspektor.de/, n.d.)

reprint from (https://fugeninspektor.de/, n.d.)

Figure 2.8: Quality control the joints with the joint inspector method

During the construction, by repeating a same form of imperfection, it should be concerned that the problem could be based on the planned details, material or process. In such cases, the plan, process and material's property have to be proofed and if required improved in order to prevent the imperfection to be repeated in the rest of the work.

Further, it is very important that the total process of construction be supervised by a qualified person with sufficient experience. Moreover, the construction's methods and proof criteria have to comply with the latest standards.

2.2.3 Testing completed Works prior to excavation

The hardened concrete in the diaphragm wall is not visible before the excavation of the construction pit. Considering the fact that despite the applying appropriate methods and equipment and adequate quality control tests by Constructor is not the occurrences of imperfections impossible. Therefore, the completed work has to be investigated for the possible imperfections before the commencement of the excavation.

If the imperfections are not so considerable, regard to the structural requirements of the construction and in accordance with the intended durability, it can be decided whether the imperfections are acceptable or not (EFFC/DFI Guide, 2018).

Making decision about the acceptance of an imperfection is not easy. Sometimes, the decision will be made according to the past experience.

In some cases, the decision has a significant effect on cost and schedule of the project. As an assistance to support the decision, the numerical simulation of diaphragm walls with the available imperfections can be used. In this Dissertation, a Fortran-code is developed, that with help of this program, some imperfections as bentonite cavity can be numerical simulated and investigated in order to assure the assessment of the defect.

For example, consider a situation that a diaphragm wall, which is designed for the vertical sealing of construction pits during the construction's time, has an imperfection near the surface of the groundwater level. This circumstance can be simulated to prove whether the wall despite of the existing imperfection possess adequate stability against the existing water and soil pressure or not.

There are various methods available to test the diaphragm wall after completion (Post-Construction Testing Methods). Such tests can be intrusive or non-intrusive. Regarding to the results of these tests, some information can be discovered about the geometry and the quality of the diaphragm wall.

For applying the non-intrusive methods, the measurement sensors have to be installed in the critical points such as joints between neighbouring panels, around the water stops or in the area with dense rebar spacing before concrete pouring (Spruit, van Tol, Broere, Doornenbal, & Hopman, Distributed temperature sensing applied during diaphragm wall construction, 2017).

An important difficulty with the results of the non-intrusive methods is the interpretation of the results correctly. It needs special knowledge as well as many experiences. However, if testing of the diaphragm wall is needed, applying the non-destructive methods are preferable (EFFC/DFI Guide, 2018).

In following, the various types of tests for the completed work are presented:

I. **Direct Testing methods:** In this method, the concrete will be cored in order to investigate the properties of the hardened concrete. By using the closed-circuit television method (CCTV) inside the drilled hole, the status of the element can be monitored (EFFC/DFI Guide, 2018).

II. **Crosshole Sonic Logging (CSL):** This method is primarily applied to investigate the structural integrity of drilled shafts and other concrete piles with large diameter (https://en-academic.com, n.d.). Later, this method is expanded to use for the diaphragm wall as well. The CSL method is able to represent the information about the quality of the concrete (Mendez, Rausche, & Paulin, 2012).

    Moreover, this method can be utilized as well to investigate the quality of joints in the diaphragm walls (Spruit, van Tol, Broere, Slob, & Niederleithinger, Detection of anomalies in diaphragm walls with crosshole sonic logging, 2014).

    Because of the difference between the density and stiffness of bentonite and concrete, the sound speed in the both materials are different. Therefore, with applying an acoustic signal, it is possible to discriminate the bentonite and concrete after completion of the construction (Spruit R. , Hopman, van Tol, & Broere, 2011).

The CSL method based on the measuring the velocity of ultrasonic waves moving between the ultrasonic probes in parallel tubes. These tubes have to be installed prior to pouring concrete in the reinforcement cage (Hajali & Abishdid, 2014). In the figure 2.9, an outline of the Crosshole Sonic Logging method is shown:

reprint from (https://olsoninstruments.com, n.d.)

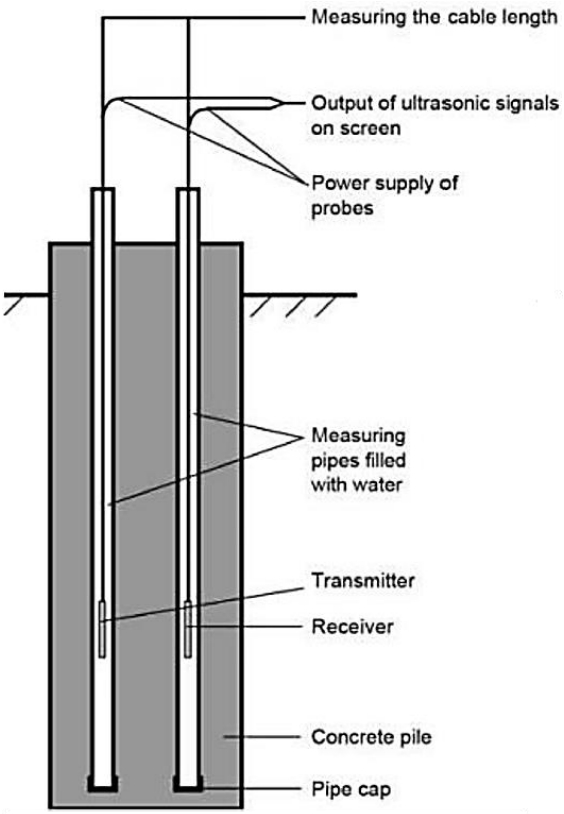

reprint from (Bagui, Puri, & Subbiah, 2020)

Figure 2.9: CSL-method

The ultrasonic probes have resonant frequencies with the range from 40 to 60 kHz range. Moreover, the applied tubes have typically an inside diameter from 35 to 50 mm. Furthermore, after the concrete pouring, the tubes will be filled with the water in order to establish an acoustic coupling of the sensor to concrete. It should be noted that the distance between tubes is not exceeded 2 m, so that a clear signal will be ensured (Mendez, Rausche, & Paulin, 2012).

The tubes are normally chosen from steel or PVC material. It is preferable to utilize the steel tubes, because the studies are shown that the PVC tubes are tended to separate due to the heat of the hydration process of concrete and it causes errors in the results of CSL test (https://en-academic.com, n.d.)

For the CSL method can the following advantages be named (White, Nagy, & Allin, 2008), (Daghighi, Sammy;, 2019):

- Evaluate the integrity, consistency and concrete quality for cast-in-place concrete structures.
- If a major defect exists, it is simple to discover it from the results of the test.
- There is no limit for the depth of the examined element.
- With high rate of accuracy, the depth of the anomaly can be specified.
- If adequate number of tubes are installed, the horizontal extent of a defect can be determined as well.
- The results of the test are without delay accessible (real time analysis).
- The Tomography of the structure is available.

Also, applying the CSL method has some disadvantage (EFFC/DFI Guide, 2018), (White, Nagy, & Allin, 2008):

- The methods need preparation prior the concrete pouring. It means, the applying of the method should be planned early enough.
- Some factors, e.g., uncured concrete, debonding, accuracy of tube position, etc. can affect the results of the test and make the interpretation complicated.
- Only the concrete between the tubes can be investigated.
- This method is not able to provide any information about the cover zone, i.e., between the face of excavation and the reinforcement.
- Interpretation of the results need special knowledge and experience.

As already mentioned, the interpretation of the CSL test's results require a special knowledge and experience. Generally, if the ultrasonic waves propagate, it is the sign of a concrete with good quality. Longer wave trave time with less amplitude shows that the quality of the concrete is not good or concrete is partial porous. If the wave is lost completely, it means that a void space in the concrete structure exists (www.pcte.com.au, n.d.)

In the following Figure 2.10, the results of the Crosshole Sonic Logging method are displayed:

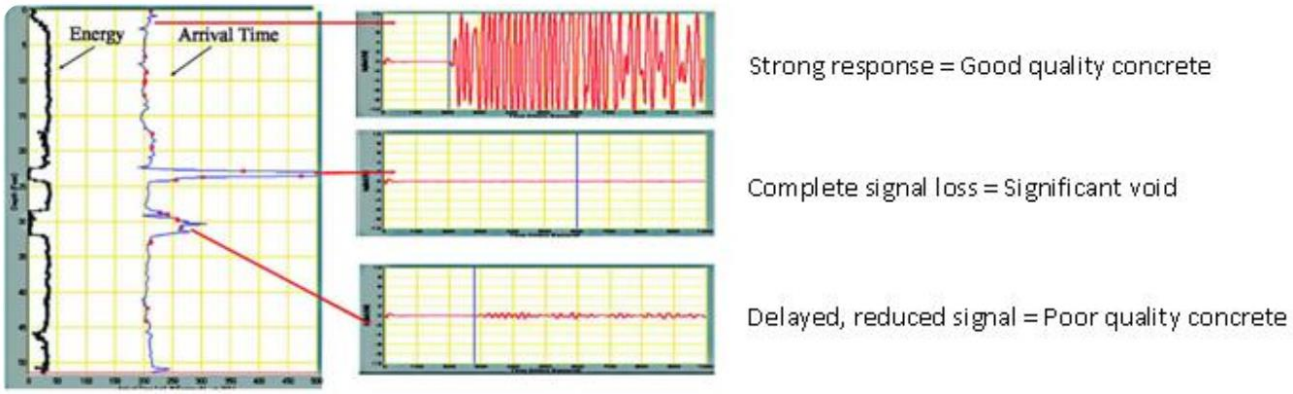

Figure 2.10: Interpretation of the CSL-method's results (reprint from (https://olsoninstruments.com, n.d.))

III. Thermal Integrity Profiling (TIP): This method is based on the measurement of the temperature profile of the cast-in-place concrete. Because of the different heat generation and thermal conductivity between the inclusions in the concrete and bentonite, the temperature is varied. Also, during the curing process (normally one or two days after concrete pouring) the produced hydration's heat will be measured and according to the results, the integrity and homogeneity of the concrete can be evaluated (ASTM D7949-14, 2016). The monitoring of the temperatures can be normally carried out in the following procedures (EFFC/DFI Guide, 2018):

- Distributed fiber optic sensing (DFOS)
- Thermistor Strings and Thermistor probes

Distributed fiber optic sensing (DFOS): During the several construction's phases of the Diaphragm walls, the concrete and bentonite replaced each other. By replacing the excavation bentonite with fresh bentonite in de-sanding process, the temperature difference between old and fresh bentonite can be identified in the trench. By commencement of the concrete pouring, the concrete will be replaced the bentonite. They have various temperatures as well. Normally, bentonite have less temperature than concrete in the trench. By continuous monitoring of the temperature near the joints, it can be realized whether the concrete between two parts of diaphragm walls at the joint exist or not. As well, it is possible to identify the concrete with low quality by temperature measurement after concrete casting. Because of the hydration heat, the temperature of the early-age concrete will be increased and if locally temperature's variations being found, it shows local defects such as voids, bulging or soil intrusion in the wall (Spruit, van Tol, Broere, Doornenbal, & Hopman, Distributed temperature sensing applied during diaphragm wall construction, 2017), (Qianchen Sun & Z.E.B. Elshafie, 2019).

For the Installation of fiber optics in diaphragm walls, various technique can be utilized. They can be embedded direct on the reinforcement cage or placed in the hollow tubes (Goeminne, Brutin, Benoot, Couck, & Vos, 2017).

In the following figures 2.11 and 2.12, the Installation of the fiber optic cables to the reinforcement cage is shown.

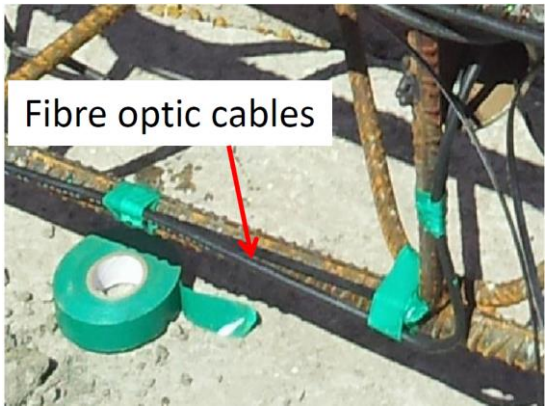

Figure 2.11: Installing of the Fiber optic cables direct on the reinforcement cage (reprint from (Li, Soga, & Kechavarzi, 2018))

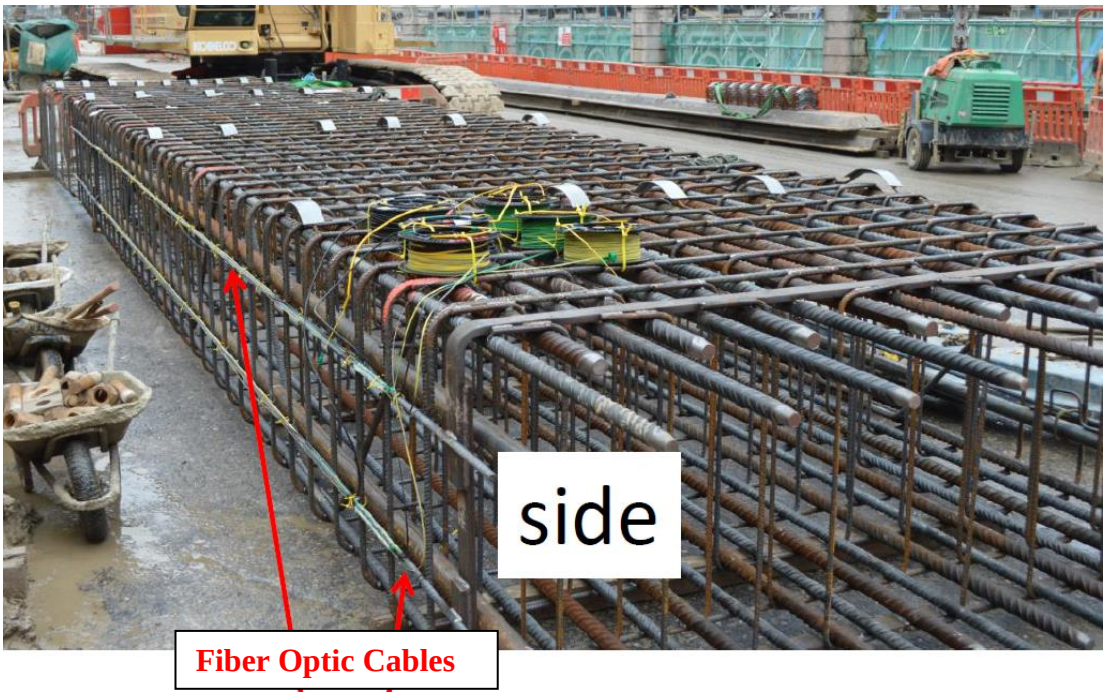

Figure 2.12: Location of the Fiber optic cables at the side of diaphragm wall (reprint from (Li, Soga, & Kechavarzi, 2018))

Another application of the DFOS method is the continuous strain measurement of the underground structures, e.g., Diaphragm walls. In the following figure, the monitoring of the behavior of the diaphragm wall during the excavation with DFOS method is displayed. The measurement of the strain helps the Constructor to prevent the collapse of the diaphragm wall early. If the strain during the excavation process unusually increases, it means that a serious defect is existing and the wall is going to deform and maybe afterwards to collapse. Therefore, the excavation has to be stopped in order to carry out more tests for assessing the quality of the diaphragm wall. In the following sketch, figure 2.13, the location of the fiber optic cables, installed in the diaphragm wall of a train station is shown. Furthermore, laying cables to measure the temperature and strain at ground level are presented in the figure 2.14.

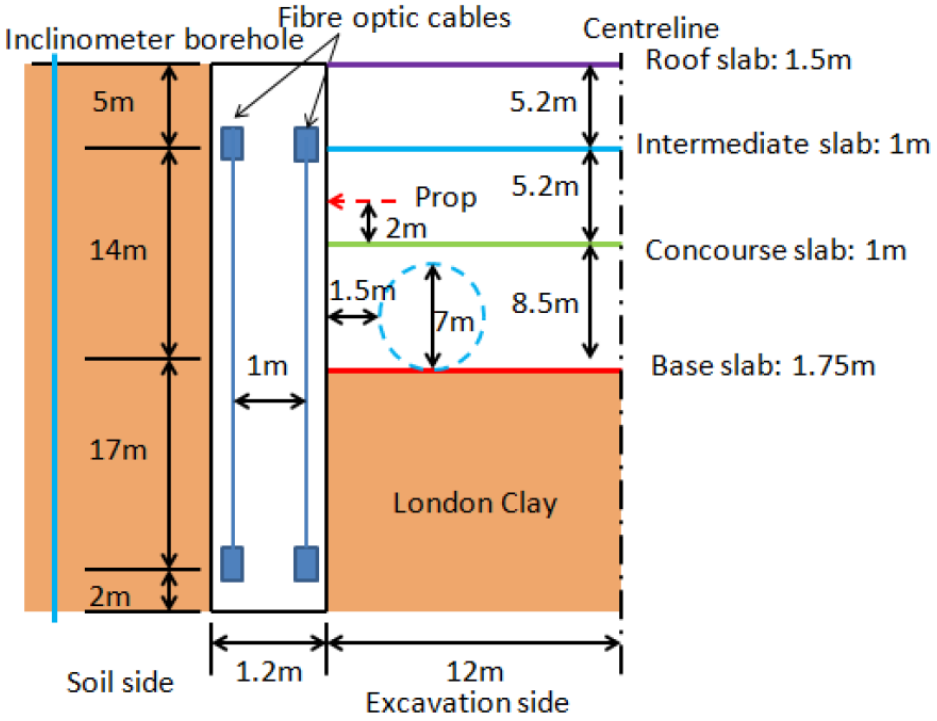

Figure 2.13: Fiber optic cables in Diaphragm wall main box (reprint from (Li, Soga, & Kechavarzi, 2018))

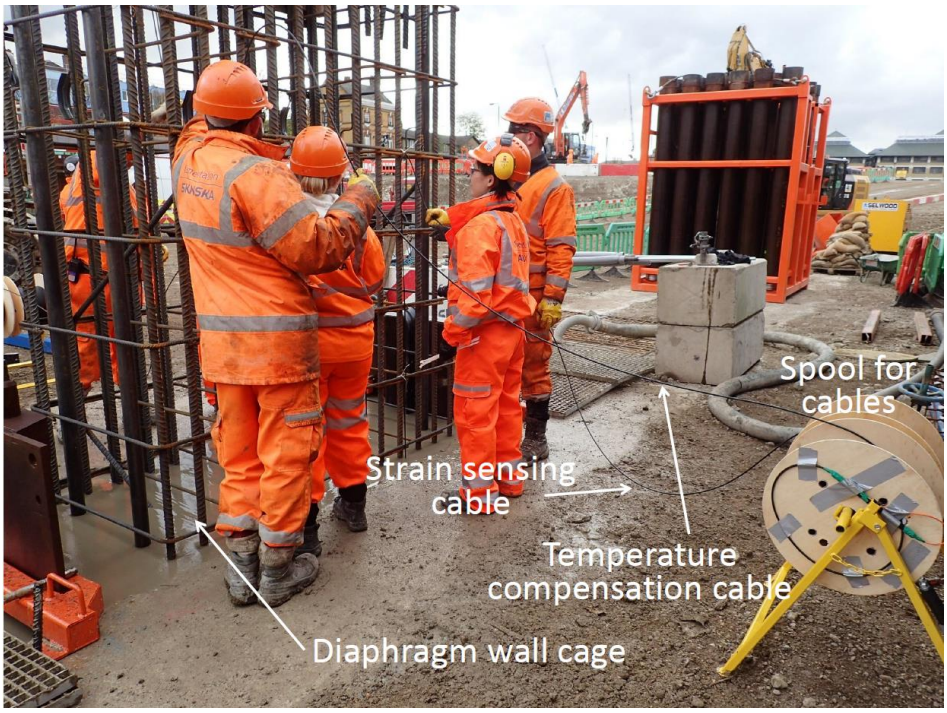

Figure 2.14: Laying cables to measure the temperature and strain at ground level (reprint from (Li, Soga, & Kechavarzi, 2018))

Thermistor Strings and Thermistor Probes: Thermistors have a large negative temperature coefficient of resistivity. They are semiconductors, which commonly show a large negative change of resistance with temperature (Encyclopedia of Ocean Sciences (Second Edition), 2001).

Due to the reliable, accurate and long-term measuring of the temperature, thermistors are be applied widely in geotechnic monitoring. Thermistors are available in the form of strings or probes (www.geosense.co.uk, n.d.).

Thermistor Probes are mounted inside a housing, which is attached at the end of a cable, ready to install in the construction. The housing is made from stainless steel or PVC. Probes are specially well suitable for the measuring of the hydration heat during the curing of the concrete (www.gkmconsultants.com, 2017). In the figure 2.15, some thermistor probes are shown.

Figure 2.15: Thermistor Probes (reprint from (www.geokon.com, n.d.))

Thermistor String is utilized for the multiple temperature measurement (temperature profile) in a single borehole. It consists of a multiconductor cable (multi-core cable) with many individual sensors. The number of sensors as well as the distance between sensors is defined in accordance with the requirement of the customer (www.gkmconsultants.com, 2017), (www.geosense.co.uk, n.d.). In the figure 2.16, Thermistor Strings are shown.

Figure 2.16: Thermistor Strings (reprint from (www.geokon.com, n.d.))

Due to the smallness of the thermistors, they are very sensible to the change of the temperature. To have a more accurate result, the resistance of the cable can be as well taken into account (hmagrp.com, 2021).

Readout of the thermistors can be done directly in degrees Celsius on the engineering unit. As alternative, a digital ohmmeter in accordance with look-up tables can be applied. For remote application, the data-collection and readout can be done automatic using wireless methods as automatic data acquisition unit (www.gkmconsultants.com, 2017), (www.geosense.co.uk, n.d.).

IV. Self-Potential Method: In geophysical problems, the self-potential method based on the natural occurrence of electrical fields at the Earth's surface or in boreholes is used often to localizing and quantifying groundwater flows (Jouniaux, Maineult, Naudet, Pessel, & Sailhac, 2009). Based on the electrical resistivity and self-potential methods, a coupled analysis used for detecting diaphragm wall seepage. This method is verified by field experiment in construction a subway station (Yang, Liu, Ding, Yang, & Xie, 2020).

2.2.4 Imperfections and defects

Many damages on deep foundations' pit are occurred every year due to the mistakes in designing and constructions of the deep foundation. The high dense of the reinforcement with small spacing, thin concrete cover, inappropriate concrete properties, lack of the knowledge of a tremie pour method, etc. are the prevalent reasons for causing imperfections and defects (Beckhaus, et al., 2011). The imperfections in the diaphragm walls are defined as the deviation from the designed quality and common continuity of the cast-in-situ concrete. The imperfections have to be more investigated, in order to decide whether the existing imperfections are necessarily defects and have to be fixed or can be regarded as a harmless anomaly. If stability and durability of the structure isn't disturbed by the imperfection, no repairing procedure is required, e.g., the grooves in the figure 2.17, which have no effect on the minimum cover of the concrete, can be ignored and consequently the quality of the structure can be accepted. It should be noted that the formation of the imperfections can have various reasons that makes the interpretation complicated. Therefore, the interpretation of the imperfections should be done by an experienced specialist (EFFC/DFI Guide, 2018).

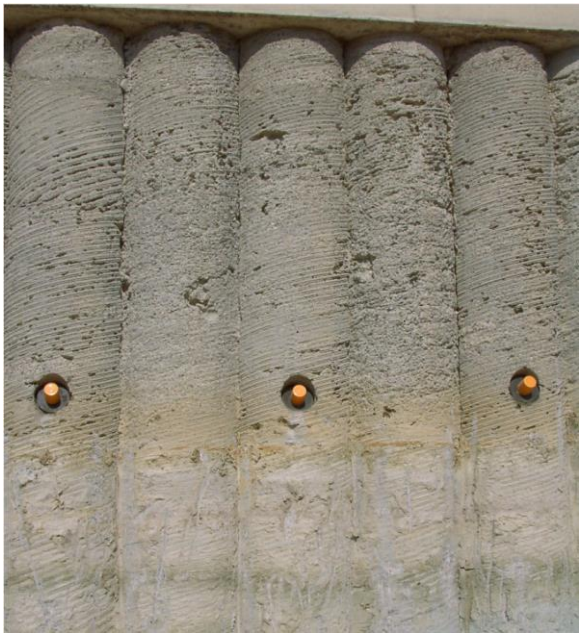

Figure 2.17: Acceptable Imperfections (reprint from (EFFC/DFI Guide, 2018))

The obstructions to flow the tremie concrete such as reinforcement cage, spacer blocks and box-outs are named as usual reasons for the creation of the imperfections. According to a joint review of problems in diaphragm walls by European Federation of Foundation Contractors (EFFC) and the Deep Foundations Institute in the United States (DFI), the insufficient workability, inadequate stability or robustness of the concrete are the main reason for imperfection in many cases. In such cases, the lack of an appropriate testing method is recognizable. Furthermore, the structural design of the reinforcement cage has a considerable consequence on the final quality of the diaphragm wall (EFFC/DFI Guide, 2018). Moreover, the damage of the joints between diaphragm wall panels is one of the most common causes of leaks in the diaphragm walls (Ewald & Schneider, 2015).

In the figures 2.18 and 2.19, some typical imperfections in the deep foundation are shown:

Figure 2.18: Typical Imperfections in deep foundation (reprint from (EFFC/DFI Guide, 2018)).

Figure 2.19: Imperfections due to the low flowability of concrete (reprint from (Mironov, Osokin, Loseva, & Kuzhelev, 2020)).

The Defects and Imperfections in the deep foundation are generally classified as follows (EFFC/DFI Guide, August 2018):

- **Anomalous material, Inclusions, Bentonite cavities:** The anomalous material are sometimes entrapped within the diaphragm walls and in the joints between diaphragm wall panels. These materials can be originated from excavated material, mixture of bentonite and concrete or from interface layer. In the following picture (figure 2.20) an occurrence of an inclusion is schematic presented, which the fresh concrete is not able to displace the existing mixture of supporting fluid and concrete (EFFC/DFI Guide, 2018), (Spruit, Hopman, & van Tol, 2012).

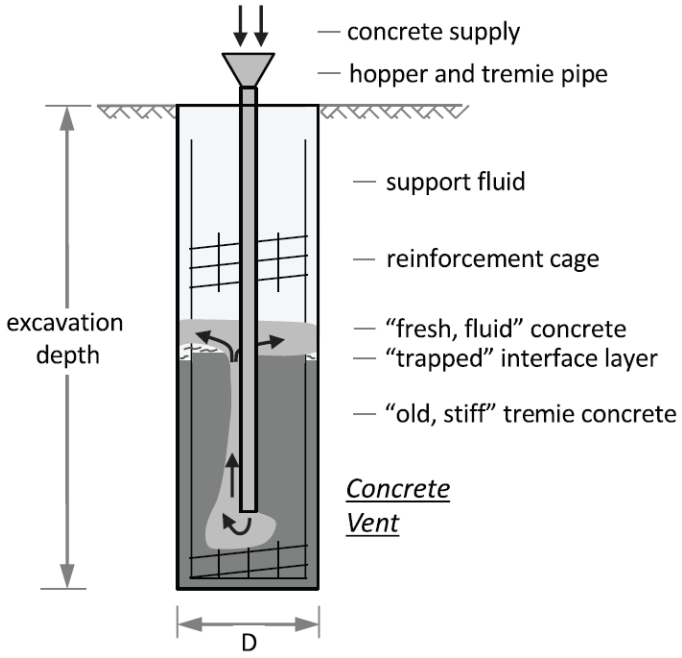

Figure 2.20: Occurrence of inclusions in a diaphragm wall (reprint from (EFFC/DFI Guide, 2018)).

Irregularity in concrete supply can causes large bentonite cavities. During the delay in concrete pouring, the concrete will be hardened and therefore is not be able to flow upwards when the fresh concrete comes and that crested often large cavities (Lubach, 2010). In the figures below 2.21 and 2.22, such imperfections are shown:

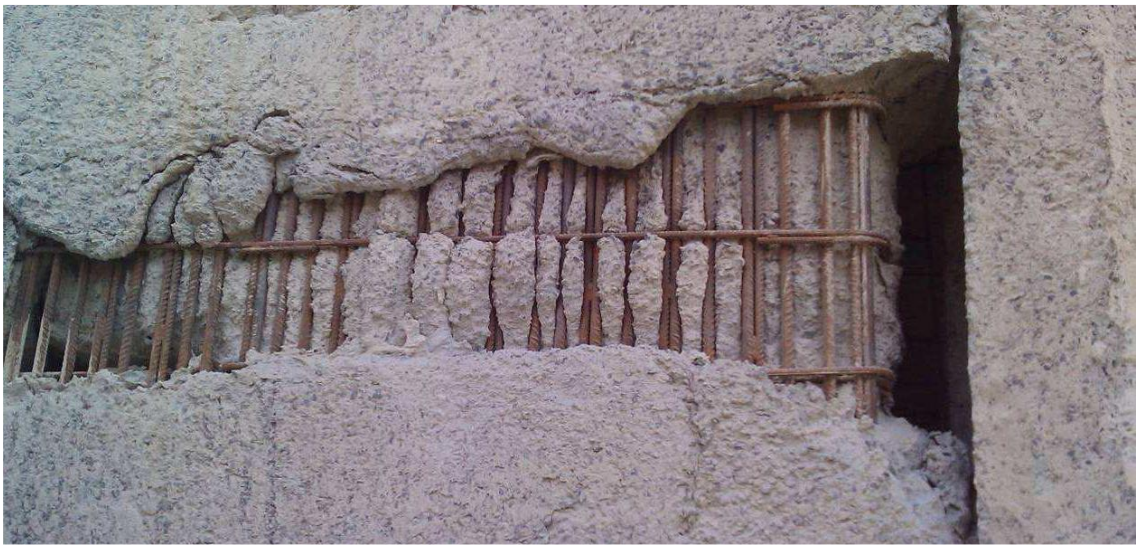

Figure 2.21: Bentonite Cavity in diaphragm wall (reprint from (Lubach, 2010)).

Figure 2.22: Inclusion defects in diaphragm wall (reprint from (Hill & Thorp, 2021)).

At the completion of the concrete placement with tremie procedure, the fresh concrete at the top of the excavations is often contaminated with bentonite, soil, ground water or excessive bleeding water. This part of the fresh concrete can be removed easily and be replaced by the clean fresh concrete (Brown, Turner, Castelli, & Loehr, 2018) (see following figures 2.23 and 2.24).

Figure 2.23: Replacing contaminated concrete at the top of a deep foundation using tremie method (reprint from (Brown, Turner, Castelli, & Loehr, 2018))

Figure 2.24: Contaminated concrete atop of a diaphragm wall (reprint from (Hill & Thorp, 2021)).

- **Channeled Bleeding:** The hydrostatic pressure of the fresh concrete can cause the creating of the vertical channels along the wall. These channels, which are visible in the interface between diaphragm wall and the ground, promotes chimneys of water upwelling on the wall. The movement of the water in fresh concrete may also cause the transport of the fine particles of the fresh concrete and therefore, the segregation of the

granular skeleton can be occurred (El Zein, Vanhove, Djelal, Madec, & Gotteland, 2021).

This phenomenon occurred usually because of an insufficient stability of the concrete, especially the poor bleeding-resistance of the concrete (EFFC/DFI Guide, 2018).

The fresh tremie concrete has to be consolidated under its own self-weight and without any possibility to vibrate the fresh concrete. Furthermore, the concrete must be able to flow easily between reinforcement cage and completely full the entire volume of the excavation. For this reason, the concrete used for tremie procedure must provide a high workability. On the contrary, the high rate of water in the concrete mix increases the risk of the arising bleed channels. Therefore, the design of the concrete mix plays an important role in tremie concrete method. By concrete mix, it should also be noted, that the aggregate particles as well as the water within the concrete mix have to be distributed uniformly, in order to reduce the tendency of the concrete to segregate and bleed. Experiences also show that adding Fly ash and silica fume in the concrete mix can reduce the bleeding in the concrete. Adding air-entraining admixtures are also decrease the tendency of the concrete to bleed, they also increase the workability of the concrete. But they cause more porosity in the concrete and thus reduce the strength of the foundation. Moreover, the entrained air in the bottom of a deep foundation may be lost due to the great pressure at the bottom of the trench. In such situation, the loss of the entrained air causes less workability at the depth and therefore, it arises the possibility of occurring imperfections at the bottom of the foundation. Another solution to decrease the water/cementitious material ratio is using water-reducing admixtures. These admixtures increase the workability of the concrete without adding excessive water, which is needed only for lubrication of the cement during the pouring of the fresh concrete and is not required for the hydration of the cement. The disadvantage of applying water-reducing admixture is by delay in pouring concrete and using inappropriate admixture, which can lead to rapid setting of the fresh concrete by unexpected delay in concrete delivery. There is another admixture which is utilized often in tremie method to prevent bleeding. The viscosity-modifying admixtures (VMAs) are binding the free water of the concrete and therefore increase the viscosity

and cohesiveness of the concrete, in order to decrease the possibility of segregation and reduce the bleeding water. Applying VMAs can cause thixotropic behavior in concrete, wherein the concrete will be more fluid, when it is displaced or pumped and will stiffen up in stationary conditions. This behavior can cause problems as well, when the concrete pour is unplanned interrupted (Brown, Turner, Castelli, & Loehr, 2018). In the following photos (figure 2.25), such channeled Bleeding are shown.

reprint from (El Zein, Vanhove, Djelal, Madec, & Gotteland, 2021)

reprint from (EFFC/DFI Guide, 2018)

Figure 2.25: Upwelling chimneys and running up bleeding channels of the diaphragm walls

To assess the imperfections due to the channeled Bleeding, if the bleed channels are arisen in the limited area and thickness, the durability of the wall may not be considerably affected. In such circumstances, the bleed channels are usually not considered as defect and they are not needed to be repaired (EFFC/DFI Guide, 2018).

- **Mattressing, Shadowing, quilting:** This phenomenon can be occurred in light or significant form. In the light Mattressing, there are only vertical features, which are emanating from the vertical reinforcement and they could be a route for the bleeding

water. The significant form of Mattressing is defined with the intersecting vertical and horizontal linear features, which are as well emanating from the reinforcement. The thin concrete cover, high congestion of the reinforcement cage as well as the low flowability of the fresh concrete have a great effect on the extent of the Mattressing. The Mattressing is found frequently in the higher elevation of the wall, where the hydrostatic pressure decreases. Mattressing can interrupt the entire depth of the concrete cover, thereby the durability and strength of the element can be badly affected. By higher frequency and extent of the Mattressing, it should get noticed as a defect and require additional treatment (EFFC/DFI Guide, 2018). In the next figure 2.26, some mattressing in Diaphragm walls are shown.

reprint from (Hill & Thorp, 2021)

reprint from (EFFC/DFI Guide, 2018)

Figure 2.26: Mattressing in Diaphragm walls

2.2.5 Applying SPH-method to assessment of imperfections and defects in diaphragm walls

As mentioned before, many damages are occurred by reason of defects in diaphragm walls during the execution of deep foundations. Such defects can cause the collapse of the excavation pit and threat the adjacent constructions.

By construction of diaphragm walls, negligible imperfections are normally happened. As an important duty in the construction's site is to decide, for which imperfection is a repairing work needed. Since the simulation of very complicated problems can be carried out easily with the help of powerful computers nowadays, applying of numerical methods to support such assessment is practical and very useful.

There are many numerical methods, that can be applied in geotechnical problems. In order to choose a proper numerical method, the property of the soil plays an important role. It can be chosen either the traditional common grid-based methods, which a suitable Mesh generation at the beginning of the calculation is necessary, or almost new numerical meshless methods, which due to the lack of the grid is the simulating of models with complicated geometry and large deformations without much effort possible.

If the excavation is performed in the clay with high cohesivity, the expected deformation of the soil is low. In such cases, the soil stays almost stable and mostly porewater flows in the excavation pit. Here, applying the famous grid-based Finite Element Method (FEM) or similar grid-based methods is a good choice.

However, there are also situations that the excavation has to be done in the granular soil as sand. In such circumstances, the behavior of the soil is totally different. The soil flows together with porewater in the excavation pit as like as fluid and therefore the deformation of the soil is very large. For such problems, the utilization of the meshless methods as like as Smoothed Particle Hydrodynamics (SPH) is a correct choice, because applying of the grid-based methods for such problems with large deformations is very difficult.

Although, some technics for remeshing of the grid-based methods has been developed to manage this problem, but the implementation of such algorithms is complicated.

For this reason, in the present research, the popular meshfree method “Smoothed Particle Hydrodynamics” (SPH) is studied and the capability of this method to simulate the defects in the diaphragm walls and collapse of the granular soil with large deformation investigated.

In the next chapters, the concept of the Smoothed Particle Hydrodynamics method (SPH) as well as the algorithm and formulation of this method explained. Thereafter, the developed Fortran-Code in this research is validated by means of comparing the results of the simulations with some benchmark experiments. Afterwards, the ability of the SPH-method to model various geotechnical problems is verified. Finally, in order to apply the method for a practical problem, the collapse of the historical archive building of the city Cologne in 2009 studied and the behavior of the defect and collapse of the diaphragm wall in saturated sand with high groundwater level is simulated and the results are compared with the carried-out experiments in the Institute of Geo Engineering in the Clausthal University of Technology.

3 Concept of Smoothed Particle Hydrodynamics (SPH) method

3.1 SPH Background

The Smoothed Particle Hydrodynamics methods was invented at the first time in 1977 by Lucy (Lucy, 1977), Gingold and Monaghan (Gingold & Monaghan, Smoothed particle hydrodynamics: theory and application to non-spherical stars, 1977) for numerical simulation of the astronomical problems. In the last decades, the SPH-method was applied in a variety of different problems such as geotechnical problems (Bui H. , Fukagawa, Sako, & Ohno, 2008), (Gholami Korzani M. , Galindo-Torres, Scheuermann, & Williams, 2018), (Bui, Sako, & Fukagawa, 2007), (Gholami Korzani M. , Galindo-Torres, Scheuermann, & Williams, 2018), (Bui, Kodikara, Bouazza, Haque, & Ranjith, A novel computational approach for large deformation and post-failure analyses of segmental retaining wall systems, 2014), (Bui & Fukagawa, An improved SPH method for saturated soils and its application to investigate the mechanisms of embankment failure: Case of hydrostatic pore-water pressure, 2013), (Grabe & Stefanova, Numerical modeling of saturated soils, based on Smoothed Particle Hydrodynamics (SPH), Part 1: Seepage analysis, geotechnik 37 (2014), Heft 3), (Grabe & Stefanova, Numerical modeling of saturated soils based on smoothed particle hydrodynamics (SPH), Part 2: Coupled analysis, geotechnik 38 (2015), Heft 3), fluid dynamical and coastal Engineering problems (Wen, Ren, & Wang, 2018), (Ye & Zhao, 2017), (Chang, Kao, Chang, & Hsu, 2011), (Roselli, Vernengo, Brizzolara, & Guercio, 2019), (G.Panicker, Goel, & R.Iyer,

2015), (Mirmohammadi & Ketabdari, 2011), multi-phase flow (Monaghan & Kocharyan, SPH simulation of multi-phase flow, 1995), (Peng, Xu, Wu, Yu, & Wang, 2017), (Fourtakas & Rogers, 2016), (Gong, Shao, Liu, Wang, & Tan, 2016), Shock Simulation (Monaghan & Gingold, Shock Simulation by the Particle Method SPH, 1983), Heat transfer (W. Cleary & J. Monaghan, 1999), etc.

To solve the different problems with numerical methods, the geometry of the problem needs to be discretized into finite number of discrete components. In the numerical method with grid, the continuum domain of the problem will be discretized through a set of mesh. But in the meshless numerical methods (e.g., SPH-method), the computational domain will be divided into a set of particles. The accuracy of the numerical method is dependent directly to the grid size or initial particle spacing. Thereafter, the integral form of the governing equations, which are obtained from the mathematical models considering the initial and boundary conditions, can be changed in an approximation over the domain. SPH method is able to simulate a vast range of problems from very small scale to very large scale (Liu & Liu, 2003).

The SPH-method has certain advantage compared to grid-based methods, particularly in modeling problems with free surface, deformable boundaries, multiphase model, etc., on the other hand, SPH-method is often computationally more expensive than grid-based methods (P. Morris, J. Fox, & Zhu, 1997). Moreover, it can be noticed, that SPH method can be modelled easier for the problems with three dimensions (Stellingwerf & Wingate, 1993)

By modelling of the problems with large deformation with grid-based methods such as finite element method (FEM), appears often because of the excess distortion of grids an instability in the calculation (Nonoyama, Moriguchi, Sawada, & Yashima, 2015), but such problems can be solved without any difficulty with the meshfree methods particularly smoothed particle hydrodynamics method.

3.2 Basic ideas of SPH

Smoothed Particle Hydrodynamics is a Lagrangian particle-based method. It means that, SPH includes the movement of particles according to time (Monaghan J. , Smoothed Particle Hydrodynamics Code Basics, 2001). In this method, the particles freely without any grid or mesh carry the properties of the field function as mass, density, viscosity, velocity, etc. (Morris & Monaghan, 1997). In this method, the continuum domain will be discretized in a set of particles, which they move according to governing equations without need to any predefined connectivity (Liu & Liu, 2003).

SPH method is an interpolation method and its formulation included two basic steps. The first step is an integral representation of an arbitrary function and the second step is particle approximation (Liu & Liu, 2003), (Monaghan J. , Smoothed Particle Hydrodynamics, 1992).

In the Figure 3.1 the necessary steps to simulate and solve a problem with SPH-method is shown.

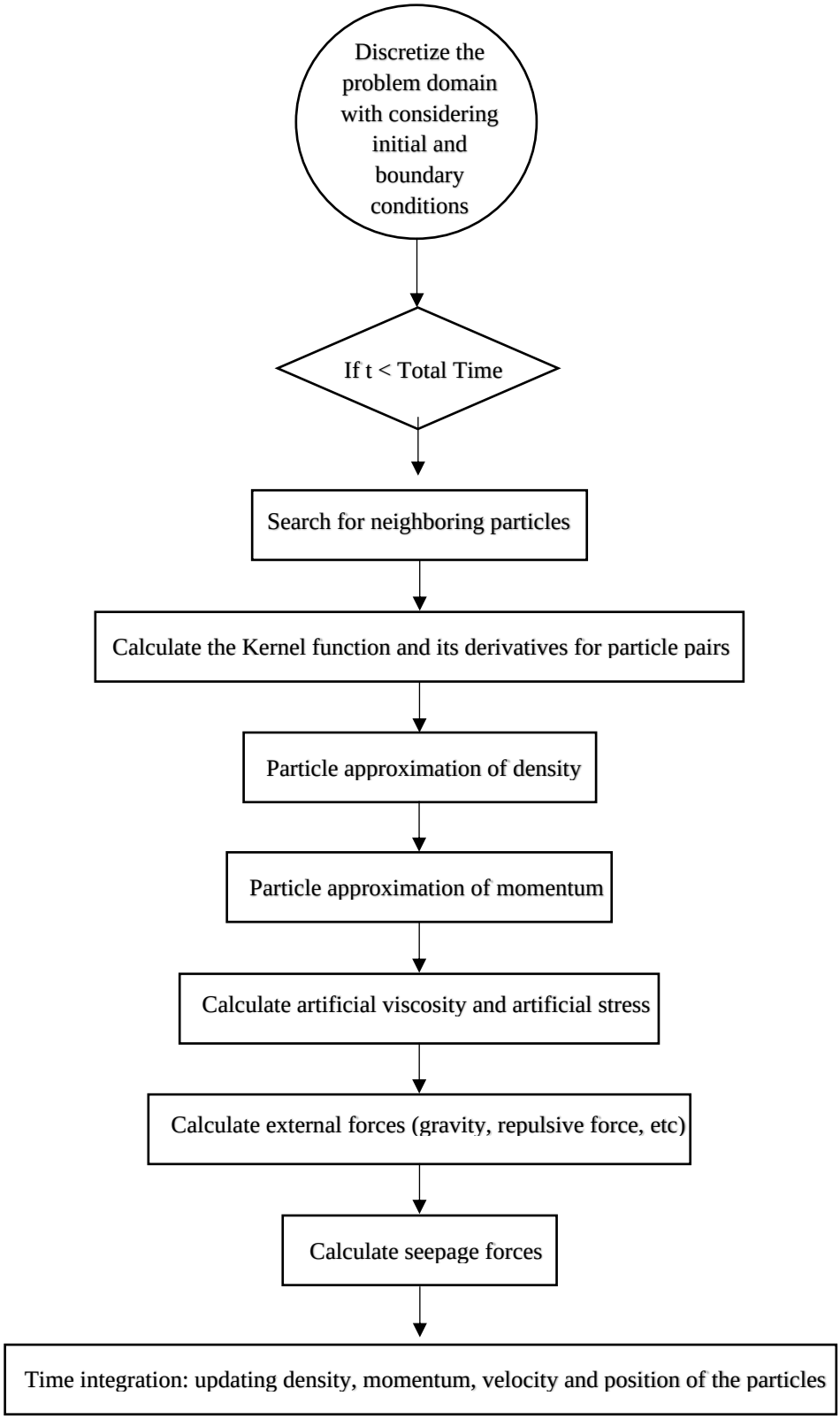

Figure 3.1: Algorithm to solve a problem with SPH-method

Based on the algorithm in figure 3.1, a Fortran-Code is developed in this study. In this code, the geometry of each problem and its domain will be discretized into finite number of particles at the beginning. After that, the initial and boundary conditions will be defined and according to the chosen boundary method, the required number of boundary particles will be created. In the next step, the neighboring particles at each time step will be found and accordingly the kernel function and its derivatives for each pair of particles will be calculated. Afterwards, the equation of density and momentum for water and soil will be solved at each time step. When needed, the methods as artificial viscosity, return mapping algorithm, etc. will be applied to prevent the instability of the model. Furthermore, the external forces and seepage forces should be added to the governing equations. Finally, the properties of the soil and water particles as well as the velocity and position of all particles will be evaluated at each time steps. This process will be continued until the final time is reached.

In the Figure 3.2 a view of the developed Fortran-Code is shown:

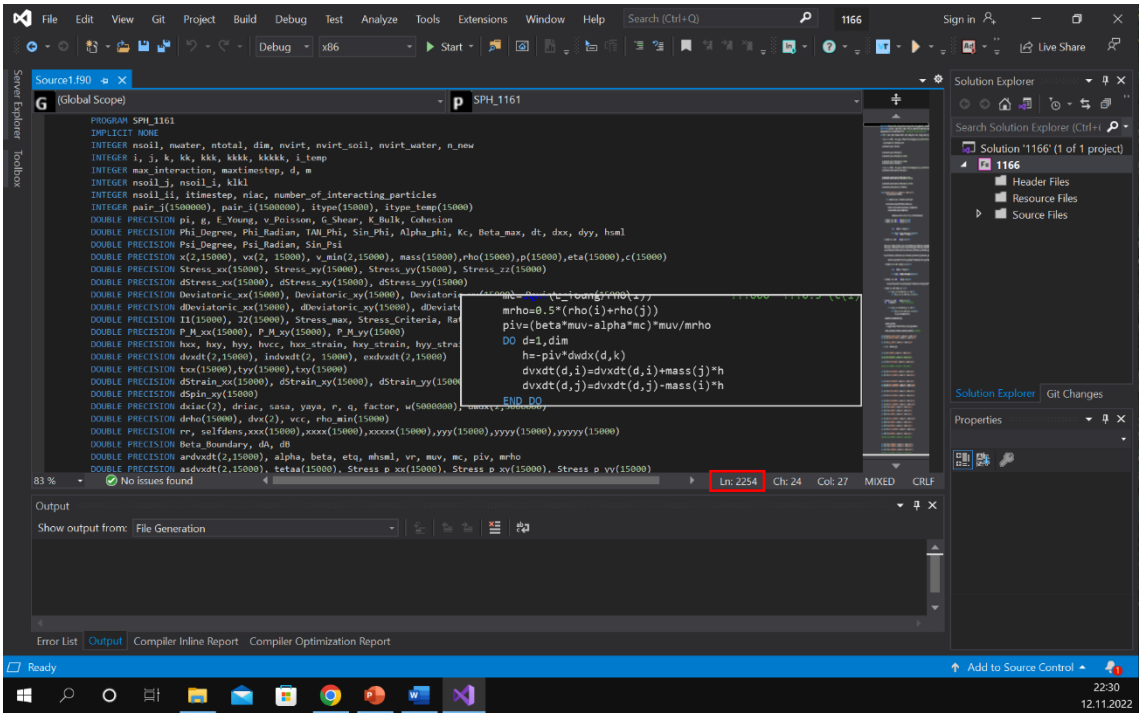

Figure 3.2: View of the developed Fortran Code in Visual Studio with Intel Fortran

3.3 Integral representation

The integral representation method, also called Integral function representation or kernel approximation, is utilized to approximate the field function.

The integral representation of any function f(x) over the entire space is defined as follows (Liu & Liu, 2003), (Monaghan J. , Smoothed Particle Hydrodynamics, 1992):

$$< f(x) >= \int_{\Omega} f(x')W(x - x', h)dx' \tag{3.1}$$

where W is smoothing kernel function.

Furthermore, the integral representation of the derivative of any function can be derived by substituting $f(x)$ with $\nabla . f(x)$ in the previous equation (Liu & Liu, 2003):

$$< \nabla . f(x) >= -\int_{\Omega} f(x') . \nabla W(x - x', h)dx' \tag{3.2}$$

3.4 Kernel Functions

The kernel function should have at least one derivative. If this derivative is continuous, it will prevent large fluctuations in calculating the forces at each particle. The smoothing kernel in the SPH method should satisfy following conditions (Liu & Liu, 2003), (Monaghan J. J., 1988), (Gingold & Monaghan, Kernel Estimates as a Basis for General Particle Methods in Hydrodynamics, 1982):

1. Normalization condition (unity condition):

$$\int W(x - x', h)dx' = 1 \tag{3.3}$$

2. Delta function property:

$$\lim_{h \to 0} W(x - x', h) = \delta(x - x') \tag{3.4}$$

where $\delta(x - x')$ is the Dirac delta function:

$$\delta(x - x') = \begin{cases} 1 & x = x' \\ 0 & x \neq x' \end{cases} \tag{3.5}$$

3. Compact support:

$$W(x - x', h) = 0 \quad when\ |x - x'| > kh \tag{3.6}$$

4. Positivity:

$$W(x - x') \geq 0 \quad for\ any\ point\ at\ x' \tag{3.7}$$

5. Decay: The kernel function for neighboring particle with bigger distance is smaller compare to neighboring particle with shorter distance.

6. Symmetric property: The smoothing function should be selected as an even function.

7. Smoothness: The kernel function should have enough smooth.

In diverse Literature, different kernel functions were used. For example, although Lucky in his original work (1977) used a bell-shaped function, Gingold and Monaghan (1977) utilized the Gaussian kernel (Liu & Liu, 2003), (Lucy, 1977), (Gingold & Monaghan, Smoothed particle hydrodynamics: theory and application to non-spherical stars, 1977). In the present work, a kernel function based on spline functions is used, which suggested in 1992 by Monaghan (Monaghan J. , Smoothed Particle Hydrodynamics, 1992):

$$W(r,h) = \frac{\omega}{h^{\nu}} \begin{cases} 1 - \frac{3}{2}q^2 + \frac{3}{4}q^3 & if\ 0 \le \frac{r}{h} \le 1; \\ \frac{1}{4}(2-q)^3 & if\ 1 \le \frac{r}{h} \le 2; \\ 0 & otherwise \end{cases} \tag{3.8}$$

where $q = \frac{r}{h}$, ν is the number of dimensions and ω is a constant factor with $\frac{2}{3}$ in 1D, $\frac{10}{7\pi}$ in 2D and $\frac{1}{\pi}$ in 3D.

3.5 Particle approximation

For implementation the particle approximation, defining the support domain is required. The support domain is a part of the main domain, which is defined for each particle individually. The support domain of the kernel function is defined as follows:

support domain of the kernel function $W = k \cdot h$

where k is a constant number related to the kernel function to define the effective area of the smoothing function and h is the smoothing length, which is defined the influence area of the kernel function for each particle.

The support domain of the kernel function W is shown in the following graphics (see figures 3.3 and 3.4):

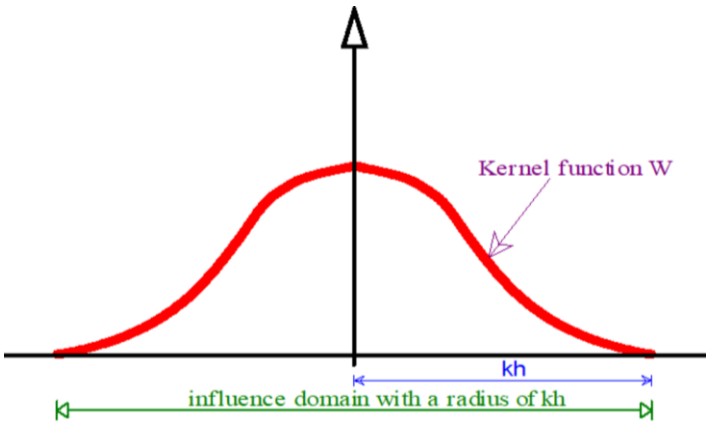

Figure 3.3: Schematic 2D-presentation of the kernel function W

SPH based on interpolation over all neighboring particles through kernel function within its support domain. To approximate a function at each particle, values of the function in all the neighboring particles should sum up in the influence domain of the particle. This process is called Particle approximation.

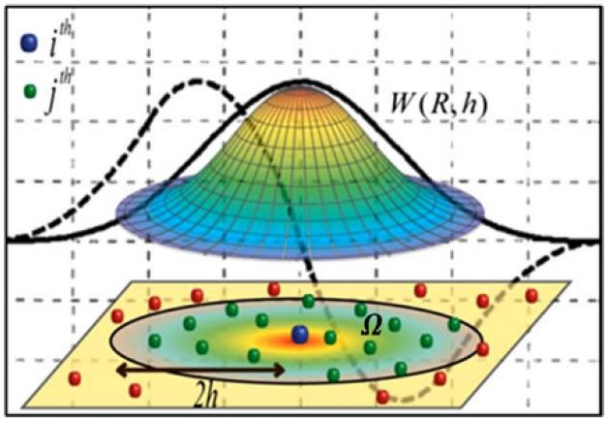

Figure 3.4: Schematic 3D-presentation of the Particle approximation with kernel function W and support domain Ω (reprint from (M. Abdelrazek, Kimura, & Shimizu, 2016)).

The particle approximation of a function for particle i is defined as below (Liu & Liu, 2003):

$$< f(x_i) > = \sum_{j=1}^{N} \frac{m_j}{\rho_j} f(x_j).W_{ij} \tag{3.9}$$

where N is the total number of neighboring particles in the support domain of particle i, and

$$W_{ij} = W(x_i - x_j, h) = W(|x_i - x_j|, h) \tag{3.10}$$

Similarly, the particle approximation for the derivative of any function can be calculated as following (Liu & Liu, 2003):

$$< \nabla . f(x_i) >= \sum_{j=1}^{N} \frac{m_j}{\rho_j} f(x_j) . \nabla_i \mathrm{W}_{ij} \tag{3.11}$$

where

$$\nabla_i W_{ij} = \frac{x_i - x_j}{r_{ij}} \frac{\partial W_{ij}}{\partial r_{ij}} = \frac{x_{ij}}{r_{ij}} \frac{\partial W_{ij}}{\partial r_{ij}} \tag{3.12}$$

where r_{ij} is the distance between particle i and its neighboring particle j.

It should be pointed out, that the particle approximation is performed at every time step.

3.6 Neighbor particle searching

Because of the free nature of the particles in the SPH method, it exists no constant structure to identify the neighboring list of each particle. Therefore, as mentioned above, in the SPH method, the neighboring particles of each domain particle must be determined at each time step, so that the particle approximation and governing equations as continuity and momentum equations can be calculated at each time step in order to updated the velocity and finally to calculate the new location of each particle at each time step (Winkler, Rezavand, & Rauch, 2018).

Neighbor particle searching is a key point in the implementation of a SPH-Code, because the efficiency of the simulation is dependent on the chosen approach to creating the neighbour list (Domínguez, Crespo, Gómez-Gesteira, & Marongiu, 2010). Different

approaches are presented in the Literature. Here, the four famous methods will be introduced (Viccione, Bovolin, & Pugliese Carratelli, 2008):

I. **Direct Searching method:** In this method, at each time step, the position of each particle will be compared with another particle in the whole domain as well as boundary particles. When the distance between two particles is less than support domain of the kernel function, the both particles will be saved in a neighboring list and will be utilized in Pairwise Interactions in the SPH-method:

$$r_{AB} \leq kh \tag{3.13}$$

where r_{AB} is the distance between particle A and B, k is a constant number and h is the smoothing length.

It should be pointed out that the boundary particles do not need to be compared with another boundary particles.

This method has a simple algorithm and can be implemented without great difficulty in the SPH code. It should be mentioned, that in problems with a very large number of particles, this method causes a high computational cost.

The direct searching method is shown in the figure 3.5. As can be seen, all the particles with grey color, which have a smaller distance than kh are part of the neighbouring list of the particle i with black color.

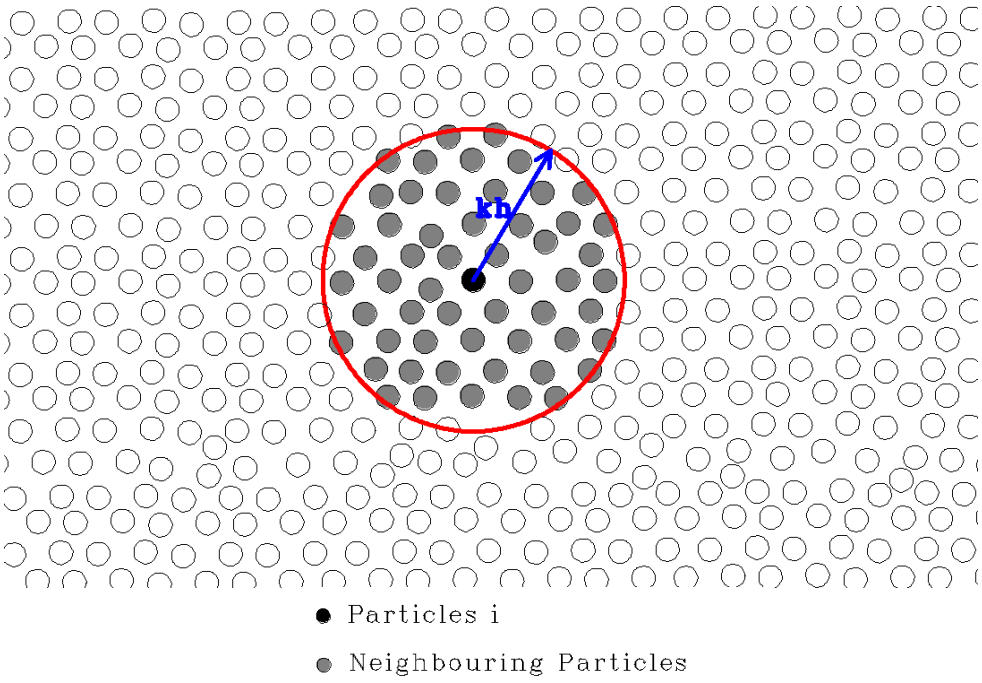

Figure 3.5: Direct Searching method to find the neighbouring particles of particle i in whole Domain

II. **Linked-Cell Neighboring List Method:** In problems with a large number of particles is preferable to use another technique as like as Linked-Cell method (Allen, 2004). In this method, the entire domain area will be divided into several rectangular grids. The grids have normally square form and called cell. These square cells have a side's length of kh, where h is the smoothing length and k is a constant number. kh is called cut-off limit. In many cases, k is assumed to be 2. Each particle is referenced in the simulation to a cell, that it belongs to (Chen, Lien, Peng, & Yee, 2020).

In this method, the neighbouring list for each particle have to be determined at each time steps, as like as direct searching method. But in Linked-Cell method, the searching for neighbouring particles of particle i will be carried out only for the cell, which particle i is located in this cell and the adjacent cell around of this cell and not in whole domain. In this approach, the cell-particle list must be

evaluated at each time steps and possibly to update the list at each time step too, because of the change of the position of particles at each time step. After assigning each particle to each cell, the searching of the neighbouring particles will be started.

By using this method, the computation cost of comparing particles with each other to create the neighbouring list will be reduced enormously, specially in the problems with very large domain.

In the picture below (figure 3.6), the Linked-Cell method is shown. The searching method for particle i with black color will be implemented only for the cells in adjacent the cell of particle i, that is shown in the graphic area with turquoise blue hatch. The neighbouring particles are shown with grey color.

With comparing the results of the neighbouring list of the direct searching and linked-cell methods can be seen that, the accuracy of the both methods are the same and just the efficiency and computation cost are different, especially in the problems with the high number of particles. In this research, the direct searching method is by reason of the ease in the implementation in the SPH code preferred and utilized.

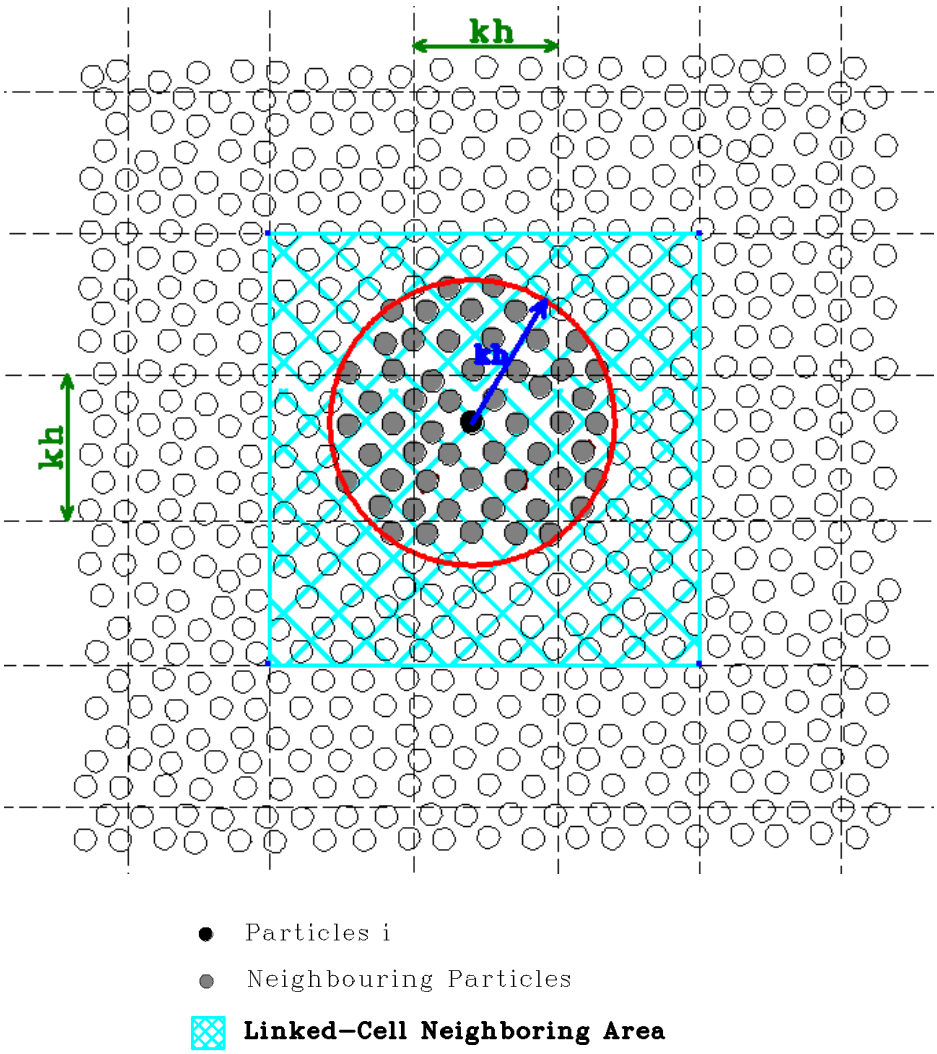

Figure 3.6: Linked-Cell Neighboring List Method to find the neighbouring particles of particle i in potential neighbouring particles at the adjacent cells

III. Verlet Neighboring List Method: As an alternative to Linked-Cell Neighboring List Method, in many SPH-Simulations, the Verlet Neighboring List Method is used. This approach has an advantage compared to another methods, that the Verlet neighbor list can be utilized for several time steps, however the update of the neighboring list after several time step is more expensive than Linked-Cell method.

In the Verlet method, a bigger cutoff radius than Linked-Cell method will be used. But only the neighboring particles with a distance smaller than kh will be employed in the contribution of the governing equations. By determining the neighboring particles of particle i at the beginning of the simulation alle possible neighboring particles in the next n time steps will be identified in a Verlet list. For each time step, a second list should be created as subset the Verlet list. Creating the second list are very low-cost, but it should be done at each time step to specify, which particles have to be contributed in the governing equations of SPH method. After n time steps, the Verlet List must be updated according to new position of particles.

The number of n time steps, that the Verlet list can be used without update is very dependent on the greatest occurring velocity in the model. Because of the change of the velocity over time in the simulation, the choose of the biggest occurring velocity and therefore choosing the correct number of the n time step has a great importance. If the velocity supposed to be small, so the computational cost increased and the efficiency of the simulation reduced. But if a bigger velocity is assumed, n time steps have to be reduced, otherwise the particles can leave the Verlet list before n time steps and the accuracy of the simulation will be impaired. By reducing the n time steps the advantage of using this method will be reduced enormously. For this reason, choosing the correct and optimal number of n time steps plays an important role in the efficiency of the model.

The Verlet method is specially suitable for the problems, which the occurring velocity are not far away from each other over time. In such problems, applying Verlet method can reduce the computational cost noticeably.

In the following picture (figure 3.7), the Verlet method is represented for particle i. As can be seen from the below figure, the cutoff radius to determining the Verlet list is assumed to be $kh + \Delta h$, as Δh defines as below (Domínguez, Crespo, Gómez-Gesteira, & Marongiu, 2010):

$$\Delta h = \zeta . (2V_{max} . n . dt) \tag{3.14}$$

where ζ is a safety parameter, which should be higher than 1. Commonly the safety factor will be assumed as 1.20. It should be noted that applying higher value of safety parameter increase the computational cost. V_{max} is the maximum possible occurring velocity of the particles in whole domain. The value of the V_{max} is doubled to consider the worst situation, when two neighbouring particles moving apart from each other with the maximum velocity. n is the number of the time steps, that the Verlet list will be kept. dt is the time step.

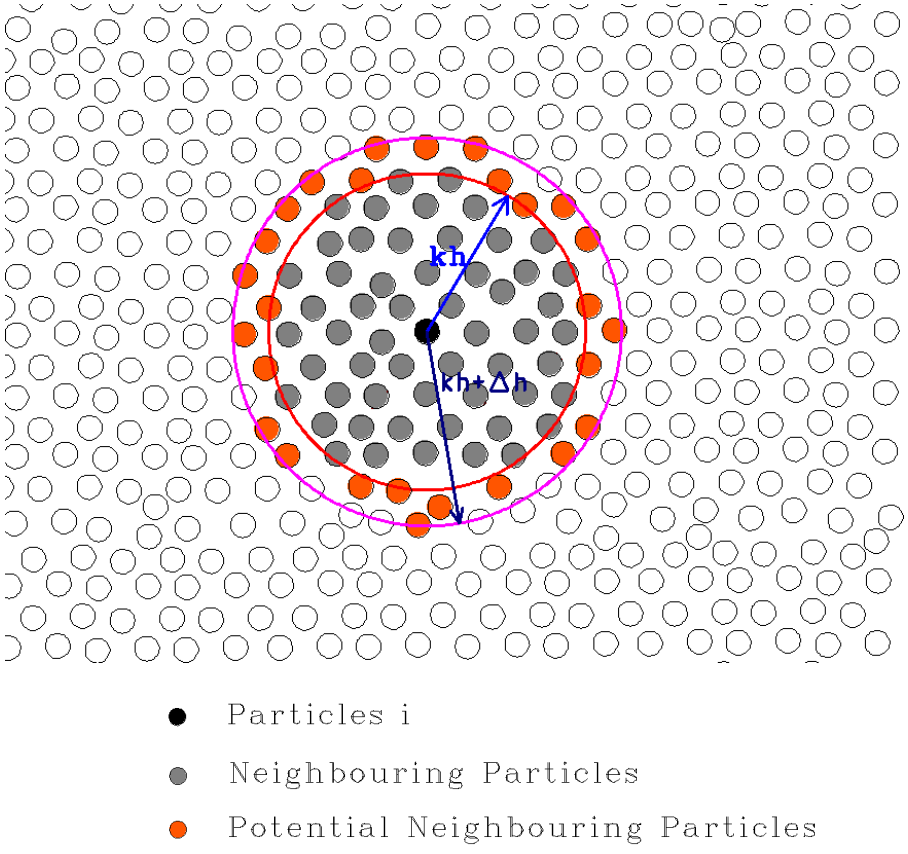

Figure 3.7: Verlet Neighboring and Verlet Potential List Method to find the neighbouring particles of particle i for several time steps

IV. Combination of Linked-Cell and Verlet Neighboring List Method: To use the advantage of the both methods Linked-Cell and Verlet neighbouring list, a combination of the both methods is utilized in several literatures. In the

combination method, at the beginning of the simulation, as shown in the figure 3.8, the whole domain will be divided into square grids and each particle will be assigned to a particular cell. After that, the Verlet list with a radius of $kh + \Delta h$ will be created, that will be kept for several time steps. In each time step, the second list as subset the Verlet list will specifying the neighbouring particles, which will be used in each time step in the contribution of the governing equation. Choosing the essential parameter is the same as what explained above for Linked-Cell and Verlet neighbouring list method.

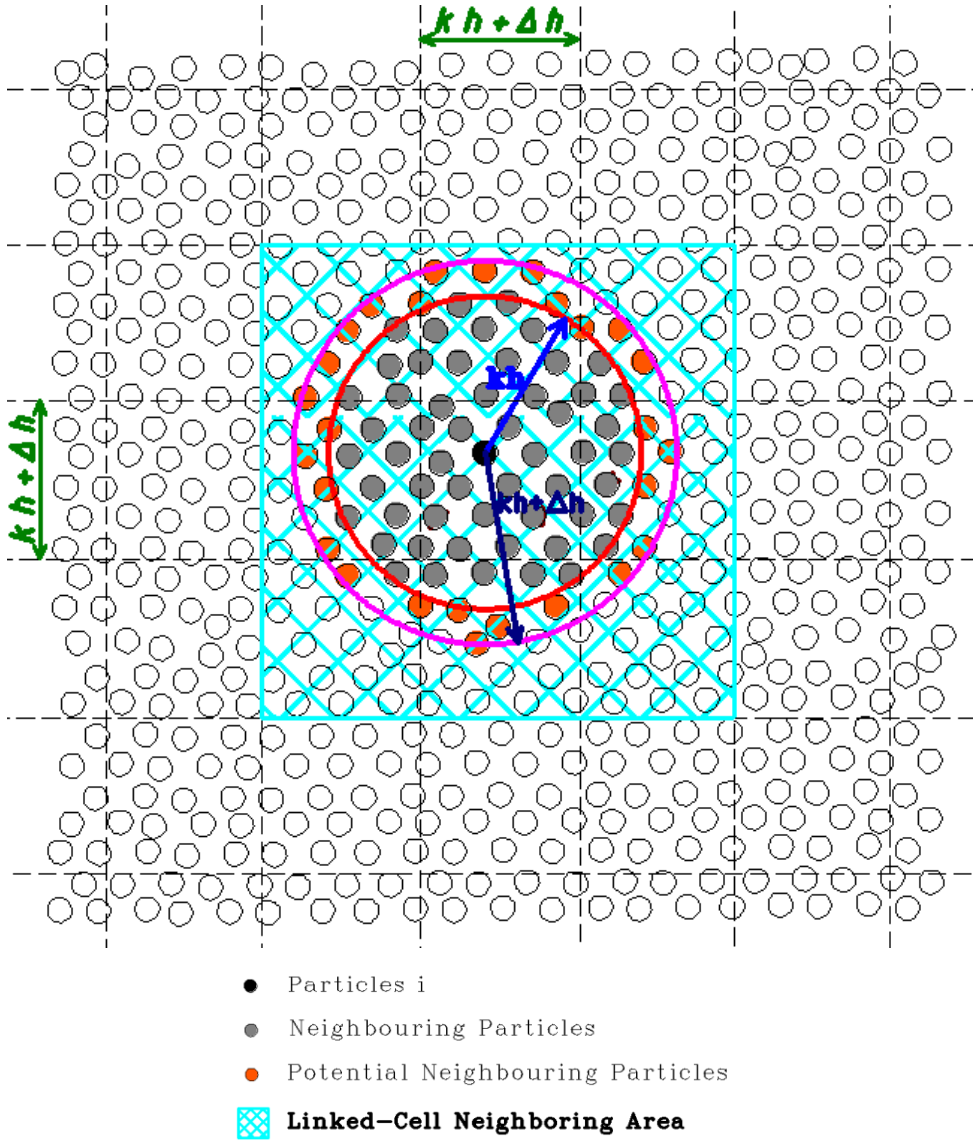

Figure 3.8: Combination of Linked-Cell and Verlet Neighboring List Method to find the neighbouring particles of particle i

3.7 Governing Equations in SPH

The governing equations based of physical laws of conservation of mass, momentum and energy. For description these governing equations in Lagrangian form of SPH, the partial differential equations (PDEs) will be discretized by Integral representation and Particle approximation to a set of ordinary differential equations (ODEs) with respect to time (Liu & Liu, 2003). In the next chapter, the SPH formulation will be derived according to the governing equations for the movement of water and soil.

4 Formulations of Smoothed Particle Hydrodynamics method

4.1 SPH model for water

Even though SPH-method was invented originally for modeling Astrophysics problems, it is extended in many researches to simulating free surface flow in computational fluid dynamics (CFD).

To simulating the fluid motion, it is common to assume fluid as incompressible or nearly incompressible flow (Monaghan J. , Simulating Free Surface Flows with SPH, 1994). In the present work, water is simulated as a viscous fluid with weak compressibility (Gholami Korzani, Galindo Torres, William, & Scheuermann, 2014).

4.1.1 SPH formulation of continuity equation

The governing equation of water is the famous Navier-Stokes equation.

In the SPH-method, the continuity equation will be used to conserving the mass. To considering the density in SPH calculation, two approach is used frequently (Monaghan J. , Simulating Free Surface Flows with SPH, 1994). In the first approach, the smoothed density will be calculated by summing over the neighboring particles according to following equation:

$$\rho_a = \sum_b m_b W_{ab} \tag{4.1}$$

where ρ_a is the density of particle a and m_b is the mass of neighboring particle b. W_{ab} is the interpolating kernel.

The above equation is not suitable for implementing fluid with free surface. Because of a lack of sufficient neighboring particles, this equation will give a low density for particles of free surface of fluid. The incorrect calculated density will cause an error in determining the pressure of fluid. For this reason, this equation isn't used in this research.

In the second approach, all particles will be assigned an initial density at beginning of the simulation. After that, the rate of change of the density of particles ($\frac{d\rho_a}{dt}$) will be estimated based on the following equation. Finally, the density of particles will be evolved in each time step.

$$\frac{d\rho_a}{dt} = \sum_b m_b (V_a - V_b).\nabla_a W_{ab} \tag{4.2}$$

where V_a is the velocity of particle a, V_b is the velocity of neighboring particle b, $\nabla_a W_{ab}$ denotes the gradient of interpolating kernel with respect to the coordinates of particle a.

4.1.2 SPH formulation of momentum equation

The Navier-Stokes equation of momentum is represented by Newton's second law and is responsible for conserving momentum in SPH problems (Liu & Liu, 2003). The governing equation for conservation of momentum in the Lagrangian frame is given by (Liu, Xie, & Liu, 2005)

$$\frac{Dv^\alpha}{Dt} = \frac{1}{\rho}\frac{\partial \sigma^{\alpha\beta}}{\partial x^\beta} \tag{4.3}$$

where v^{α} is the velocity component and the total stress tensor $\sigma^{\alpha\beta}$ consist of isotropic pressure P and viscous stress $\tau^{\alpha\beta}$. In some cases, the water will be considered as incompressible fluid without viscosity.

In such a circumstance, the momentum equation for particle a in a fluid is given by (Monaghan J. , 2012)

$$\frac{dv_a}{dt} = -\sum_b m_b \left(\frac{P_a}{\rho_a^2} + \frac{P_b}{\rho_b^2}\right).\nabla_a W_{ab}(b) + g_a \tag{4.4}$$

where P_a is the pressure at particle a, P_b is the pressure at neighboring particle b, ρ_a and ρ_b are the density of particle a and neighboring particle b respectively, g_a is considered as gravity or another external force.

There are other formulations of the momentum equation, in which the effect of the viscosity of water is taken into account. Three different methods are used frequently in modelling the problems with SPH method.

The first formulation is derived from the discretization of the Navier-Stokes equations and is given by (Holmes, Williams, & Tilke, 2011):

$$\begin{aligned}\frac{dv_a^{\alpha}}{dt} = &-\frac{1}{m_a}\sum_{b=1}^{N}\left(\frac{P_a}{n_a^2} + \frac{P_b}{n_b^2}\right)\frac{\partial W_{ab}}{\partial r_a^{\alpha}} \\ &+ \frac{1}{m_a}\sum_{b=1}^{N}\frac{(\mu_a + \mu_b)}{n_i n_j}(v_a^{\alpha} - v_b^{\alpha})\frac{\mathrm{r}_a^{\beta} - r_b^{\beta}}{\left|\mathrm{r}_a^{\beta} - r_b^{\beta}\right|^2}\frac{\partial W_{ab}}{\partial r_a^{\beta}} \\ &+ F_a^{\alpha}\end{aligned} \tag{4.5}$$

where μ is the dynamic viscosity and F_a^{α} is the body force applied on the particle a in the direction α. The particle number density term is defined as below:

$$n_a = \frac{\rho_a}{m_a} \tag{4.6}$$

Another Formulation is achieved by discretizing the SPH method, which is written as following (Tartakovsky, et al., 2016):

$$\frac{D(m_a v_a)}{Dt} = \sum_{b=1}^{N} -\left(\frac{P_b}{n_b^2} + \frac{P_a}{n_a^2}\right)\frac{\boldsymbol{r}_{ab}}{r_{ab}}\frac{dW(r_{ab}, h)}{dr_{ab}} + \sum_{b=1}^{N}\frac{4\mu_a\mu_b}{\mu_a + \mu_b}\frac{\boldsymbol{v}_{ab}}{n_a n_b r_{ab}}\frac{dW(r_{ab}, h)}{dr_{ab}} - \boldsymbol{F}_{ab}^{int} \tag{4.7}$$

Where molecular-like pairwise interaction force is defined by:

$$\boldsymbol{F}_{ab}^{int} = F(r_{ab})\frac{\boldsymbol{r}_{ab}}{r_{ab}} \tag{4.8}$$

In this work, another formulation is used, which shows good results in the simulation. Following formulation are utilized in the Fortran-code to simulate the viscosity of water in the momentum equation (Liu & Liu, 2003), (Pan, et al., 2016):

$$\frac{dv_a^\alpha}{dt} = \sum_b^N m_b\left(\frac{\sigma_a^{\alpha\beta}}{\rho_a^2} + \frac{\sigma_b^{\alpha\beta}}{\rho_b^2}\right).\frac{\partial W_{ab}}{\partial x_a^\beta} + f_a^\alpha \tag{4.9}$$

where $\sigma_a^{\alpha\beta}$ is the total stress tensor of the particle a and is defined as:

$$\sigma^{\alpha\beta} = -p\delta^{\alpha\beta} + \mu\dot{\varepsilon}^{\alpha\beta} \tag{4.10}$$

in the above equation, p is the isotropic pressure and μ is the dynamic viscosity. The shear strain rate $\dot{\varepsilon}^{\alpha\beta}$ takes the form as:

$$\dot{\varepsilon}^{\alpha\beta} = \sum_b^N \frac{m_b}{\rho_b}\left(v_b^\beta - v_a^\beta\right)\frac{\partial W_{ab}}{\partial x_a^\alpha} + \sum_b^N \frac{m_b}{\rho_b}\left(v_b^\alpha - v_a^\alpha\right)\frac{\partial W_{ab}}{\partial x_a^\beta} - \frac{2}{3}\sum_b^N \frac{m_b}{\rho_b}\left(v_b^\gamma - v_a^\gamma\right)\frac{\partial W_{ab}}{\partial x_a^\gamma}\delta^{\alpha\beta} \tag{4.11}$$

where N is the number of the neighboring particles of particle a.

Subsequently, the momentum equation of water with considering the viscosity is written as below:

$$\frac{Dv_a^\alpha}{Dt} = -\sum_{b=1}^{N} m_b \left(\frac{P_a}{\rho_a^2} + \frac{P_b}{\rho_b^2}\right)\frac{\partial W_{ab}}{\partial x_a^\alpha} + \sum_{b=1}^{N} m_b \left(\frac{\mu_a \varepsilon_a^{\alpha\beta}}{\rho_a^2} + \frac{\mu_b \varepsilon_b^{\alpha\beta}}{\rho_b^2}\right)\frac{\partial W_{ab}}{\partial x_a^\alpha} + g_a \quad (4.12)$$

In the simulated models in this research, the viscosity of water is assumed to be constant, therefore:

$$\mu_a = \mu_b \quad (4.13)$$

4.1.2.1 Equation of state

In order to modelling the water in SPH method, it is necessary to use an equation of state. Water should be modelled as a viscous fluid with weak compressibility (WCSPH), (Gholami Korzani M. , Galindo-Torres, Scheuermann, & J. Williams, 2016). In this work, the following equation of state is applied (Monaghan J. , SPH without a Tensile Instability, 2000):

$$P = B\left[\left(\frac{\rho}{\rho_0}\right)^\gamma - 1\right] \quad (4.14)$$

where

$$B = \frac{\rho_0 c_0^2}{\gamma} \quad (4.15)$$

where c_0 is the speed of sound, ρ_0 is the reference density and γ is taken as 7. Using the actual speed of sound in SPH formulation cause instability. To remove the instability, a very small time-step should be used, and it increases the computational cost significantly. In modeling of water as weakly compressible fluid, the speed of sound assumed to be greater than ten times the maximum fluid velocity ($c_0 > 10$ U). Therefore, a bigger time-step can be utilized in the numerical calculation without causing instability. This

technique ensures that the density variation of fluid remain less than 1% and the fluid behaves very close to physically incompressible fluid (Pereira, Prakash, & Cleary, 2011).

4.2 SPH model for Soil

Because of the elastic-plastic behavior of soil, the numerical simulation of soil is much more complex than water. To modeling soil in SPH method, the mass and momentum conservation equations are applied as governing equations of the soil. Different constitutive model are utilized to modeling the problems with SPH-method, as like as Drucker-Prager (Bui H. , Fukagawa, Sako, & Ohno, 2008), (Korzani, n.d.), hypoplastic (Peng, Wu, Yu, & Wang, 2015), Mohr-Coulomb failure criterion with applying equation of state for soil (Bui, Sako, & Fukagawa, 2007), original and modified Cam-Clay models (Nonoyama, Moriguchi, Sawada, & Yashima, 2015). Due to the more accurate results, the Drucker-Prager model with non-associated plastic flow rule is used in this study.

4.2.1 SPH formulation of continuity equation

The SPH formulation for evaluation of density of soil is similar to water. To distinguish water and soil particles from each other, the soil particles represented with subscripts i and j and water particles with subscripts a and b.

$$\frac{d\rho_i}{dt} = \sum_j m_j \left(V_i - V_j\right).\nabla_i W_{ij} \tag{4.16}$$

4.2.2 SPH formulation of momentum equation

The general form of SPH approximation of the momentum equation for defining of the soil particles is:

$$\frac{dv_i^\alpha}{dt} = \sum_j m_j \left(\frac{\sigma_i^{\alpha\beta}}{\rho_i^2} + \frac{\sigma_j^{\alpha\beta}}{\rho_j^2} \right) \frac{\partial W_{ij}}{\partial x_i^\beta} + f^\alpha \tag{4.17}$$

where f^α is the external force that is exerted to particles, $\sigma^{\alpha\beta}$ is the total stress tensor which divided into two parts:

I. an isotropic pressure p

II. a deviatoric shear stress $s^{\alpha\beta}$

$$\sigma^{\alpha\beta} = -p\delta^{\alpha\beta} + s^{\alpha\beta} \tag{4.18}$$

where $\delta^{\alpha\beta}$ is the Kronecker's delta:

$$\delta^{\alpha\beta} = \begin{cases} 1 & \alpha = \beta \\ 0 & \alpha \neq \beta \end{cases} \tag{4.19}$$

There are two usual ways to determine the isotropic pressure p in SPH-Formulation:

a. using equation of state: In this approach, the behavior of soil is assumed as elastic and will obey Hooke's law (Bui, Sako, & Fukagawa, 2007):

$$p = -K\frac{\Delta V}{V} = K\left(\frac{\rho}{\rho_0} - 1\right) \tag{4.20}$$

where K is the bulk modulus; ρ_0 is the initial density and $\Delta V/V$ is the volumetric strain.

b. using soil constitutive equation: In this method, the isotropic pressure will be calculated directly from the constitutive equation (Bui H. , Fukagawa, Sako, & Ohno, 2008), (Gholami Korzani M. , Galindo-Torres, Scheuermann, & Williams, 2018):

$$p = -\frac{\sigma^{\gamma\gamma}}{3} = -\frac{1}{3}(\sigma^{xx} + \sigma^{yy} + \sigma^{zz}) = K\varepsilon^{\gamma\gamma} \tag{4.21}$$

where $\varepsilon^{\gamma\gamma}$ is the volumetric strain, which is function of the actual soil displacement and $\sigma^{\gamma\gamma}$ is the summation of stress components in x, y and z direction (Kermani & Qiu, 2020).

To determine the deviatoric shear stress $s^{\alpha\beta}$, an elastic-perfectly plastic model is chosen in this study (Bui H. , Fukagawa, Sako, & Ohno, 2008).

For an elastic-perfectly plastic material, the total strain rate tensor $\dot{\varepsilon}^{\alpha\beta}$ consists of two parts: elastic strain rate tensor $\dot{\varepsilon}_e^{\alpha\beta}$ and plastic strain rate tensor $\dot{\varepsilon}_p^{\alpha\beta}$:

$$\dot{\varepsilon}^{\alpha\beta} = \dot{\varepsilon}_e^{\alpha\beta} + \dot{\varepsilon}_p^{\alpha\beta} \tag{4.22}$$

The elastic strain rate tensor will be calculated in according to Hooke's law as follows:

$$\dot{\varepsilon}_e^{\alpha\beta} = \frac{\dot{s}^{\alpha\beta}}{2G} + \frac{1-2\nu}{3E}\dot{\sigma}^{\gamma\gamma}\delta^{\alpha\beta} \tag{4.23}$$

where $\dot{\boldsymbol{s}}^{\boldsymbol{\alpha\beta}}$ is the deviatoric shear stress rate tensor, G is the shear modulus, ν is Poisson's ratio, E is Young's modulus and $\dot{\boldsymbol{\sigma}}^{\boldsymbol{\gamma\gamma}}$ is summation of three normal components:

$$\dot{\sigma}^{\gamma\gamma} = \dot{\sigma}^{xx} + \dot{\sigma}^{yy} + \dot{\sigma}^{zz} \tag{4.24}$$

To calculate the strain rate tensor, the plastic flow rule is used as follows:

$$\dot{\varepsilon}_p^{\alpha\beta} = \dot{\lambda}\frac{\partial g_p}{\partial \sigma^{\alpha\beta}} \tag{4.25}$$

where g_p is the plastic potential function and $\dot{\lambda}$ is the rate of change of the so-called plastic multiplier λ, which is dependent on the state of stress and load history.

Granular materials changing their volume under shear. Thus, for numerical modelling of the soil, usually the non-associated flow rule with considering the dilatancy is selected (Wang, Wang, Peng, & Meng, Dilatancy and compaction effects on the submerged granular column collapse, 2017). It means, that the plastic potential function g is not

coincident with the yield function Y of material. As yield function to calculate the plastic flow regime of soil in this study, the Drucker-Prager (Drucker & Prager, 1952) (Alejano & Bobet, 2012) yield criterion is employed. The plastic deformation happens, when the following equation is satisfied as follows (Wu, An, & Liu, 2015):

$$Y(I_1,J_2) = \sqrt{J_2} + \alpha_\phi I_1 - k_c = 0 \tag{4.26}$$

where I_1 and J_2 are the first and second invariants of the stress tensor respectively:

$$I_1 = \sigma^{xx} + \sigma^{yy} + \sigma^{zz} \tag{4.27}$$

$$J_2 = \frac{1}{2} s^{\alpha\beta} s^{\alpha\beta} \tag{4.28}$$

α_ϕ and k_c are Drucker-Prager's constants, which are defined for plane-strain condition as follows (Bui, Kodikara, Bouazza, Haque, & Ranjith, A novel computational approach for large deformation and post-failure analyses of segmental retaining wall systems, 2014):

$$\alpha_\phi = \frac{\tan\phi}{\sqrt{9 + 12\tan^2\phi}} \tag{4.29}$$

$$k_c = \frac{3c}{\sqrt{9 + 12\tan^2\phi}} \tag{4.30}$$

where ϕ is internal friction and c is cohesion of soil.

The non-associated plastic flow rule can be defined as follows (Nguyen, Bui, & Fukagawa, 2013):

$$g_p = \alpha_\psi I_1 + \sqrt{J_2} - constant \tag{4.31}$$

where α_ψ is a dilatancy factor and can be defined the same as α_ϕ.

The plastic potential function g_p for non-associated flow rule is chosen in the following form:

$$g_p = \sqrt{J_2} + 3I_1 \sin\psi \tag{4.32}$$

where ψ is the dilatancy angle and if $\psi = 0$, the material is plastically incompressible.

After discretizing of soil constitutive equation in the SPH framework, the stress-strain relationship for the non-associated flow rule soil model for particle i in the SPH formulation can be summarized as follows (Bui H. , Fukagawa, Sako, & Ohno, 2008), (Gholami Korzani M. , www.m2clab.com, n.d.):

$$\frac{D\sigma_i^{\alpha\beta}}{Dt} = \sigma_i^{\alpha\gamma}\dot{\omega}_i^{\beta\gamma} + \sigma_i^{\gamma\beta}\dot{\omega}_i^{\alpha\gamma} + 2G\dot{e}_i^{\alpha\beta} + K\dot{\varepsilon}_i^{\gamma\gamma}\delta_i^{\alpha\beta} - \dot{\lambda}_i\left[9K\sin\psi\,\delta^{\alpha\beta} + \frac{G}{\sqrt{J_2}}s_i^{\alpha\beta}\right] \tag{4.33}$$

where the rate of change of plastic multiplier $\dot{\lambda}_i$ for particle i defined as below:

$$\dot{\lambda}_i = \frac{3\alpha K\dot{\varepsilon}_i^{\gamma\gamma} + (G/\sqrt{J_2})s_i^{\alpha\beta}\dot{\varepsilon}_i^{\alpha\beta}}{27\alpha_\phi K\sin\psi + G} \tag{4.34}$$

where $\dot{\varepsilon}^{\gamma\gamma}$ is the summation of the three normal strain-rate components (Wang & Chan, 2014)

$$\dot{\varepsilon}^{\gamma\gamma} = \dot{\varepsilon}^{xx} + \dot{\varepsilon}^{yy} + \dot{\varepsilon}^{zz} \tag{4.35}$$

also is K the elastic bulk modulus:

$$K = \frac{E}{3(1-2\nu)} \tag{4.36}$$

and G is the shear modulus:

$$G = \frac{E}{2(1+\nu)} \tag{4.37}$$

In order to solve the above soil constitutive equation with SPH-method, the strain and spin rate tensors is discretized into SPH formulation too:

$$\dot{\varepsilon}^{\alpha\beta} = \frac{1}{2}\left(\frac{\partial v^{\alpha}}{\partial x^{\beta}} + \frac{\partial v^{\beta}}{\partial x^{\alpha}}\right) = \tag{4.38}$$

$$\frac{1}{2}\left[\sum_{j=1}^{N}\frac{m_j}{\rho_j}\left(v_j^{\alpha} - v_i^{\alpha}\right)\frac{\partial W_{ij}}{\partial x_i^{\beta}} + \sum_{j=1}^{N}\frac{m_j}{\rho_j}\left(v_j^{\beta} - v_i^{\beta}\right)\frac{\partial W_{ij}}{\partial x_i^{\alpha}}\right]$$

$$\dot{\omega}^{\alpha\beta} = \frac{1}{2}\left(\frac{\partial v^{\alpha}}{\partial x^{\beta}} - \frac{\partial v^{\beta}}{\partial x^{\alpha}}\right) = \tag{4.39}$$

$$\frac{1}{2}\left[\sum_{j=1}^{N}\frac{m_j}{\rho_j}\left(v_j^{\alpha} - v_i^{\alpha}\right)\frac{\partial W_{ij}}{\partial x_i^{\beta}} - \sum_{j=1}^{N}\frac{m_j}{\rho_j}\left(v_j^{\beta} - v_i^{\beta}\right)\frac{\partial W_{ij}}{\partial x_i^{\alpha}}\right]$$

For implementing large deformation problems in the SPH method, it is necessary to define a relationship between the tensors of strain rate and stress rate. In this study, the Jaumann Stress Rate is utilized (Bui H. , Fukagawa, Sako, & Ohno, 2008), (Huang, Dai, & Zhang, 2014):

$$\hat{\dot{\sigma}}^{\alpha\beta} = \dot{\sigma}^{\alpha\beta} - \sigma^{\alpha\gamma}\dot{\omega}^{\beta\gamma} - \sigma^{\gamma\beta}\dot{\omega}^{\alpha\gamma} \tag{4.40}$$

where $\hat{\dot{\sigma}}^{\alpha\beta}$ is the Jaumann stress rate.

The two-dimensional Jaumann stress rate defines as follows (Huang, Dai, & Zhang, 2014):

$$\dot{\sigma}_{xx} = \hat{\sigma}_{xx} + 2\omega_{xy}\sigma_{yx} \tag{4.41}$$

$$\dot{\sigma}_{yy} = \hat{\sigma}_{yy} - 2\sigma_{xy}\omega_{xy} \tag{4.42}$$

$$\dot{\sigma}_{xy} = \hat{\sigma}_{xy} - \sigma_{xx}\omega_{xy} + \sigma_{yy}\omega_{xy} \tag{4.43}$$

4.3 SPH model for simulation of the seepage force in saturated soil

To model the movement of water in saturated soil, two separate phases must be defined: water and soil phases. In this approach, each phase is defined parallel but separate from another phase and calculating of continuity and momentum equations were carried out separately. The interaction between water and soil is implemented by adding the seepage force as an external force into momentum equation of water and soil. The seepage force is defined by Darcy's law (Bui, Sako, & Fukagawa, 2007):

$$f_{seepage} = \gamma_w n \frac{(v_{water} - v_{soil})}{k_s} \tag{4.44}$$

where k_s denotes the soil permeability, n is porosity of the soil and γ_w is the unit weight of water.

The seepage force will be added to momentum equation of soil and water separately. Because of naturally existence of pore water in saturated soil, the effect of pore water pressure will be considered in the soil momentum equation.

Finally, the momentum equation for saturated soil and water defined as follows:

Momentum equation for soil phase:

$$\begin{aligned} \frac{dv_i^\alpha}{dt} = \sum_{j=1}^{N} m_j \left(\frac{\sigma_i^{\alpha\beta}}{\rho_i^2} + \frac{\sigma_j^{\alpha\beta}}{\rho_j^2} \right) \frac{\partial W_{ij}}{\partial x_i^\beta} + f_i^\alpha \\ + \sum_{a=1}^{N} m_a \frac{f_{ia}^{seepage}}{\rho_i \rho_a} W_{ia} \\ - \sum_{a=1}^{N} m_a \frac{p_a}{\rho_i \rho_a} \frac{\partial W_{ia}}{\partial x_i^\alpha} \end{aligned} \tag{4.45}$$

Momentum equation for water phase:

$$\frac{dv_a^\alpha}{dt} = \sum_{b=1}^{N} m_b \left(\frac{\sigma_a^{\alpha\beta}}{\rho_a^2} + \frac{\sigma_b^{\alpha\beta}}{\rho_b^2} \right) \frac{\partial W_{ab}}{\partial x_a^\beta} + f_a^\alpha - \sum_{a=1}^{N} m_a \frac{f_{ia}^{seepage}}{\rho_i \rho_a} W_{ia} \tag{4.46}$$

where W_{ia} is the interpolating kernel between soil particle i and water particle a.

4.4 Speed of sound

To increase the value of time step and reduce the computing cost, the speed of sound, that used in the standard SPH, is chosen very slower than the physical speed of sound (Bui H. , Fukagawa, Sako, & Ohno, 2008). The speed of sound in the granular will be estimated from the following equation (Nguyen, Nguyen, Bui, Nguyen, & Fukagawa, 2016), (Fa´vero Neto & Borja, 2018):

$$c = \sqrt{E/\rho} \tag{4.47}$$

where E bulk modulus and ρ is the density of the granular material.

4.5 Stability of the model

In numerical simulations, it happens often that some particles are unstable. They obtain a large velocity and with high force leave the domain through the boundary particles. These situations will be prevented by using some methods as like as artificial viscosity, return mapping algorithm, choosing appropriate time step etc.

4.5.1 Artificial Viscosity

The artificial viscosity will be used to prevent the fluctuation in the flow. The artificial viscosity term will be added to the physical pressure term in the momentum equation to help to diffuse of the large variation in the model and to dissipate of high frequency terms (Liu & Liu, 2003). By adding the artificial viscosity, the momentum equation will be rewritten as:

$$\frac{dv_i^{\alpha}}{dt} = \sum_j m_j \left(\frac{\sigma_i^{\alpha\beta}}{\rho_i^2} + \frac{\sigma_j^{\alpha\beta}}{\rho_j^2} + \Pi_{ij} \right) \frac{\partial W_{ij}}{\partial x_i^{\beta}} + f^{\alpha} \tag{4.48}$$

where Π_{ij} is given by Monaghan (Monaghan J. , Smoothed Particle Hydrodynamics, 1992) as follows:

$$\Pi_{ij} = \begin{cases} \dfrac{-\alpha \overline{c_{ij}} \mu_{ij} + \beta \mu_{ij}^2}{\overline{\rho_{ij}}} & v_{ij}.r_{ij} < 0; \\ 0 & v_{ij}.r_{ij} > 0; \end{cases} \tag{4.49}$$

and

$$\mu_{ij} = \frac{h v_{ij}.r_{ij}}{r_{ij}^2 + \eta^2} \tag{4.50}$$

where η^2 is assumed to prevent the denominator from being zero, when r_{ij} is zero. Therefore, the above equation can be rewritten as below:

$$\mu_{ij} = \frac{h v_{ij}.r_{ij}}{r_{ij}^2 + 0.01h^2} \tag{4.51}$$

α and β are two constants, that their values will be chosen between 0 and 2.50. $\overline{c_{ij}}$ is the average of the sound speed of particle i and j.

4.5.2 Return mapping algorithm

Numerical errors are commonly found in the computational calculation and sometimes it is required, that a correction algorithm be added in the program. In such a circumstance, the stress state of soil can exceed the apex of the yield function or it can lie away from the yield surface. These errors lead to an unrealistic behavior of soil. To prevent occurring such problems, two following procedures, that earlier was applied in the finite element codes, will be customized for using in SPH-method (Chen & Mizuno, 1990), (Bui H. , Fukagawa, Sako, & Ohno, 2008):

a. Tension cracking treatment:

If the stress state of soil, throughout the calculation, exceeds the apex of the yield surface, it causes unrealistic behavior of soil as like as fracture or forming clumps of the particles. These numerical errors are very similar to tensile instability in SPH methods, that commonly occurred in the tensile regime (Swegle, Hicks, & Attaway, 1995).

If the stress state exceeds the apex of the yield surface (as like as stress state of a particle, which because of the occurring numerical error, instead of position E has moved to position F, as shown in der following Figure 4.1. Here, the stress state of the particle has to be corrected with utilizing tension cracking treatment), which corresponds to the following condition:

$$-\alpha_{\phi} I_1^n + k_c < 0 \tag{4.52}$$

where

$$I_1^n = \sigma_n^{xx} + \sigma_n^{yy} + \sigma_n^{zz} \tag{4.53}$$

The stress state of the particle should be corrected with shifting the hydrostatic stress component considering the following equation (Bui H. , Fukagawa, Sako, & Ohno, 2008):

$$\widetilde{\sigma_n^{xx}} = \sigma_n^{xx} - \frac{1}{3}\left(I_1^n - \frac{k_c}{\alpha_\phi}\right) \tag{4.54}$$

$$\widetilde{\sigma_n^{yy}} = \sigma_n^{yy} - \frac{1}{3}\left(I_1^n - \frac{k_c}{\alpha_\phi}\right) \tag{4.55}$$

$$\widetilde{\sigma_n^{zz}} = \sigma_n^{zz} - \frac{1}{3}\left(I_1^n - \frac{k_c}{\alpha_\phi}\right) \tag{4.56}$$

$$\widetilde{\sigma_n^{xy}} = \sigma_n^{xy} \tag{4.57}$$

$$\widetilde{\sigma_n^{xz}} = \sigma_n^{xz} \tag{4.58}$$

$$\widetilde{\sigma_n^{yz}} = \sigma_n^{yz} \tag{4.59}$$

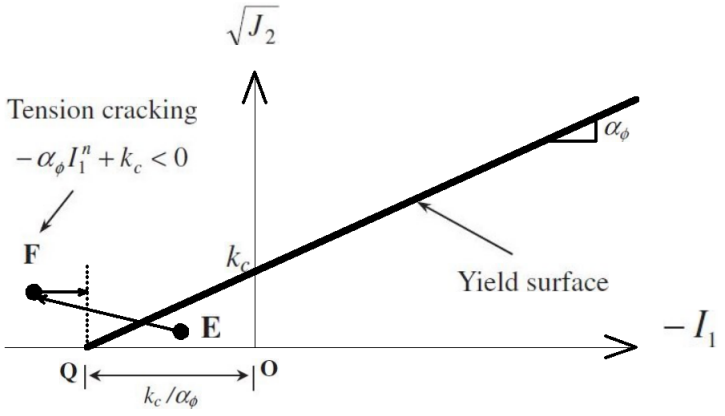

Figure 4.1: Return mapping algorithm: Tension cracking treatment (Bui H. , Fukagawa, Sako, & Ohno, 2008), (Copyright © 2008 John Wiley & Sons, Ltd.)

b. Scale-back procedure:

There are situations, where the stress state of particle exceeds the yield surface, although in the plastic deformation, the stress state of the particle must always lie on the yield surface (as stress state of a Particle, which due to the numerical error, from position A

moved to position B, as illustrated in der following Figure 4.2, here the stress state of the particle must be returned on the yield surface, by means of a scaling-back procedure). In such cases, a scale-back procedure have to be used, by that the stress state of particle lie again on the yield surface. In such a circumstance, for the Drucker-Prager yield criterion, following scaling factor must be utilized, thereby the errors will be corrected:

$$r^n = \frac{-\alpha_\phi I_1^n + k_c}{\sqrt{J_2^n}} \tag{4.60}$$

In the Drucker-Prager yield criterion, if

$$-\alpha_\phi I_1^n + k_c < \sqrt{J_2^n} \tag{4.61}$$

it means that a numerical error occurred and the stress state of the particle exceeded the yield surface. With using the following equations, the stress state can be corrected and an unrealistic behavior of soil and instability of the model is prevented:

$$\widetilde{\sigma_n^{xx}} = r^n s_n^{xx} + \frac{1}{3} I_1^n \tag{4.62}$$

$$\widetilde{\sigma_n^{yy}} = r^n s_n^{yy} + \frac{1}{3} I_1^n \tag{4.63}$$

$$\widetilde{\sigma_n^{zz}} = r^n s_n^{zz} + \frac{1}{3} I_1^n \tag{4.64}$$

$$\widetilde{\sigma_n^{xy}} = r^n s_n^{xy} \tag{4.65}$$

$$\widetilde{\sigma_n^{xz}} = r^n s_n^{xz} \tag{4.66}$$

$$\widetilde{\sigma_n^{yz}} = r^n s_n^{yz} \tag{4.67}$$

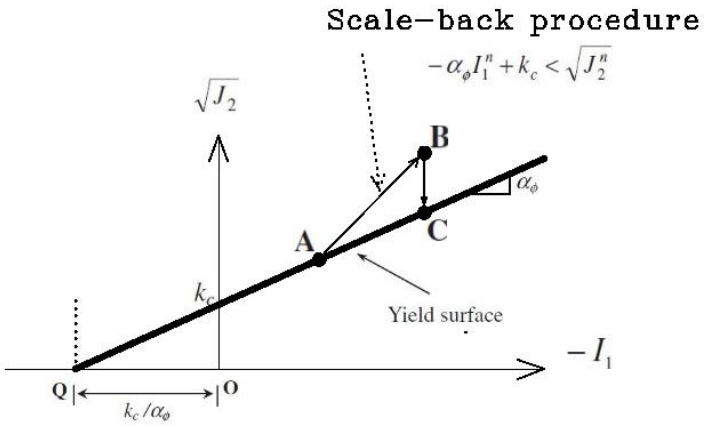

Figure 4.2: Return mapping algorithm: Scale-back procedure
(Bui H. , Fukagawa, Sako, & Ohno, 2008), (Copyright © 2008 John Wiley & Sons, Ltd.)

4.5.3 Time Integration

In each numerical simulation, the choice of the appropriate time step plays an important role. Using large time step causes instability in the model and choosing small time step increases the computing cost. To have a stable model, following criteria should be satisfied (P. Morris, J. Fox, & Zhu, 1997), (Peng, et al., 2019):

1. Courant-Friedrichs-Lewy condition:

$$\Delta t \leq \chi \min\left(\frac{h}{c}, \sqrt{\frac{h}{\max\|a_i\|}}\right) \tag{4.68}$$

where χ is the CFL coefficient and is normally chosen between 0.05 – 0.25, h is the smoothing length and c is the sound speed, that depends on the material's stiffness. The particle acceleration in the above equation is defined as follow:

$$a_i \leq \frac{dv_i}{dt} \tag{4.69}$$

where v_i is the velocity of the particle i.

2. Viscous diffusion condition:

$$\Delta t \leq 0.125 \frac{h^2}{\nu_k} \tag{4.70}$$

where ν_k is kinematic viscosity.

They are different methods to integrating of the discrete SPH equation such as Runge-Kutta, Leapfrog, velocity-Verlet scheme and predictor-corrector (Liu & Liu, 2003). In this study, the velocity-Verlet scheme is used (Adami, Hu, & Adams, 2012), (Beeman, 1976):

$$\rho^{n+\frac{1}{2}} = \rho^n + \frac{\Delta t}{2}\left(\frac{d\rho^n}{dt}\right) \tag{4.71}$$

$$v^{n+\frac{1}{2}} = v^n + \frac{\Delta t}{2}\left(\frac{dv^n}{dt}\right) \tag{4.72}$$

$$\rho^{n+1} = \rho^n + \Delta t\left(\frac{d\rho^n}{dt}\right) \tag{4.73}$$

$$v^{n+1} = v^n + \Delta t\left(\frac{dv^{n+\frac{1}{2}}}{dt}\right) \tag{4.74}$$

$$x^{n+1} = x^n + \Delta t v^{n+1} \tag{4.75}$$

4.6 Moving the particles

To determine the moving of particles, following equation is used widely:

$$\frac{dr_a}{dt} = v_a \tag{4.76}$$

There is a method to add a correction term to the above equation in order to improve the movement of particles, so that the particles, which are close together, will be moved with almost identical velocities. This method called XSPH and defines as below (Monaghan J. , On the Problem of Penetration in Particle Methods, 1989), (Monaghan J. , Smoothed Particle Hydrodynamics, 1992):

$$\frac{dr_a}{dt} = v_a + \varepsilon \sum_b m_b \left(\frac{V_{ba}}{\bar{\rho}_{ab}}\right) W_{ab} \tag{4.77}$$

where

$$\bar{\rho}_{ab} = \frac{(\rho_a + \rho_b)}{2} \tag{4.78}$$

$$V_{ba} = v_b - v_a \tag{4.79}$$

and ε is a constant number, which is between 0 and 1.

XSPH correction method is specially helpful in simulation of weakly incompressible fluids such as water, in which the viscosity in the simulation of water was ignored.

Furthermore, using XSPH correction stabilize the particles at free surface and help to prevent the unphysical penetration (Wang, Riaz, & Balachandran, 2020).

4.7 Initial Stress and Boundary conditions

4.7.1 Define Initial Stress of soil

Defining initial stress is an import part of numerical modelling. Applying inappropriate initial stress causes unrealistic results. There are two usual methods to assigning initial stresses in soil (Bui & Fukagawa, An improved SPH method for saturated soils and its application to investigate the mechanisms of embankment failure: Case of hydrostatic pore-water pressure, 2013):

a. K_0 method: This method is suitable for geometry of soil with horizontal surface. In this method, the total vertical and horizontal stresses is calculated with considering groundwater level and earth pressure coefficient $K_0 = (1 - \sin\phi)$ in accordance with the theoretical methods. The results are assigned as initial stresses in each problem.

b. Gravity loading method: In this method the initial vertical and horizontal stresses were calculated by using soil self-weight loading in the first phase of problem's modeling. Ba applying this method, the non-horizontal ground surface can be simulated.

It should be pointed out that the initial stress of the soil boundary particles will be assigned identical as the neighbouring real soil particles, which have the similar elevation in the geometry of the problem.

4.7.2 Boundary conditions in SPH

Boundary particles are responsible to avoid the penetration of real particles and therefore preventing real particles leave the domain. Defining the boundary conditions in SPH-method is very important. In this method, the continuum und momentum equations for each particle is calculated for the neighboring particles and there are no neighboring particles from outside for the particles near the boundary, which causes inaccuracy in estimating the kernel summation for these particles (Randles & Libersky, 1996). Therefore, without defining a suitable boundary, errors are arisen in the calculation of the

particles near or on the boundary. In the following figures 4.3 and 4.4 are shown, that in the boundary region the kernel function W has no effect and the contribution of the particles near the boundary are incomplete.

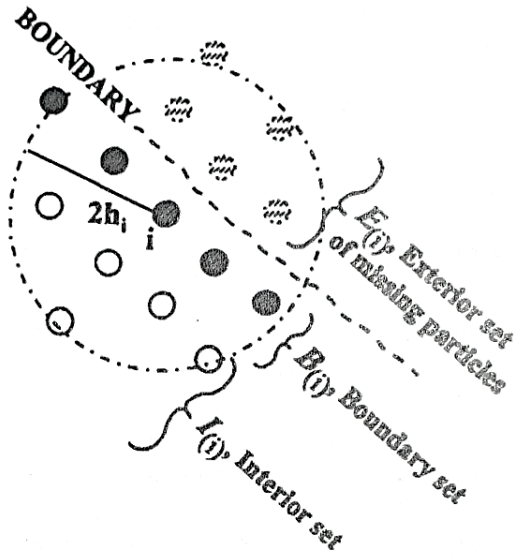

Figure 4.3: Missing particles in the kernel sum for the particles near the boundary (reprint from (Randles & Libersky, 1996))

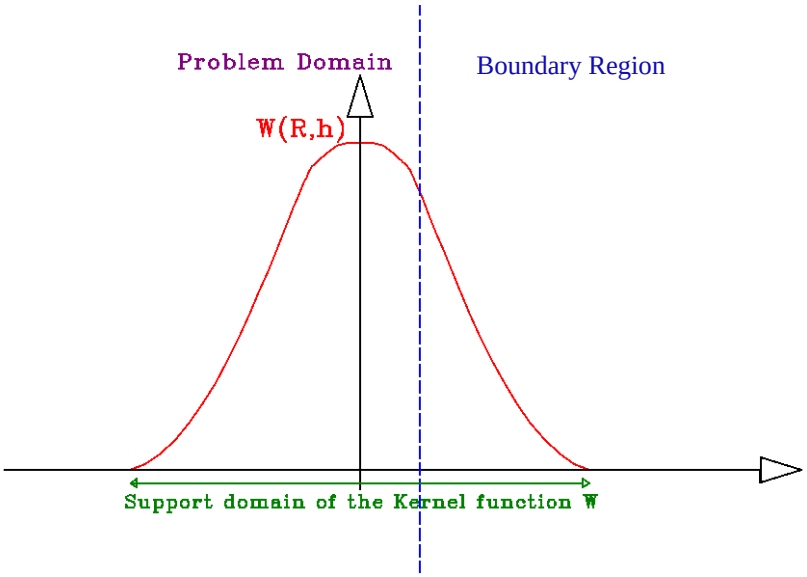

Figure 4.4: Incomplete estimation of the kernel sum for the particles near the boundary

To overcome the boundary problem, that mentioned above, the boundary in the simulation builds up from a set of virtual particles. They are three main methods to treat these boundary particles:

I. Repulsive force method: In this method, a series of virtual particles will be set on the boundary. These particles have a distance von Δx from the real particles, where Δx is the initial spacing. When a real particle approaching the boundary, the boundary particles exert central force on this particle. Then the real particle cannot penetrate in the boundary. The repulsive force between real and boundary particles has the Lennard-Jones form (Liu & Liu, 2003), (Monaghan J. , Simulating Free Surface Flows with SPH, 1994):

$$f(r) = \begin{cases} D\left[\left(\frac{r_0}{r_{ij}}\right)^{P_1} - \left(\frac{r_0}{r_{ij}}\right)^{P_2}\right]\frac{x_{ij}}{r_{ij}^2} & \frac{r_0}{r_{ij}} \leq 1 \\ 0 & \frac{r_0}{r_{ij}} > 1 \end{cases} \tag{4.80}$$

where D is a problem dependent parameter, that should be equal to square of the greatest speed. P_1 and P_2 can be chosen as 12 and 4. The cutoff distance r_0 is usually taken equal to initial particle spacing.

The initial spacing of the virtual boundary particles can be chosen Δx or $\Delta x/2$. In order to produce enough repulsive force in problems with higher velocity, it is recommended to assign $\Delta x/2$ to the initial distance between boundary particles as shown in the figure 4.5.

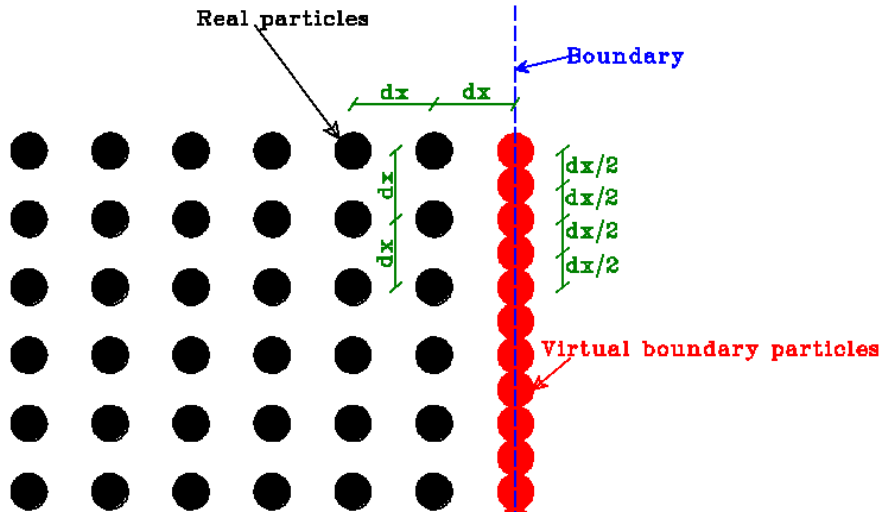

Figure 4.5: **Initial set up the virtual boundary particles in the Repulsive force method**

II. Ghost or mirror particles: Ghost particles are fictitious particles, which are generated in each time step and ensure the boundary condition. Ghost particles are produced by reflections of the real particles, as shown in the following figure 4.6, which are near or on the boundary (Libersky, Petschek, Carney, Hipp, & Allahdadi, 1993). By contributing the mirror particles in the governing equation, the inaccuracy near the boundary because of the lack of the boundary particles will be removed and results zero velocity on the Boundary.

The utilizing of the mirror boundary to implement the problems with complex geometries arises difficulties in the simulation (Chow, Rogers, Lind, & Stansby, 2018).

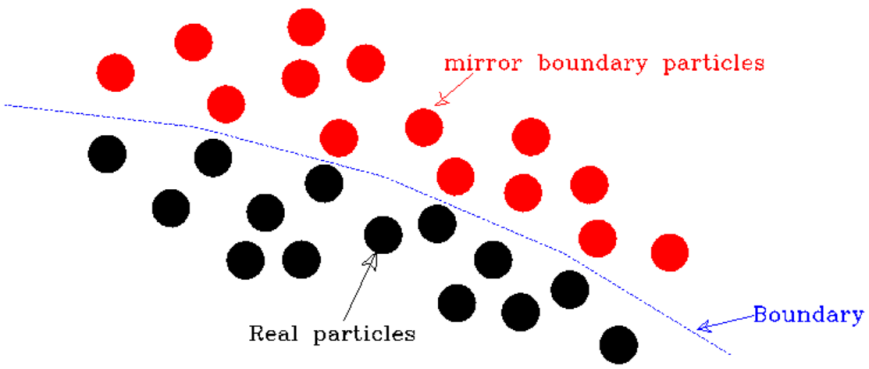

Figure 4.6: **Schema of mirror boundary particles**

III. fixed boundary particles: This type of boundary particle would be called also as imaginary (Takeda, M. Miyama, & Sekiya, 1994) or virtual (Jin, Zheng, Duan, & Niu, 2015) particles. In this method, three layers of boundary particles are set parallel to the boundary. The first layer of boundary particles are placed ($\frac{\Delta x}{2}$) from the boundary. Each boundary particle has a distance of Δx from another boundary particle. The first layer of real particles near the boundary is arranged as well ($\frac{\Delta x}{2}$) from the boundary. This has been illustrated in the figure 4.7:

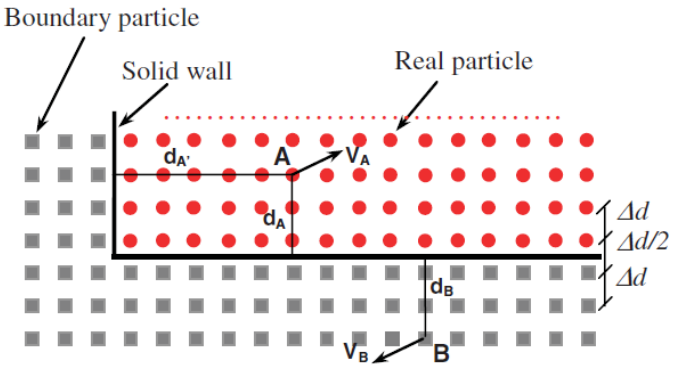

Figure 4.7: **Arrangement of boundary particles (reprint from (Bui H. , Fukagawa, Sako, & Ohno, 2008))**

In this study, after trying different methods, fixed boundary particle method is applied to simulate the boundary particles. The fixed boundary particles contribute in continuum and momentum calculations, but they will not move. To contribute in the governing equation of SPH, each boundary particles must have the essential quantities of material. In the developed Fortran-code, the initial mass of real particles is assigned to the boundary particles at the beginning of calculation. This value will not be changed throughout the simulation. In order to contribute the boundary particles in the continuity equation, the initial density will be assigned to boundary particles at each time step. Thereafter, by implementing the SPH continuity equation, the density of real and boundary particles are evolved at each time step.

The velocity of boundary particles is not determined as like as real particles. To achieve the no-slip boundary condition, the artificial velocity method is utilized (Bui H. , Fukagawa, Sako, & Ohno, 2008), (P. Morris, J. Fox, & Zhu, 1997). The velocity of boundary particle B is calculated at each time step as follows:

$$v_B = -(\frac{d_B}{d_A})v_A \tag{4.81}$$

If real particle A gets too close to boundary, d_A will be very small and as a result, the velocity of boundary particle B increases greatly. To avoid such a numerical error, the velocity of boundary particles can be obtaining from following equation:

$$v_B = (1-\beta)v_A \tag{4.82}$$

where

$$\beta = \min\left(\beta_{max}, 1.0 + \frac{d_B}{d_A}\right) \tag{4.83}$$

Choosing $\beta_{max} = 1.5 - 2.0$ shows good results. In this study, $\beta_{max} = 1{,}50$ shows mostly good results.

Another quantity in modelling of soil is stress. Here, it is assumed that the stress is distributed locally uniformly on the boundary. Therefore, the stress of boundary particles in each time step is assigned according to (Bui H. , Fukagawa, Sako, & Ohno, 2008):

$$\sigma_B^{\alpha\beta} = \sigma_A^{\alpha\beta} \tag{4.84}$$

For contributing the boundary particles in momentum equation of water, pressure value should be assigned to boundary particles at each time step. The pressure value will be estimated as follows (Adami, Hu, & Adams, 2012):

$$P_B = \frac{\sum P_A W_{BA} + g \sum \rho_A r_{BA} W_{BA}}{\sum W_{BA}} \tag{4.85}$$

By using the above equation, the density of boundary particles can be accordingly obtained:

$$\rho_B = \rho_0 \left(\frac{P_B}{B} + 1 \right)^{\frac{1}{\gamma}} \tag{4.86}$$

where

$$B = \frac{\rho_0 c_0^2}{\gamma} \tag{4.87}$$

5 Validation and Verification

In order to simulate the problems with SPH-method, a Fortran-Code is developed as a part of this study. With this code, different geotechnical problems with dry as well as saturated soil can be simulated. In this code, the soil and water has been coupled to each other in order to model the movement of porous water in soil too. In what follows, this code is validated by means of comparing the results of simulations with some benchmark experiments.

5.1 Failure process of non-cohesive soil

The simulation of collapse of granular material is because of the transition from solid-like to fluid-like behaviors is complicated (Fern & Soga, 2017). In order to validate the ability of SPH method and the Fortran-Code to simulate the geotechnical problems with large deformation, a two-dimensional soil collapse of non-cohesive soil (sand) is hereby modelled. The result of this simulation is compared with the experiment, which was carried out by Bui et al. (Bui H. , Fukagawa, Sako, & Ohno, 2008).

In the experiment, a rectangular soil model with the dimensions of 200 mm x 100 mm is utilized, which 200 mm is the length of the model and 100 mm is the height of the model.

In order to have a better visualization of the soil model, a square grids paper of 50 mm x 50 mm is installed in the background of the experiment.

As described in the previous chapter, the elastic-perfect plastic model and the Drucker-Prager yield criterion is employed to calculate the stress in the soil model.

The required parameters of the soil model were obtained by conducting a shear box test. In the SPH constitutive equations, the same values are used, which are obtained of the test.

To utilize the SPH method to solve this problem, firstly the domain has to be discretized into particles. To choosing the number of particles, it is very important to notice the calculating cost. Using more particles bring higher resolution, but the calculating time increased enormously.

To define the boundary, the fixed boundary particles with considering the no-slip boundary condition for the base and the wall is applied

The initial setting and the dimensions of the numerical model is shown in der following drawing (figure 5.1):

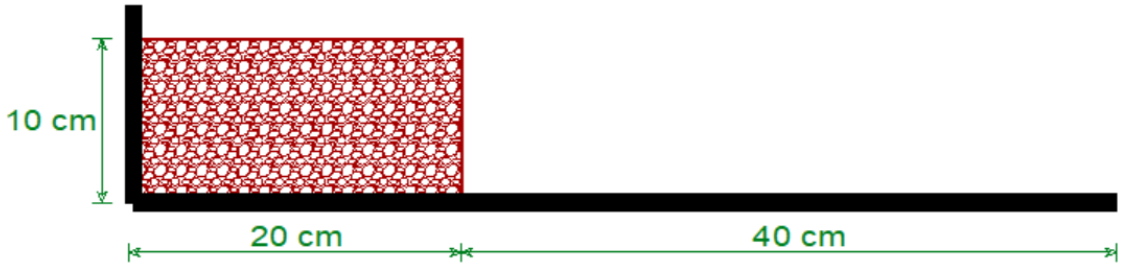

Figure 5.1: Initial setting of the problem "Failure process of non-cohesive soil"

The applied parameters and the initial conditions of the simulation are presented in the following table 5.1:

Table 5.1: Initial setup parameters of the numerical simulation of the problem "Failure process of non-cohesive soil"

initial length of the soil model [m]	0.20
initial height of the soil model [m]	0.10
number of real particles	5000
number of neighboring particles	1080
Initial particle spacing [m]	0.001
density of sand ρ_{soil} [kg/m³]	2650
Young's Modulus E [MPa]	0.84
internal friction angle ϕ [Degree]	19.8
cohesion c [kPa]	0.0
dilatancy angle ψ [Degree]	3.0
Poisson's ratio υ	0.30
time step dt [s]	0.00002
total time [s]	0.40
background mesh spacing [m]	0.05
Processor (computing)	Intel® Core™ i7-6700T CPU @ 2.80GHz
Computing time [hour]	13,0

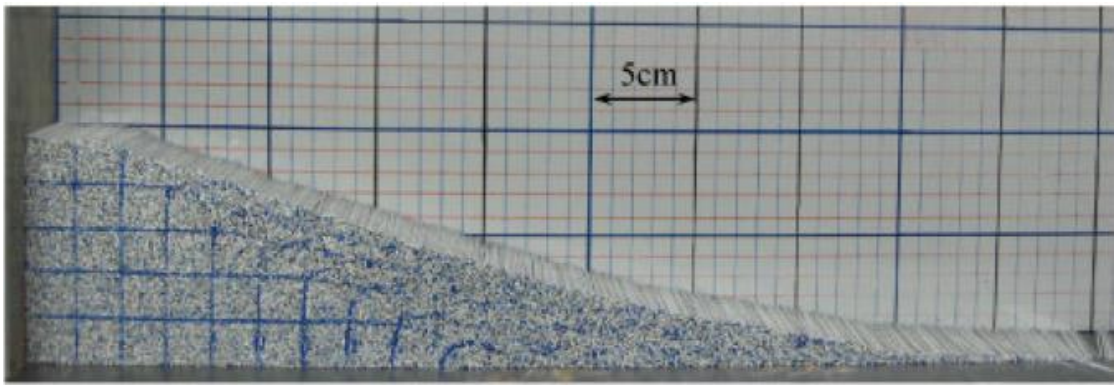

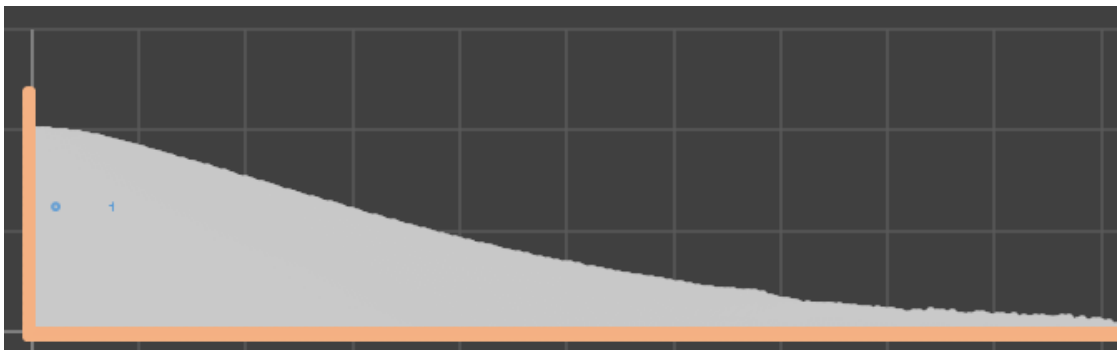

t=0.40 s

Figure 5.2: Compare between the experiment's results and the results of the numerical simulation of the problem "Failure process of non-cohesive soil"

In the presented figure 5.2, the results of the numerical simulation are shown. By comparing these results with the experiment, it can be seen that the numerical results have a very good agreement with the benchmark experiment's results. These results of this simulation present clearly the ability of the SPH method to modelling the geotechnical problems with large deformation. Hereby no mesh is used and therefore exists no difficulty with defining a large domain and the particles can move freely in accordance with their governing equations in the whole of the domain.

5.2 Spreading of a granular mass on a horizontal plane

The behavior of the granular material is complex. The granular material has a different behavior in different conditions. For example, in static loading they behave as like as a solid but by dynamic conditions they behave as same as fluid (Dávalos, Cante, Hernández, & Oliver, 2015). The same granular material shows different behavior, if they are transported by wind as a suspension of particles in air (Thompson & Huppert, 2007). Because of this complexity and usage of granular material in industry, the modelling of granular material is an interesting topic for many researchers.

In order to validate the developed Fortran-Code for simulating the granular material, the experiments of spreading granular mass on horizontal plane with different dimensions, which was carried out by Lajeunesse et al. 2004 (Lajeunesse, Mangeney-Castelnau, & Vilotte, 2004) are simulated.

In this experiment a cylindrical pile of dry granular material with different initial aspect ratios was suddenly released to spread on a horizontal plane. In this experiment, the glass beads are used as granular material.

To implement the experiment with various initial ratio, the inner radius R_i and the height H_i are varied in the initial setup. The initial aspect ratio α is defined as below:

$$\alpha = \frac{H_i}{R_i} \tag{5.1}$$

To allow the granular column to spread on the plane, the cylinder tube was removed suddenly by means of a lifting system, that was constructed of rope and pulleys. The experiment is done on a plane with the dimensions of 600 x 600 mm. In the following sketch (figure 5.3) the initial scheme of the experiments' setup is illustrated.

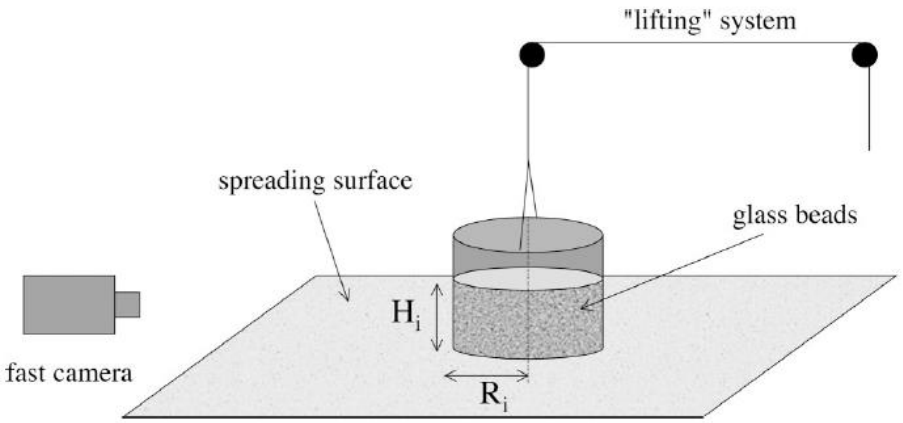

Figure 5.3: Initial setup of the experiment "spreading granular mass on horizontal plane" (reprint from (Lajeunesse, Mangeney-Castelnau, & Vilotte, 2004))

In order to compare the results of the numerical simulation, the same geometry as like as the experiments are employed in the numerical models. Therefore, three models are simulated with three initial aspect ratios of 0.56, 0.80 and 5.40 as like as the experiments. In the experiment, glass beads are used, but in these numerical models, sand as granular material is utilized in order to show that the behavior of the granular material is independent of the applied material. In fact, the final shape and the behavior of the granular material is only depended on the initial aspect ratio of the model (Staron & Hinch, 2005). Furthermore, the lifting velocity in the experiment is given 1.6 m/s. But this lifting velocity does not fit properly to the experiment's results. In the results, the position of the cylinder tube can be recognized. By the numerical simulation, it was found out, that by applying smaller lifting velocity, the position of the tube in different time interval and the results of the simulations are identical with the experiment's results. In the following table 5.2, the applied initial setting parameters for simulation of each case are presented:

Table 5.2: Initial setup parameters of the numerical simulation of the problem "Spreading granular mass on horizontal plane"

Initial aspect ratio	$\alpha = 0.56$	$\alpha = 0.80$	$\alpha = 5.40$

inner radius of the column R_i [mm]	70.50	70.50	28.00
Height of the column H_i [mm]	39.48	56.40	151.20
number of real particles	9672	14100	8640
number of neighboring particles to model the underneath the cylinder	1800	1800	1500
number of neighboring particles to model cylinder tube	108	154	436
Initial particle spacing [m]	0.00075	0.00075	0.0015
density of sand ρ_{soil} [kg/m³]	2500	2500	2500
Young's Modulus E [MPa]	0.80	0.80	0.80
internal friction angle ϕ [Degree]	35.0	35.0	29.0
cohesion c [kPa]	0.0	0.0	0.0
dilatancy angle ψ [Degree]	1.0	1.0	1.0
Poisson's ratio υ	0.35	0.35	0.25
lifting velocity [m/s]	0.30	0.30	1.60
time step dt [s]	0.00002	0.00002	0.00002
total time [s]	0.648	0.540	0.512
Processor (computing)	Intel® Core™ i7-6700T CPU @ 2.80GHz		
Computing time [hour]	6,0	9,25	4,0

Hereinafter, the results of the numerical simulation compared to the experiment's results are presented (figures 5.4 to 5.6, Experiment's results are reprinted from (Lajeunesse, Mangeney-Castelnau, & Vilotte, 2004):

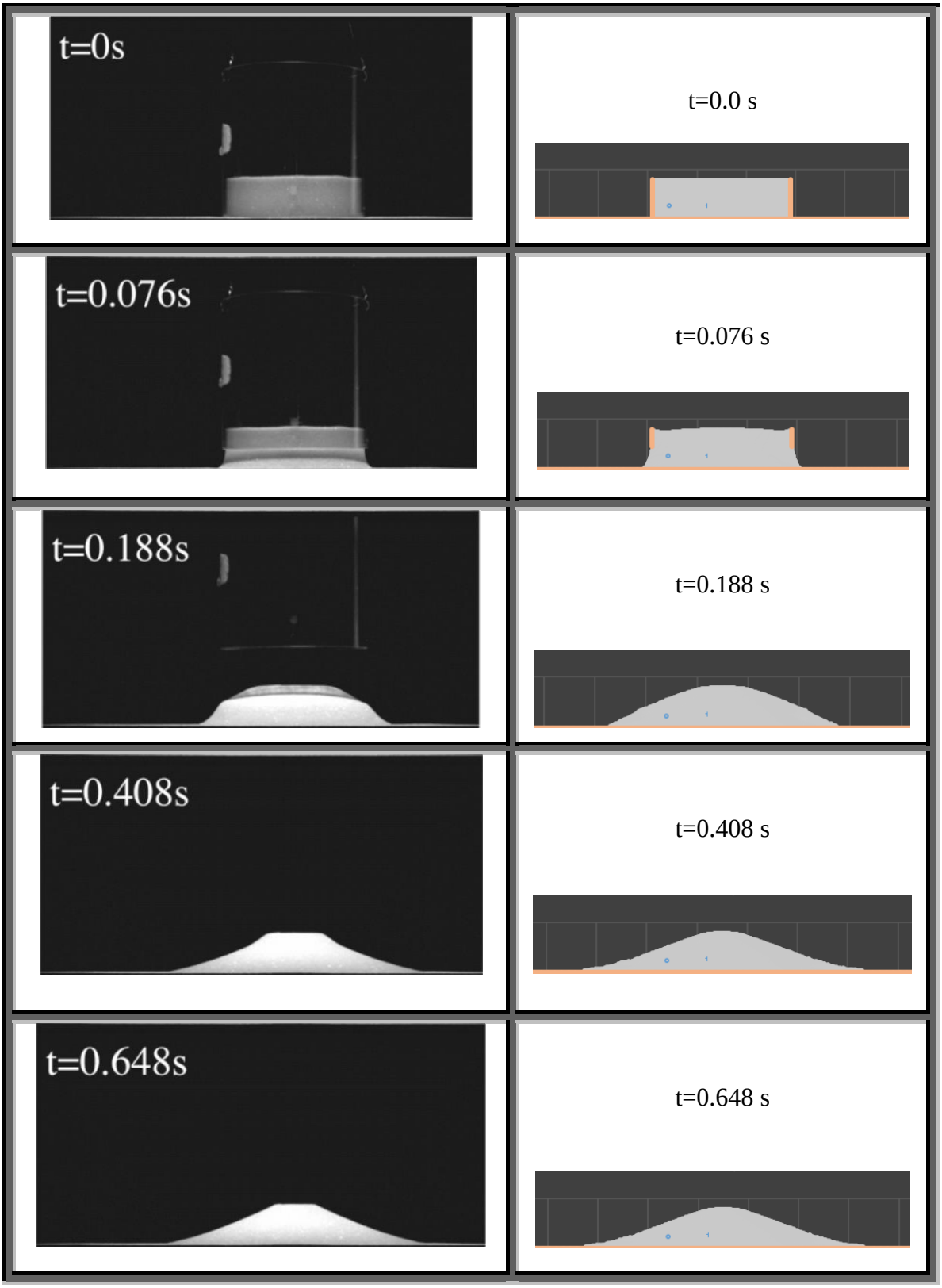

Figure 5.4: Comparing the results of the simulation and experiment of the problem "Spreading granular mass on horizontal plane with initial aspect ratio α=0.56" Left results reprint from (Lajeunesse, Mangeney-Castelnau, & Vilotte, 2004)

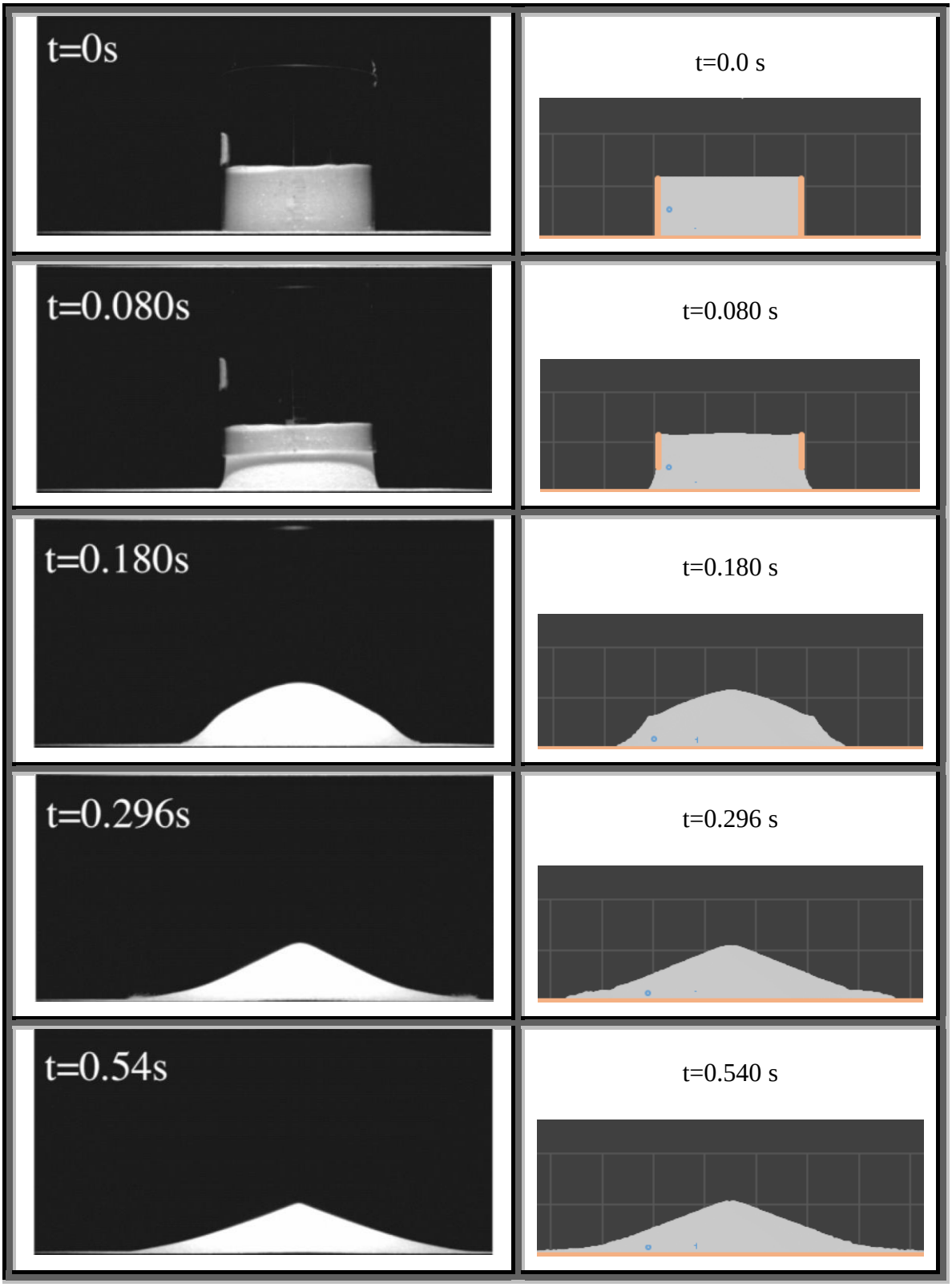

Figure 5.5: Comparing the results of the simulation and experiment of the problem "Spreading granular mass on horizontal plane with initial aspect ratio α=0.80" left results reprint from (Lajeunesse, Mangeney-Castelnau, & Vilotte, 2004)

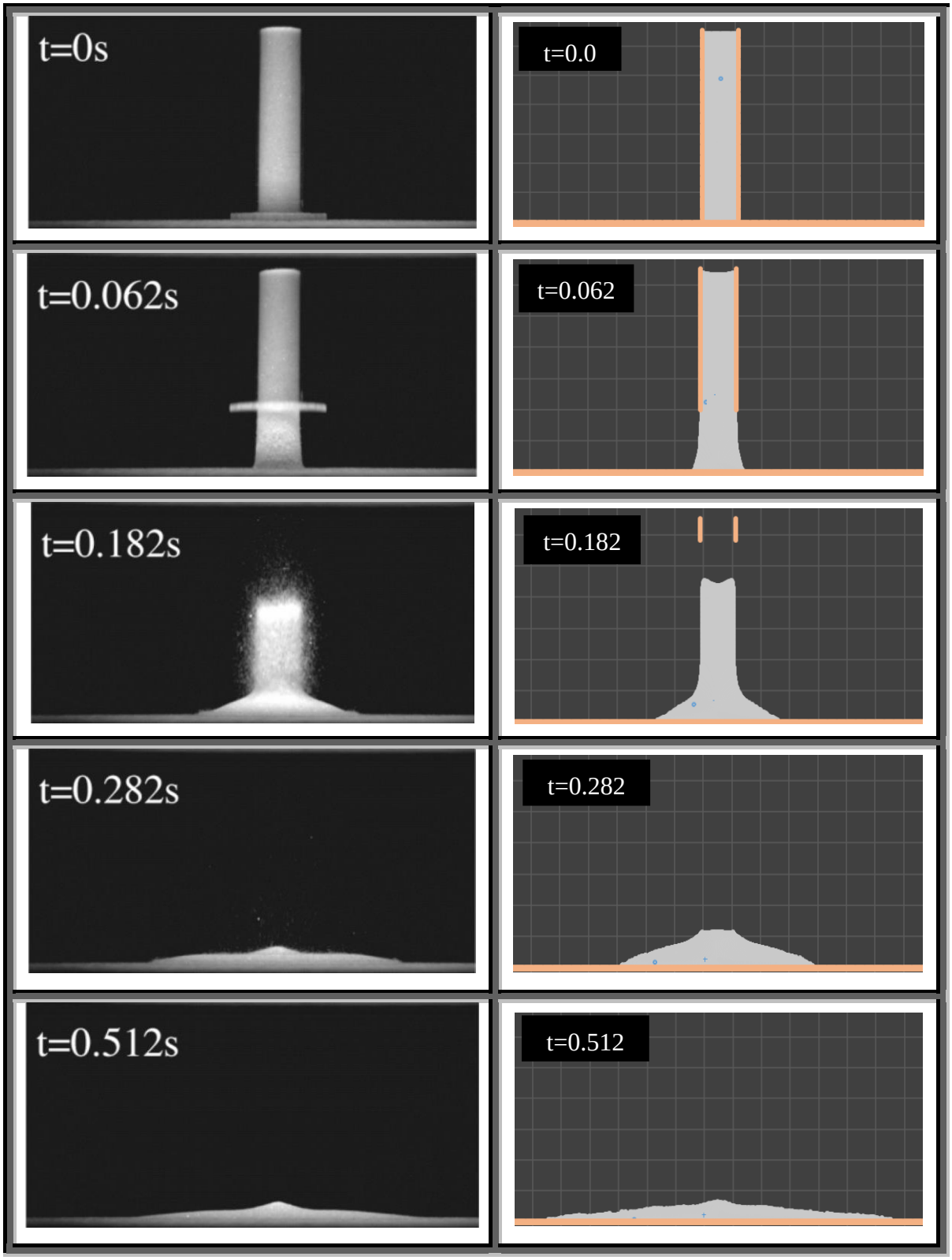

Figure 5.6: Comparing the results of the simulation and experiment of the problem "Spreading granular mass on horizontal plane with initial aspect ratio α=5.40" left results reprint from (Lajeunesse, Mangeney-Castelnau, & Vilotte, 2004)

By comparing the results of the simulation with the experiment's results, it can be seen that, a very good agreement between simulation and experiment is by the aspect ratios 0.56 and 0.80 available. Although the used material in experiment was glass beads and, in the simulation, sand is used, but the results are nearly the same. Also, it proved that the behavior of the granular material is independent of the used material. By the initial aspect ratio of 5.40 exists a little difference in the middle the simulation, but at the end of the simulation the results are identical as well and have a very good agreement with the experiment.

5.3 Collapse of a water-saturated granular column into water

In natural and hazardous phenomena, the collapse of the granular materials in dry and submerged situation are frequently occurred. They are many processes as like as submarine landslide, debris flows, etc. in that the collapse and movement of fluid and granular materials are connected with each other (Wang, Wang, Peng, & Meng, Dilatancy and compaction effects on the submerged granular column collapse, 2017). In such phenomena, the interaction between fluid and granular material has to be considered in analyze as well as in the simulation and modelling such problems.

Because of the complexity of the interaction between fluid and granular materials, the simulation of the collapse of the saturated granular materials is an interesting topic for many researchers. Furthermore, the accurate prediction of such catastrophic events is very important for risks assessment. It should be noted that, because of the huge mass transport and high velocity of such phenomena, it is almost very difficult to carry out a proper experiment in laboratory, which its results are adequate reliable to predict a real phenomenon in nature (Rondon, Pouliquen, & Aussillous, 2011).

For this reason, the Fortran-Code in this study is also expanded for modelling the two-phase problems in order to be able to consider the movement of soil and water simultaneously in different problems.

To validate the code, some benchmark experiments are chosen to compare with the numerical simulation. The first experiment is the collapse of a water-saturated sand column into water, that was carried out in the Cambridge University (Thompson & Huppert, 2007). The aspect ratio in this study is considered as initial height to horizontal extent of the column.

In the selected experiment, the saturated sand was released in a tank of depth 150 mm and depth of 600 mm by lifting a Perspex wall. The tank is full with water. The column has an initial height of 250 mm and initial width of 120 mm.

This problem is simulated with the same geometry and the same initial and boundary conditions as like as experiment. The only difference is the length of the tank, which is considered 500 mm based on the results of the experiment and in order to save the computational time.

The initial setting and the dimensions of the numerical model is shown in der following drawing (figure 5.7):

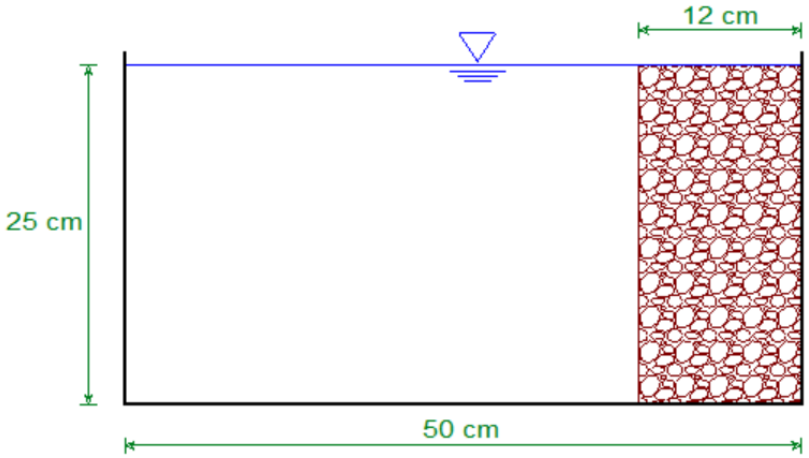

Figure 5.7: Initial setup of the numerical model of the problem "Collapse of a water-saturated granular column into water"

In the simulation of this experiment, the following setup initial parameters has been applied (table 5.3):

Table 5.3: Initial setup parameters of the numerical simulation of the problem "Collapse of a water-saturated granular column into water"

initial height of the sand column $[m]$	0.25
initial depth of the sand column $[m]$	0.12
initial height of the water in the tank $[m]$	0.25
initial depth of the water in the tank $[m]$	0.50
number of real soil particles	528

number of real water particles	2211
number of neighboring soil particles	273
number of neighboring water particles	429
initial particle spacing for water and soil $[m]$	0.0075
density of sand ρ_{soil} $[kg/m^3]$	2650
density of water ρ_{water} $[kg/m^3]$	1000
Young's Modulus of soil E $[MPa]$	25.0
internal friction angle of sand ϕ $[Degree]$	30.0
cohesion c [kPa]	0.0
dilatancy angle of soil $\psi[Degree]$	1.20
Poisson's ratio υ	0.30
permeability of soil k_s $[m/s]$	0.001
porosity of soil n	0.35
time step dt $[s]$	0.00004
total time $[s]$	17.0
Processor (computing)	Intel® Core™ i7-6700T CPU @ 2.80GHz
Computing time [hour]	7,50

In the figure 5.8, the experiment's results and the results of the numerical simulation of this are presented:

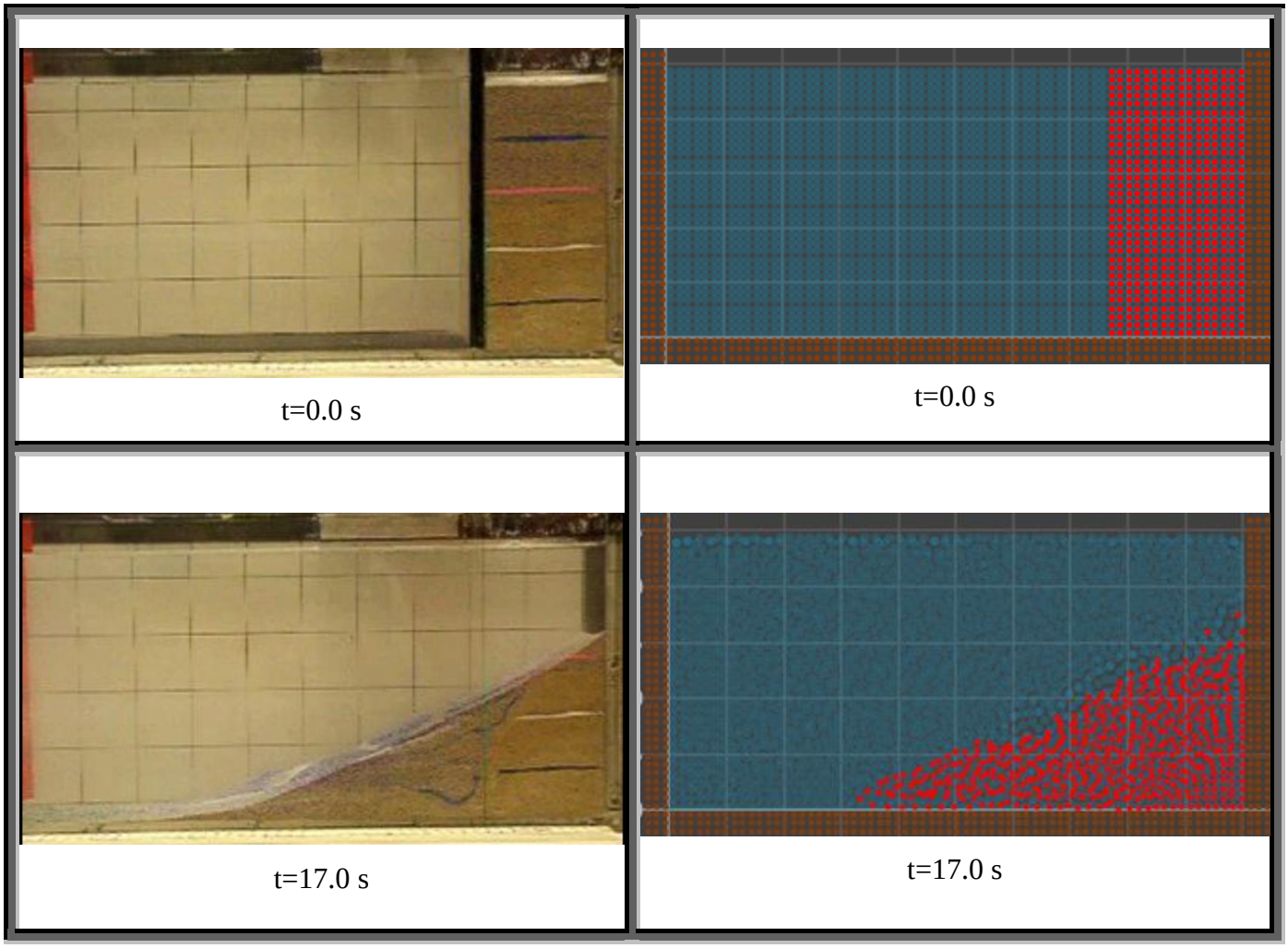

Figure 5.8: Compare between the experiment's results (reprint from (Thompson & Huppert, 2007)) and the results of the numerical simulation of the problem "Collapse of a water-saturated granular column into water"

By comparing the results of the simulation and the experiment's result can be recognized that a relatively good agreement is achieved. Therefore, the results show the ability of the developed code to simulate the problems with water and soil.

5.4 Hydraulic heave

To construct an excavation pit in the areas with high groundwater level, occurring the hydraulic heave is a normal problem. By developing the pore water pressure because of the seepage flow, the excavation base could be lifted and causes the stability loss of the excavation pit (Koltuk & Azzam, Design Charts for Circular-Shaped Sheeted Excavation Pits against Seepage Failure by Heave, 2016). The hydraulic heave happens, when the effect of the seepage pressure exceeds the existing resistance, which is normally the weight of the soil body. In other words, if the pore water pressure at the bottom of the heave zone is equal or greater than the total normal stress at this level the hydraulic heave occurs (Koltuk, Song, Iyisan, & Azzam, 2019). In the figure 5.9 the hydraulic heave is illustrated:

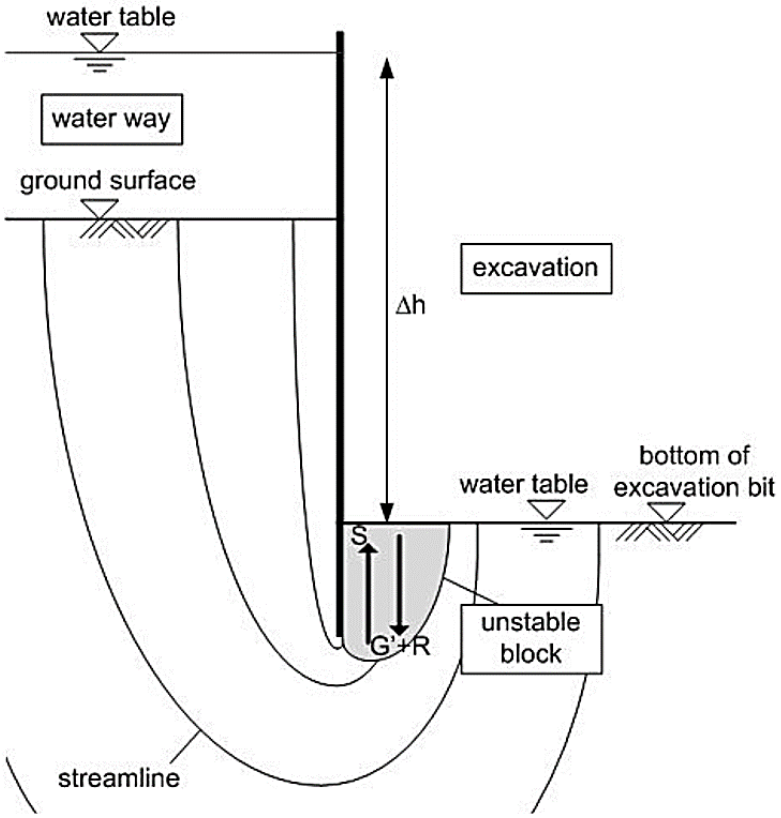

Figure 5.9: Description of the hydraulic heave (reprint from (Schober, Boley, & Odenwald, 2011))

Furthermore, the width of the hydraulic heave in non-cohesive soil is according to Terzaghi & Peck (1961) approximately half of the embedded length (Aulbach, Ziegler, & Schüttrumpf, Design Aid for the Verification of Resistance to Failure by Hydraulic Heave, 2013). In the figure 5.10, the width of the heave in accordance with the embedded length illustrated:

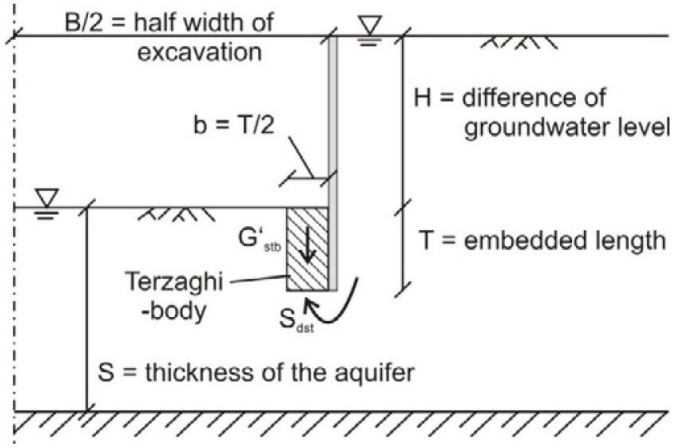

Figure 5.10: Schematic illustration of the hydraulic heave (reprint from (Aulbach, Ziegler, & Schüttrumpf, Design Aid for the Verification of Resistance to Failure by Hydraulic Heave, 2013))

Because of the importance of the hydraulic heave in construction of the deep foundation and need to predict the behavior of the soil for various conditions, many experiments and numerical simulations are done. For this reason, this problem is also chosen as a benchmark experiment in this study in order to validate the developed Fortran-Code.

As a benchmark, an experiment is chosen, which was done in RWTH Aachen University in Germany (Aulbach & Ziegler, Versagensform und Nachweisformat beim hydraulischen Grundbruch –Plädoyer für den Terzaghi-Körper, 2014). In this experiment, the tank is divided into two parts, which are connected from the lower area of the tank. Both parts are filled with sand and water. In the right side of the tank, the water level stays constant during the experiment, but in the left side, the water level is falling over time. This experiment is modeled with SPH-method and finally compared the results with each other. The initial setting of the simulation is shown in der following outline (figure 5.11):

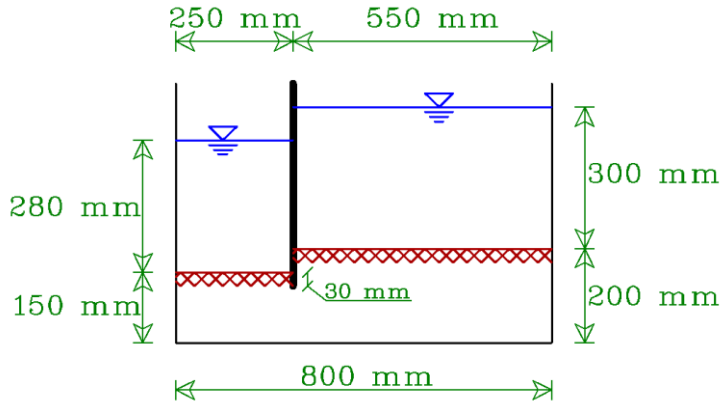

Figure 5.11: Initial setup of the numerical model of the problem "Hydraulic heave in non-cohesive soil"

Moreover, there is an opening with a height of 36 mm in the left side of the tank, which lies approximately 12 mm above the surface of the soil. This opening is responsible for the falling of the water level in the left side of the tank over time.

The initial applied parameters for modelling of the hydraulic heave experiment, that mentioned above is shown in the table 5.4:

Table 5.4: Initial setup parameters of the numerical simulation of the problem "Collapse of a water-saturated granular column into water"

initial height of the water in the right side of the tank $[m]$	0.50
initial height of the water in the left side of the tank $[m]$	0.43
initial height of the sand in the right side of the tank $[m]$	0.20
initial height of the sand in the left side of the tank $[m]$	0.15
height of the opening in the left side of the tank $[m]$	0.036
number of real soil particles	1041
number of real water particles	2624
number of neighboring soil particles	344

number of neighboring water particles	516
initial particle spacing for water and soil $[m]$	0.012
density of sand ρ_{soil} $[kg/m^3]$	2000
density of water ρ_{water} $[kg/m^3]$	1000
Young's Modulus of soil E $[MPa]$	15.0
internal friction angle of sand ϕ $[Degree]$	30.0
cohesion c $[kPa]$	0.0
dilatancy angle of soil $\psi[Degree]$	1.0
Poisson's ratio υ	0.30
permeability of soil k_s $[m/s]$	0.0024
porosity of soil n	0.35
time step dt $[s]$	0.00005
total time $[s]$	16.0
Processor (computing)	Intel® Core™ i7-6700T CPU @ 2.80GHz
Computing time [hour]	10,15

In the following figure 5.12, the experiment's results as well as the results of the numerical simulation are shown:

t=0.0 s

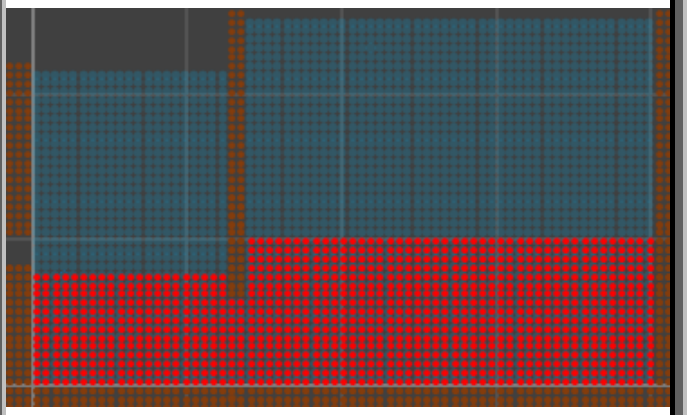

t=0.0 s

t=6.0 s

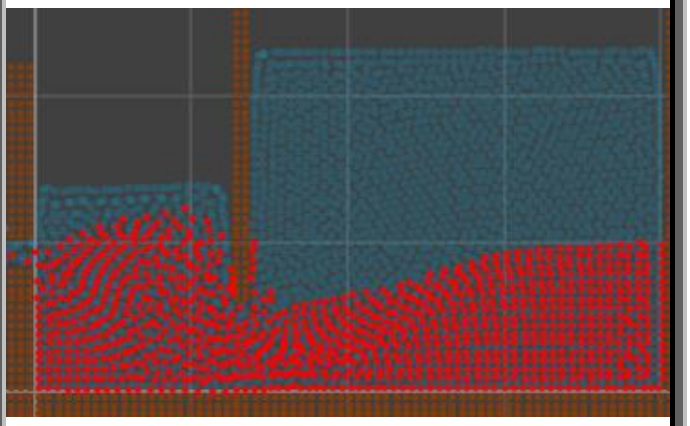

t=6.0 s

t=8.0 s

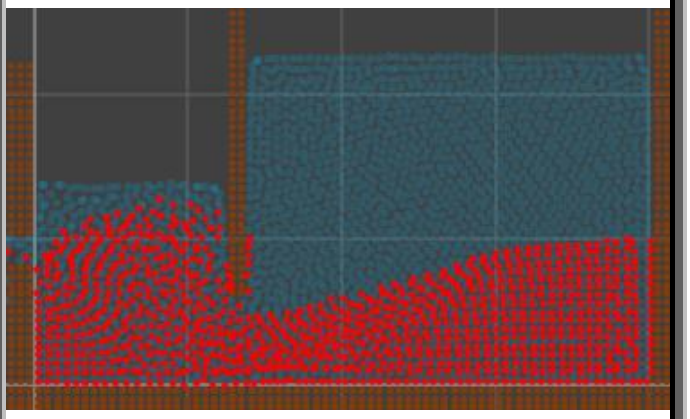

t=8.0 s

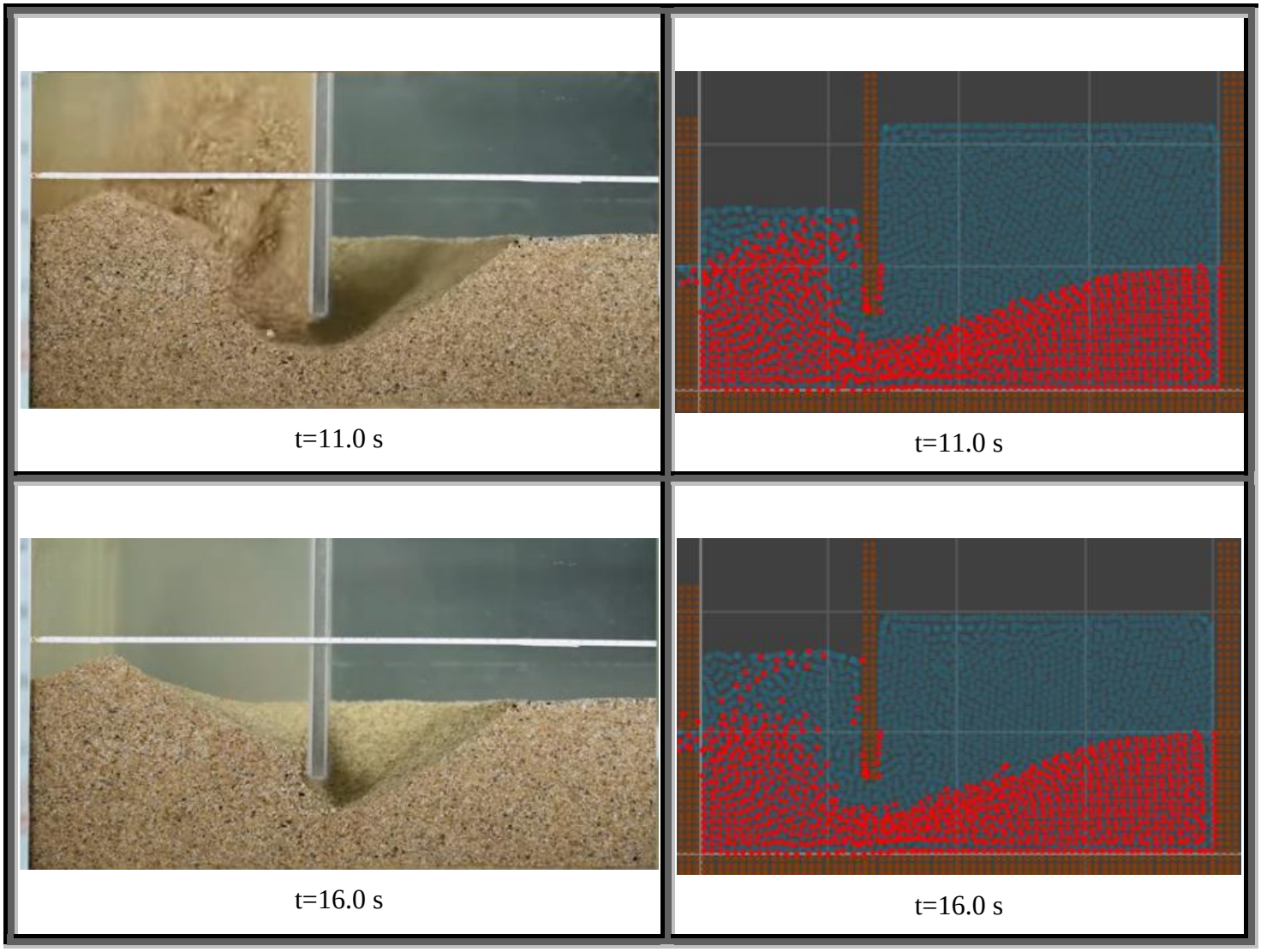

Figure 5.12: Compare between the experiment's results (reprint from (Aulbach & Ziegler, Versagensform und Nachweisformat beim hydraulischen Grundbruch –Plädoyer für den Terzaghi-Körper, 2014), (Copyright © 2014 Ernst & Sohn Verlag für Architektur und technische Wissenschaften GmbH & Co. KG, Berlin) and the animation of the experiment (Civil Engineering RWTH Aachen University_youtube, 2016)) and the results the numerical simulation of the problem "Hydraulic heave"

By comparing the results of the numerical simulation with SPH-method and the experiment's results can be stated that the numerical method has a very good agreement with experiment in the form and shape as well as with the representative time.

Because of the lack of the mesh in the numerical model, the particles are move freely in the domain and present the sand particles in the experiment very well. Furthermore, by observing the results can be realized that with this model a prediction of different situations of occurring hydraulic heave is well possible. Due to the results, the developed code is verified for modelling the interaction between water and soil in various situations and with different initial and boundary conditions. Moreover, the results show that, SPH-method is a reliable and robust numerical method for the simulation of saturated soil problems.

6 Applications of SPH-method in various engineering problems

In the last chapter, the developed Fortran-Code is validated for simulating soil and water as well as the interaction between soil and water. In this chapter, different problems with large deformation and various geometry and materials are simulated in order to show the ability of the SPH-method to model various geotechnic problems.

6.1 Failure process of Granular Material in a Silo

As explained in the previous chapter, the behavior of the granular materials is very important in many industrial processes and due to the complex behavior of these materials, it is an interesting topic for numerical methods (Bui H. , Fukagawa, Sako, & Wells, 2009). One of the interesting problems is the simulating discharge of a silo. Due to the very large deformation in the problem silo, this problem is a suitable task for SPH-method.

To model a silo with an opening for discharge, a box with two floors considered. The box has width of 300 cm and total height of 420 cm, which divide into two floors. The lower floor, which intended to collect the discharged material, has a height of 255 cm.

There is an opening with the width of 100 cm installed in the middle of the upper floor, which allows the granular material to fall down in the lower floor.

The initial soil height in the upper floor is planed 165 cm.

The initial setting and the dimensions of the numerical model is shown in der following outline (figure 6.1):

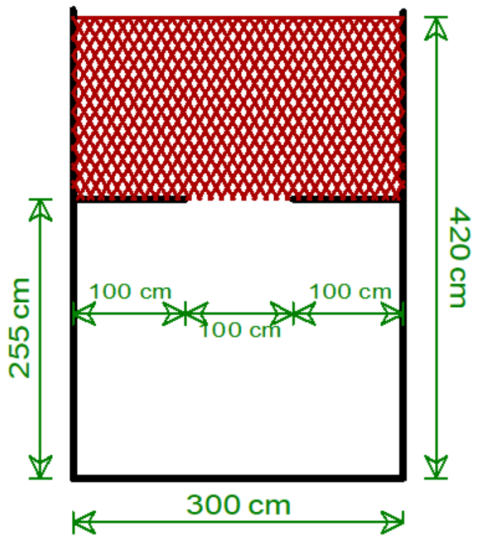

Figure 6.1: Initial setup of the numerical model of the problem "Failure process of Granular Material in a Silo"

In the following, the applied parameters for simulating the discharge of the silo are presented in the table 6.1:

Table 6.1: Initial setup parameters for the numerical simulation of the problem "Failure process of Granular Material in a Silo"

initial height of the sand in the upper floor of the silo $[m]$	1.65
height of the lower floor of the silo $[m]$	2.55
total height of the silo $[m]$	4.25
total width of the silo $[m]$	3.0

width of the opening of the silo $[m]$	1.0
number of real soil particles	12000
number of neighboring soil particles	2046
initial particle spacing $[m]$	0.02
density of sand ρ_{soil} $[kg/m^3]$	2000
Young's Modulus of soil E $[MPa]$	0.80
internal friction angle of soil ϕ $[Degree]$	30.0
cohesion $c[kPa]$	0.0
dilatancy angle of soil $\psi[Degree]$	1.0
Poisson's ratio υ	0.30
time step dt $[s]$	0.0005
total time $[s]$	20.0
Processor (computing)	Intel® Core™ i7-6700T CPU @ 2.80GHz
Computing time [hour]	11,0

In the figure 6.2, the results of the numerical simulation of this problem with SPH method is represented:

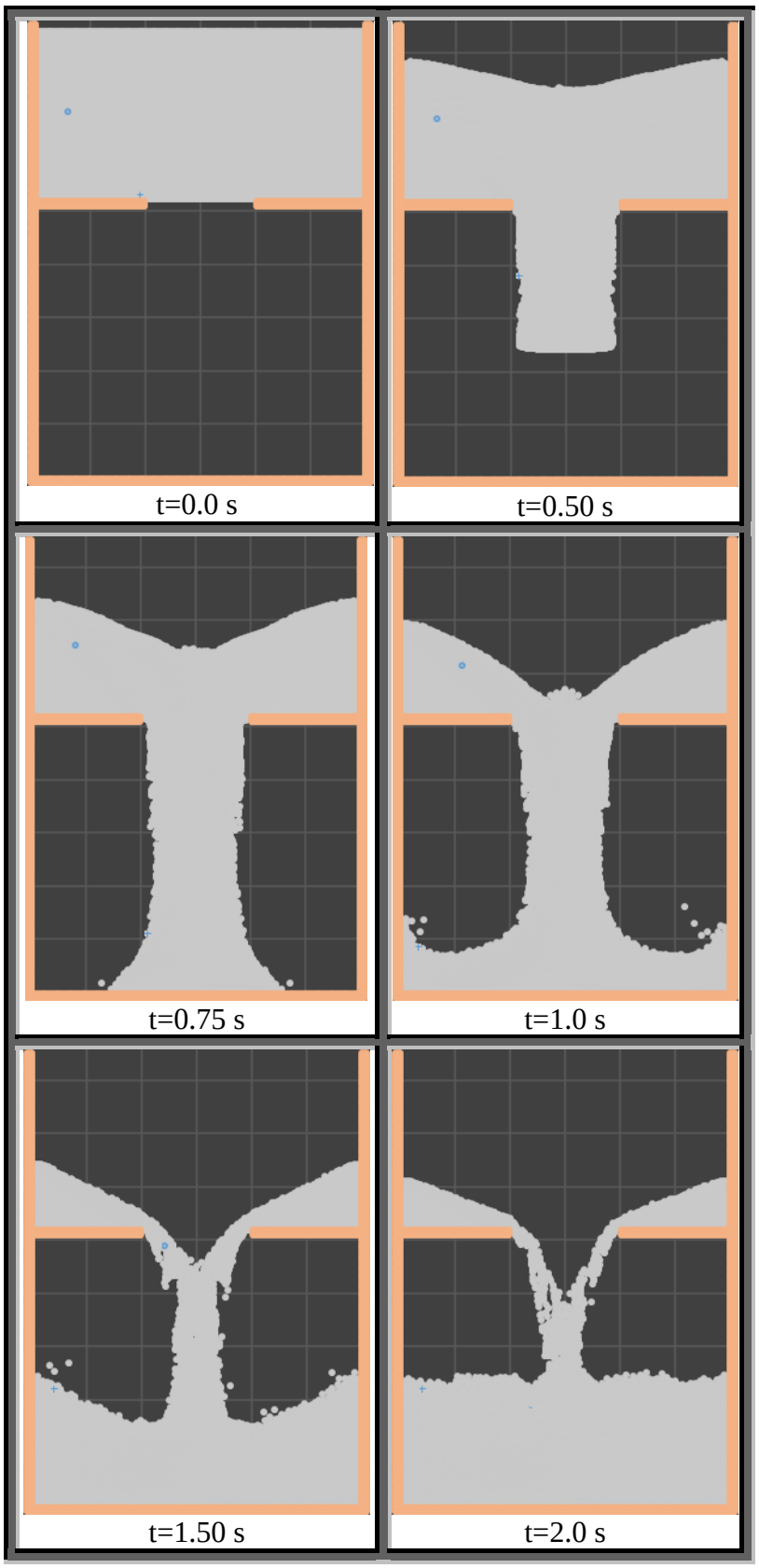
t=0.0 s
t=0.50 s
t=0.75 s
t=1.0 s
t=1.50 s
t=2.0 s

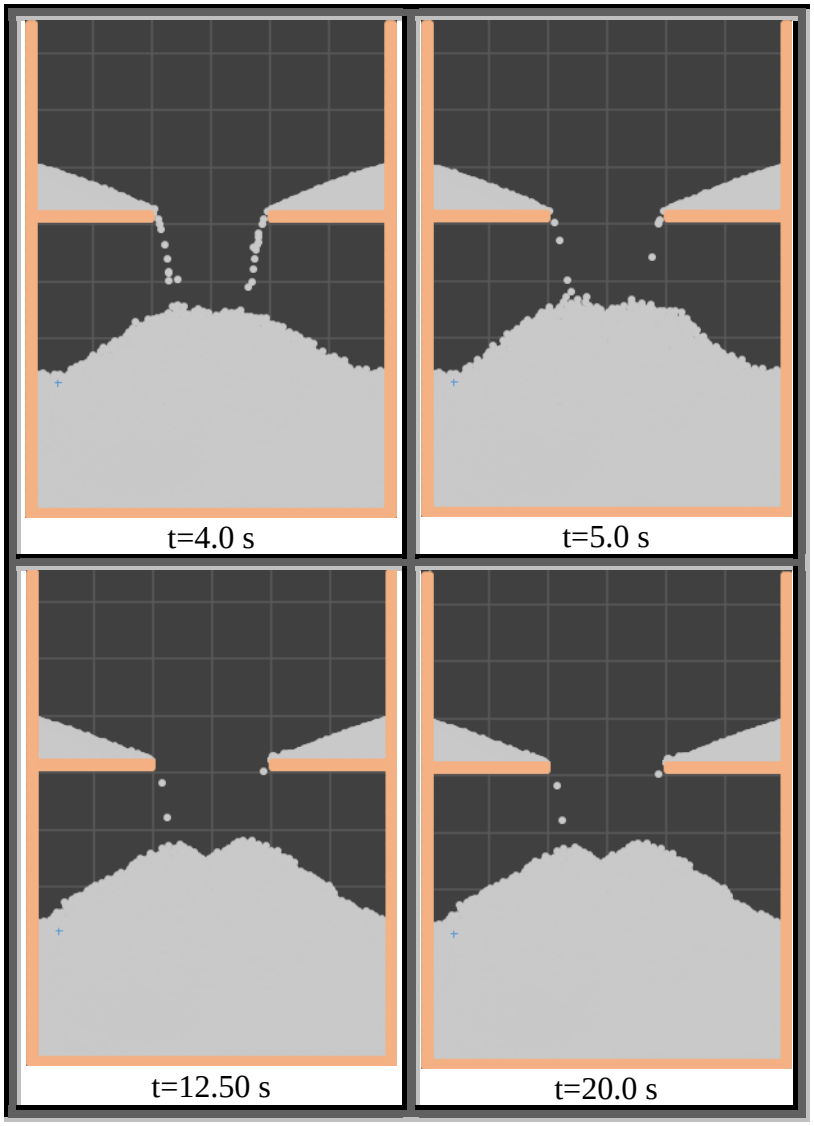

Figure 6.2: The results of the numerical simulation of the problem "Failure process of Granular Material in a Silo"

The results show that, the SPH method is a suitable method to simulate the granular materials, especially the problems with complex geometry and large deformations.

6.2 Excavation by a water jet

In continue to represent the ability of the Fortran-Code to simulate various problems, the numerical modelling of the problem “Excavation by a water jet” is considered. In this model, the water jet as a stream of water is projected into the soil. To simulate this problem, the excavation area is modelled as a box with a width of 120 cm, which is filled with 55 cm high dry sand. The water jet is also simulated with three layer of water particles with an initial velocity of 25 m/s.

The initial setting and the dimensions of the numerical model are shown in der following drawing (figure 6.3):

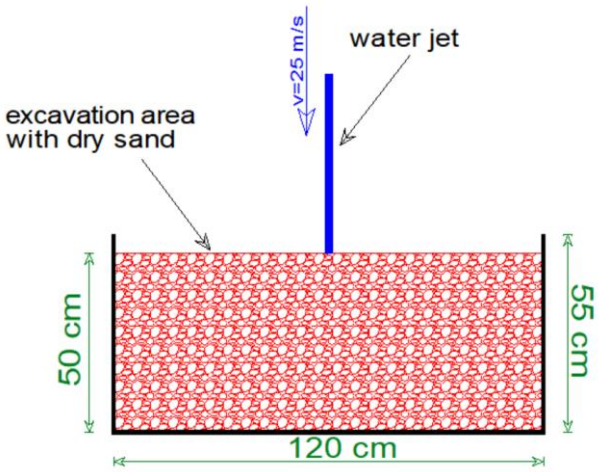

Figure 6.3: Initial setup of the numerical model of the problem “Excavation by a water jet”

Because of the high velocity of water jet, a soil with high modulus of elasticity of 150 MPa and a permeability of 1.0 mm/s is chosen, so that the erosion of the soil can be recognized clearly in the results.

The initial applied parameters for modelling of the problem “Excavation by a water jet” are shown in the table 6.2:

Table 6.2: Initial setup parameters for the numerical simulation of the problem "Excavation by a water jet"

initial width of the soil in the excavation area $[m]$	1,20
initial height of the soil in the excavation area $[m]$	0.50
initial width of the water jet $[m]$	0.02
initial velocity of the water jet $[m/s]$	25.0
number of real soil particles	6000
number of real water particles	750
number of neighboring soil particles	708
number of neighboring water particles	0
initial particle spacing for water and soil $[m]$	0.01
density of sand ρ_{soil} $[kg/m^3]$	2650
density of water ρ_{water} $[kg/m^3]$	1000
Young's Modulus of soil E $[MPa]$	150
internal friction angle of sand ϕ $[Degree]$	30.0
cohesion c $[kPa]$	0.0
dilatancy angle of soil $\psi[Degree]$	1.0
Poisson's ratio υ	0.30
permeability of soil k_s $[m/s]$	0.001
porosity of soil n	0.35
time step dt $[s]$	0.000002

total time $[s]$	0.08
Processor (computing)	Intel® Core™ i7-6700T CPU @ 2.80GHz
Computing time [hour]	3,0

In the following figure 6.4, the results of the simulation for the problem “Excavation by a water jet” are presented. As can be seen, the results show a good agreement with reality and look reasonable.

By impacting the water streams with high energy and velocity with the dry sand, the process of soil’s erosion has begun. Over the time the excavation continues and soil and water particles are thrown in the air.

The transmission of the water’s energy to sand particles can be observed very good from the results.

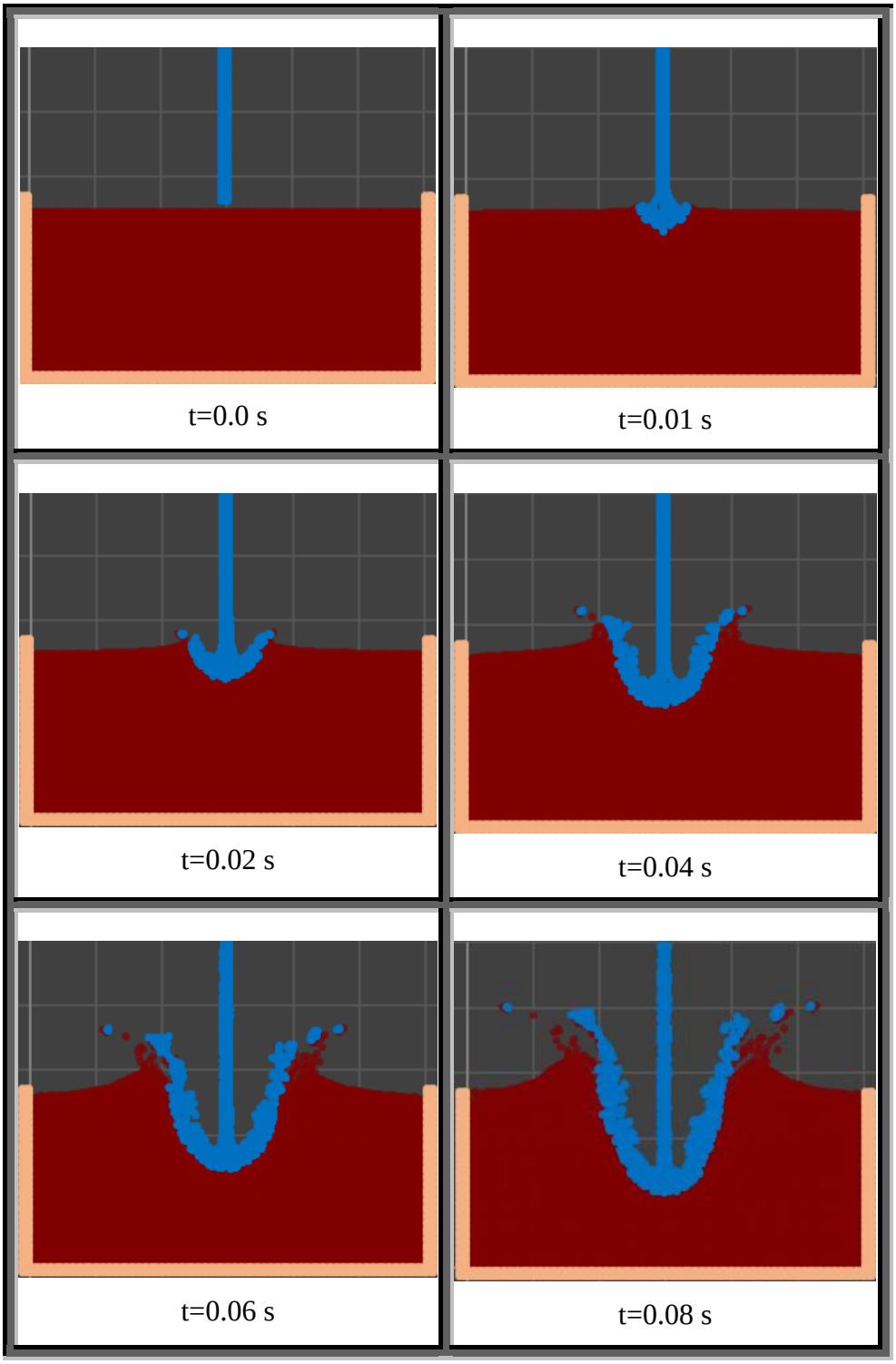

Figure 6.4: The results of the numerical simulation of the problem "Excavation by a water jet"

6.3 Two-sided slope embankment model

In this section of this research, the problem of the two-sided slope embankment is simulated. In this problem, a flood is assumed, that flows from upstream towards the embankment. The flood is created in this numerical model by setting an initial height difference between water level at the upstream of the embankment. At upstream are two water level intended. The lower water level at upstream has the same height as the crest level. The higher water level at upstream is 4.55 m higher than the crest at the beginning of the simulation. At downstream, the embankment has an initial low water level of 1.20 m. After running the model, the water with higher level collapse and form a wave of flood toward the embankment.

The Embankment supposed to be unsaturated at the beginning of the simulation. The water level in the embankment is created over the time between the water level in upstream and downstream by SPH formulations. The slope of the embankment is in the both side 1:2 (V:H) and build an angle of 26.57°. To observe the behavior of the embankment and carrying out the possibility test, two models with different permeability are simulated.

For implementing the boundary conditions, two types of fixed boundary particles are defined for water and soil separately. The fixed boundary particles are simulated with considering of the no-slip boundary condition for base and walls in the both side of the problem. It should be pointed out that the soil boundary particles are just applied in the base of the embankment. Because of the small amount of erosion in this model, no soil boundary particles are modeled for the walls. On the other hand, the water boundary particles are required in the base and the walls as well.

There is no extra external force applied to this model. The force of the gravity is the only applied external force in the momentum equation, apart from the interaction between water and soil by seepage force.

To reduce the total time of the simulation and thus decreasing the calculation cost of the simulation, in this model, soil is considered with high permeability.

The initial setting and the dimensions of the numerical model are shown in der following drawing (figure 6.5):

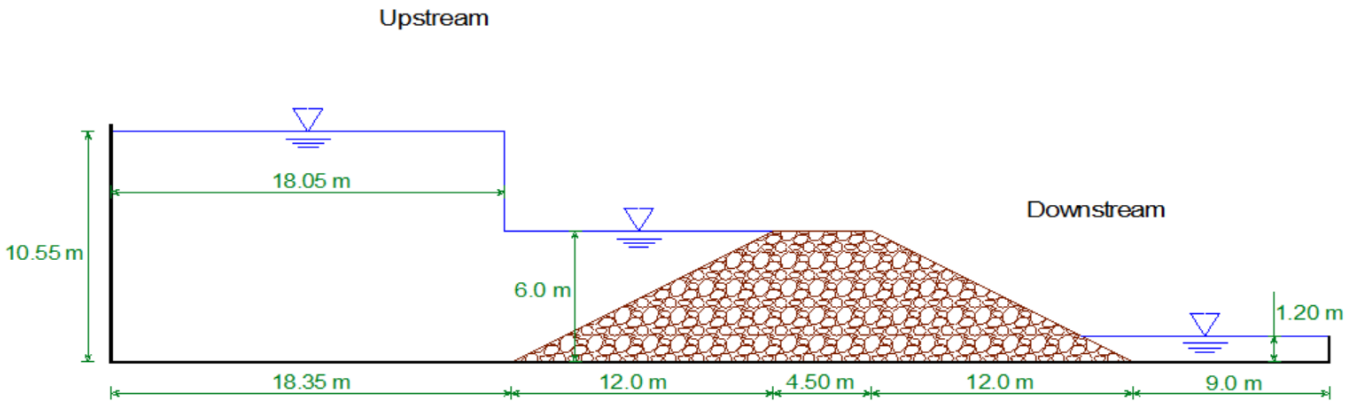

Figure 6.5: Initial setup of the numerical model of the problem "Two-sided slope embankment model"

The initial applied parameters for the simulation of the problem "Two-sided slope embankment model" are shown in the following table 6.3:

Table 6.3: Initial setup parameters for the numerical simulation of the problem "Two-sided slope embankment model"

initial higher level of the water in the upstream of the embankment $[m]$	10.55
initial lower level of the water in the upstream of the embankment $[m]$	6.0
initial water level in the downstream of the embankment $[m]$	1.20
initial height of the embankment $[m]$	6.0
Width of the embankment in base $[m]$	28.50
Width of the crest of the embankment$[m]$	4.50

number of real soil particles	1100
number of real water particles	2640
number of neighboring soil particles	375
number of neighboring water particles	693
initial particle spacing for water and soil $[m]$	0.30
density of sand ρ_{soil} $[kg/m^3]$	2700
density of water ρ_{water} $[kg/m^3]$	1000
Young's Modulus of soil E $[MPa]$	50.0
internal friction angle of sand ϕ $[Degree]$	30.0
cohesion c $[kPa]$	0.0
dilatancy angle of soil $\psi[Degree]$	1.0
Poisson's ratio υ	0.30
permeability of soil k_s $[m/s]$ in Test 1	0.02
permeability of soil k_s $[m/s]$ in Test 2	0.05
porosity of soil n	0.30
time step dt $[s]$	0.0002
total time $[s]$	120
Processor (computing)	Intel® Core™ i7-6700T CPU @ 2.80GHz
Computing time [hour]	19,50

In the figure 6.6, the results of the numerical simulation for the problem two-sided slope embankment model are presented. The results are shown for two model with the same geometry and various permeability.

permeability of soil K_S=0.02 m/s	**permeability of soil K_S=0.05 m/s**
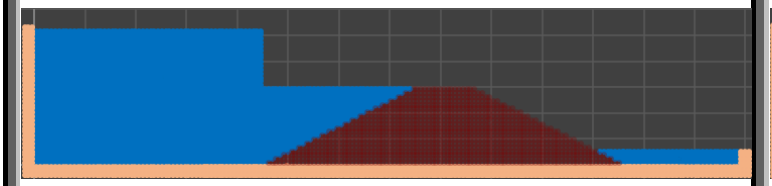 t=0.0 s	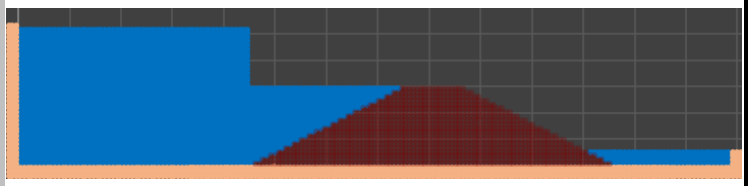 t=0.0 s
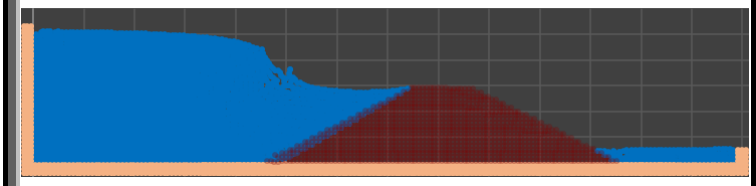 t=0.60 s	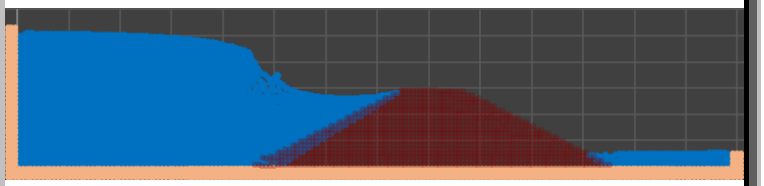 t=0.60 s
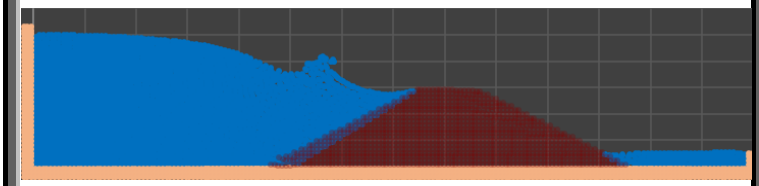 t=1.0 s	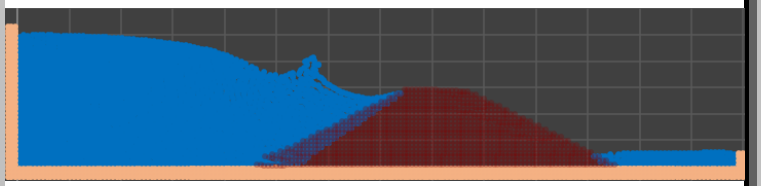 t=1.0 s
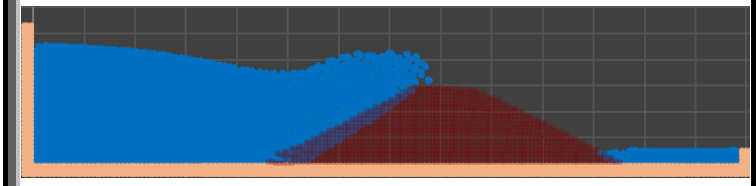 t=2.0 s	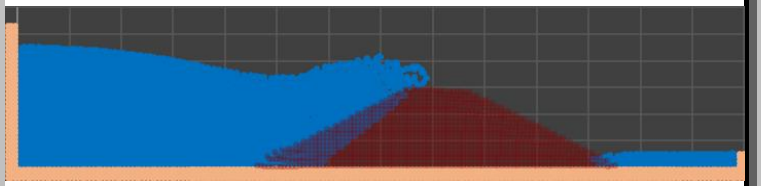 t=2.0 s

permeability of soil K_S =0.02 m/s	**permeability of soil K_S =0.05 m/s**
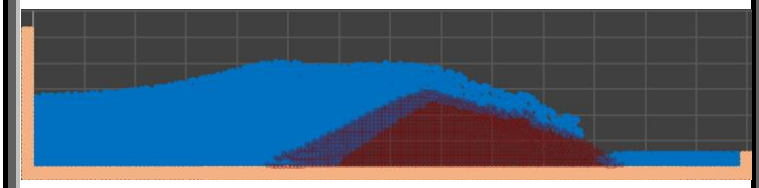 t=5.0 s	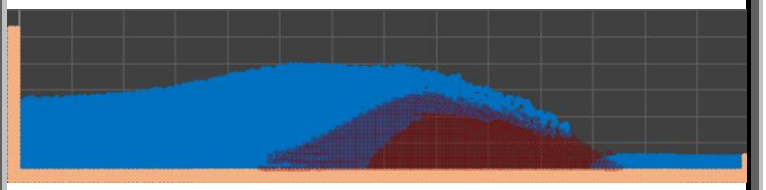 t=5.0 s
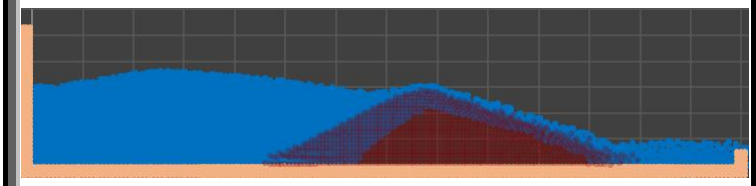 t=10.0 s	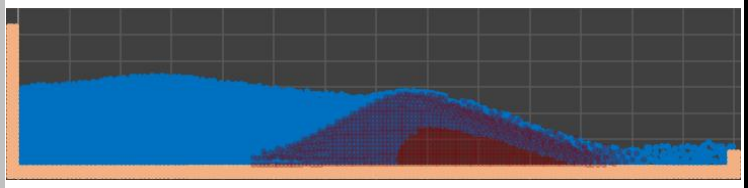 t=10.0 s
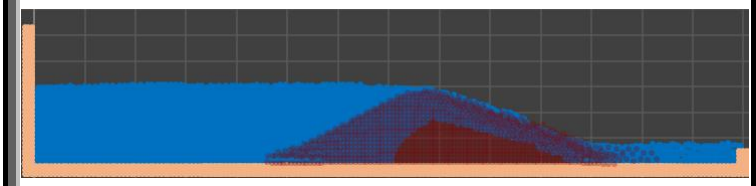 t=20.0 s	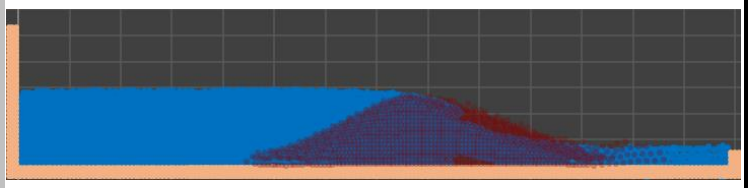 t=20.0 s
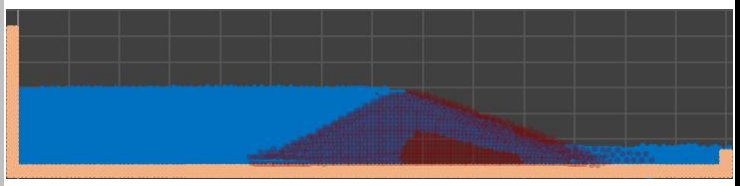 t=30.0 s	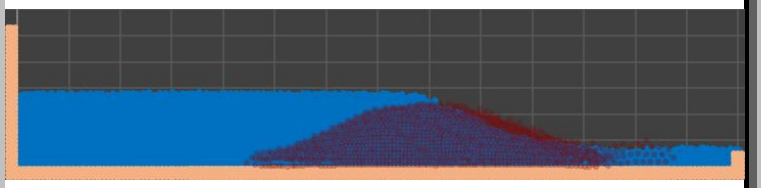 t=30.0 s
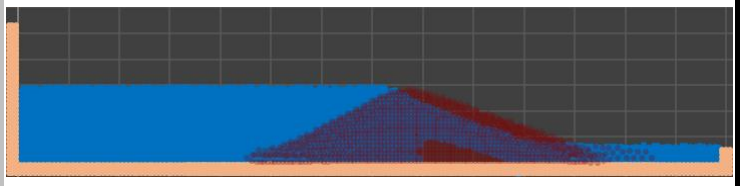 t=40.0 s	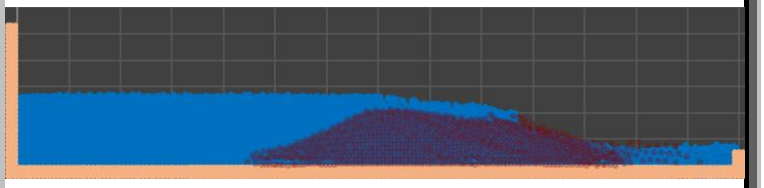 t=40.0 s

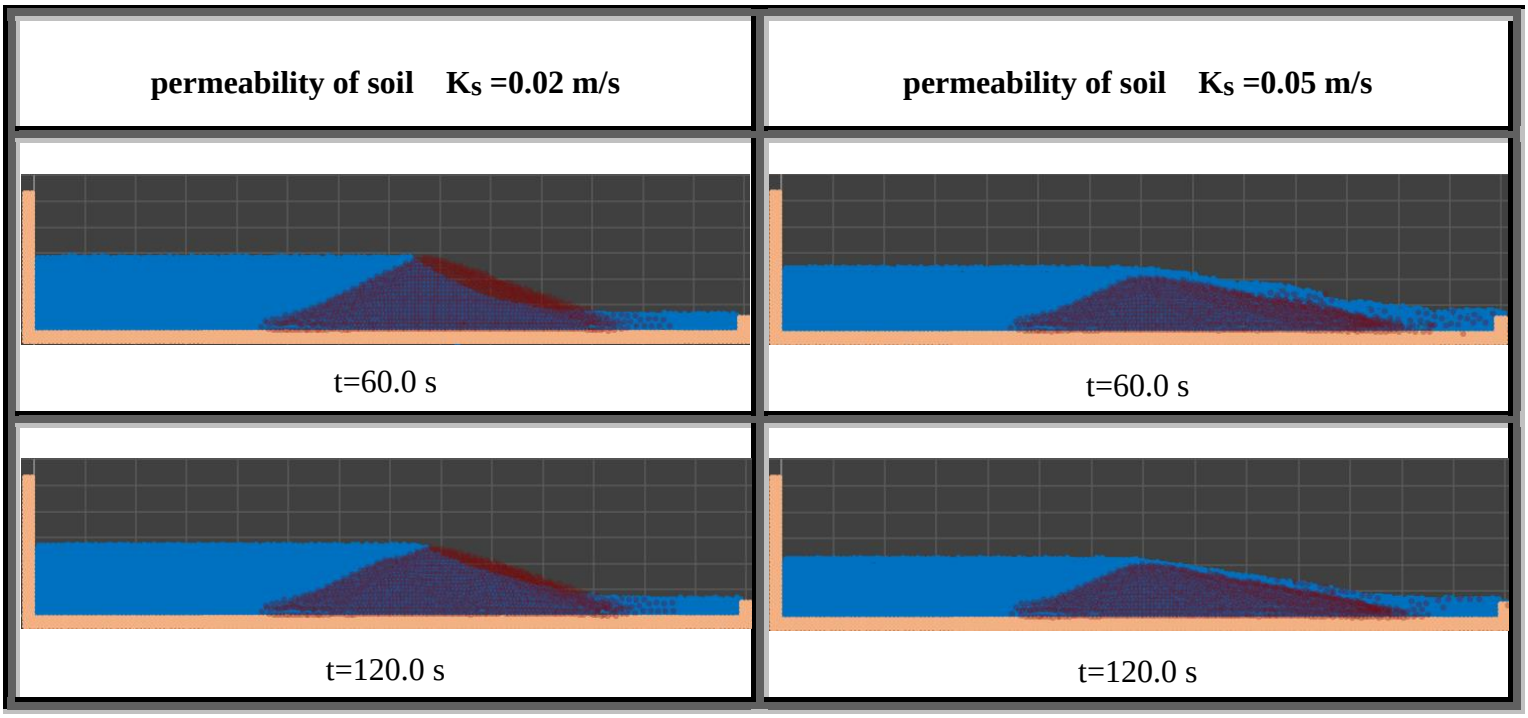

Figure 6.6: Compare between the results of the numerical simulation of the problem "Two-sided slope embankment model" with two different permeability

From the results can clearly recognized that the water goes faster through the embankment with higher permeability. It is in accordance with the known knowledge from geotechnic.

By start to run the simulation, the water with higher level at upstream collapse and form a wave of flood toward the embankment. The wave is higher than the crest of the embankment and therefore water flows over the crest. Over the time, the embankment is flooded. Gradually is the crest damaged and some soil particles are removed by the wave of water. The erosion of the embankment is especially in the test 2 with higher permeability more identifiable. The mixture of soil and water particles at the downstream can be obviously observed.

The progression of the water into embankment by seepage force and forming the pore water in embankment is corresponding to the physics law. The presented results are reasonable and acceptable and again show clearly the ability of SPH-method to handle with such geotechnical problem.

7 Defect in the diaphragm wall in Cologne

On 3rd of March 2009, the historical archive building of the city Cologne collapsed. According to the court-expert, it happened because of the mistake in subway construction. In the construction of the diaphragm wall, a big block is forgotten to remove before filling the wall with concrete. This leads to leakage in the diaphragm wall, which was located in the underground with high water table. The duty of the diaphragm wall was to prevent the water from entering in the excavation pit. Due to the resulting leak, the ground water found a way to the excavation pit. Over the time, the opening in the wall is enlarged. By the weight of the upper layer of soil, a great amount of water, sand, gravel, etc. is rushed into the pit, thereby the soil under the archive building is undermined and the building collapse (https://www.dw.com, 2019).

In order to investigate this accident in Cologne in more details, a small-scaled experiment is carried out in the Institute of Geo-Engineering in the Clausthal University of Technology in Germany. The considered geometry and applied parameters in the experiment are chosen in accordance with the diaphragm wall in Cologne and with considering a scale factor of 1:7 (Mattner, 2018) (Emker, 2020).

In the experiment, it has tried to model a diaphragm wall with an opening as a defect in the construction. For this experiment, a tank is utilized with the dimensions of 200 x 100 x 15 cm for length, height and depth. To build the diaphragm wall two

wall-elements are used, which are installed above and below the opening to form a defect in the wall's construction.

The both sides of the wall-elements are filled with soil with different height level. At the beginning of the experiment, the soil is dry. To model the effect of the ground water, a water tank is installed above the experiment's tank. Water flows from water tank with 9 thin water pipes to the left side of the experiment's tank. Therefore, soil is saturated and the pore water pressure increases in the model, which is necessary to cause the collapse in the model.

As required measuring technology, six pore water pressure sensors are installed in the experiment's tank in order to measure the pore water pressure in whole experiment's time. The results of these sensors are very important for the numerical simulation. To simulate the similar pore water pressure in the simulation, the results of the pressure measurement as initial and boundary conditions utilized.

To simulate the boundary conditions, the base and outer walls as well as the wall-elements in the experiment, no-slip boundary condition is considered for both soil and water boundary particles.

The geometry and initial conditions of the numerical simulation are chosen similar to the experiment and they are shown in the following figures 7.1 and 7.2:

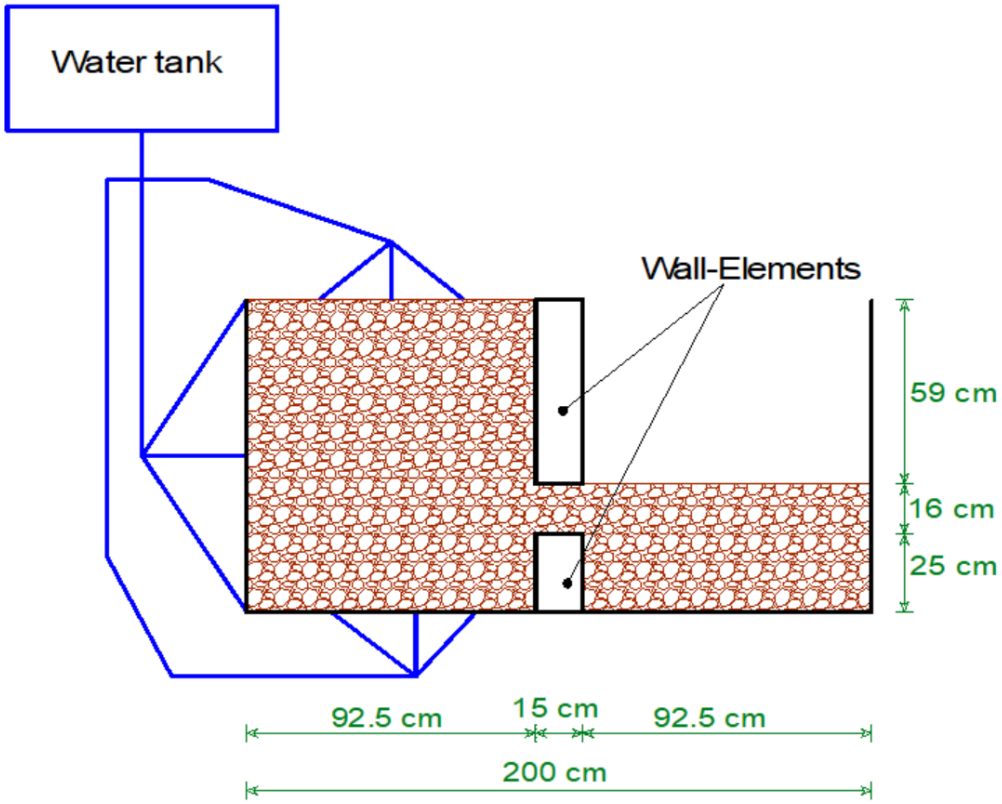

Figure 7.1: Initial setup of the experiment model of the problem "Defect in diaphragm wall in Cologne"

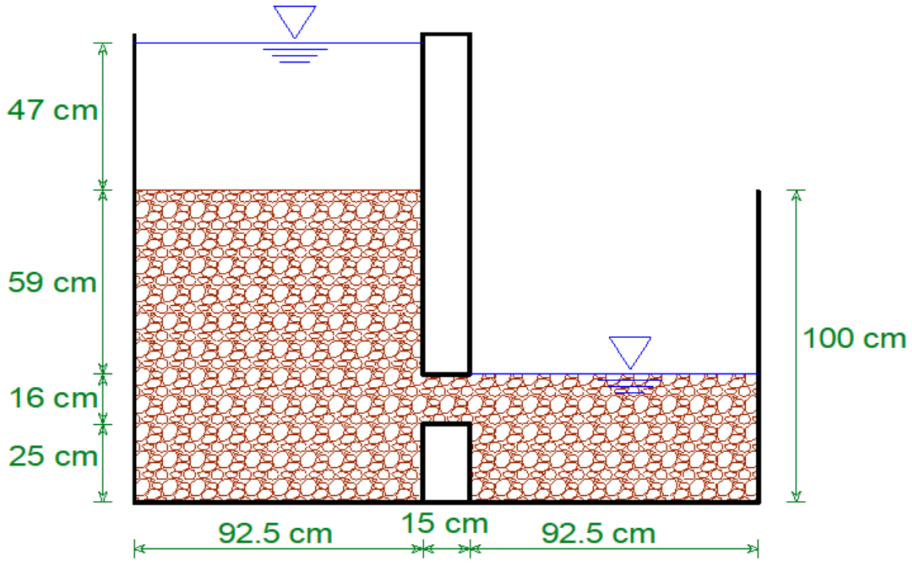

Figure 7.2: Initial setup of the numerical model of the problem "Defect in diaphragm wall in Cologne"

As can be seen in the last figure, the effect of the water tank is considered as higher initial water level in the simulation. To choose the correct initial water level, the results of the measurement of the pore water pressure is used. As in the figure 7.3 illustrated, the whole experiment's time can be divided into three regions. The Region I is the required time to fill the link side of the experiment's tank with water. This part is not relevant with the simulation's model. The simulation begins with the illustrated initial water level, that produces the same pressure as the water tank. Region III is optional to add in the simulation, as the form of soil will not change more. Because of the high calculation time, this part is not simulated in this simulation. After saturating the soil in the Region I, the pore water pressure stays almost constant in Region II. In this time span, the transfer of water and soil through the opening begins and failure of the soil surface in the left side of the experiment's tank occurred.

In the following graphic (figure 7.3), the results of the pore water measurement of a sensor in the axis of the opening is shown:

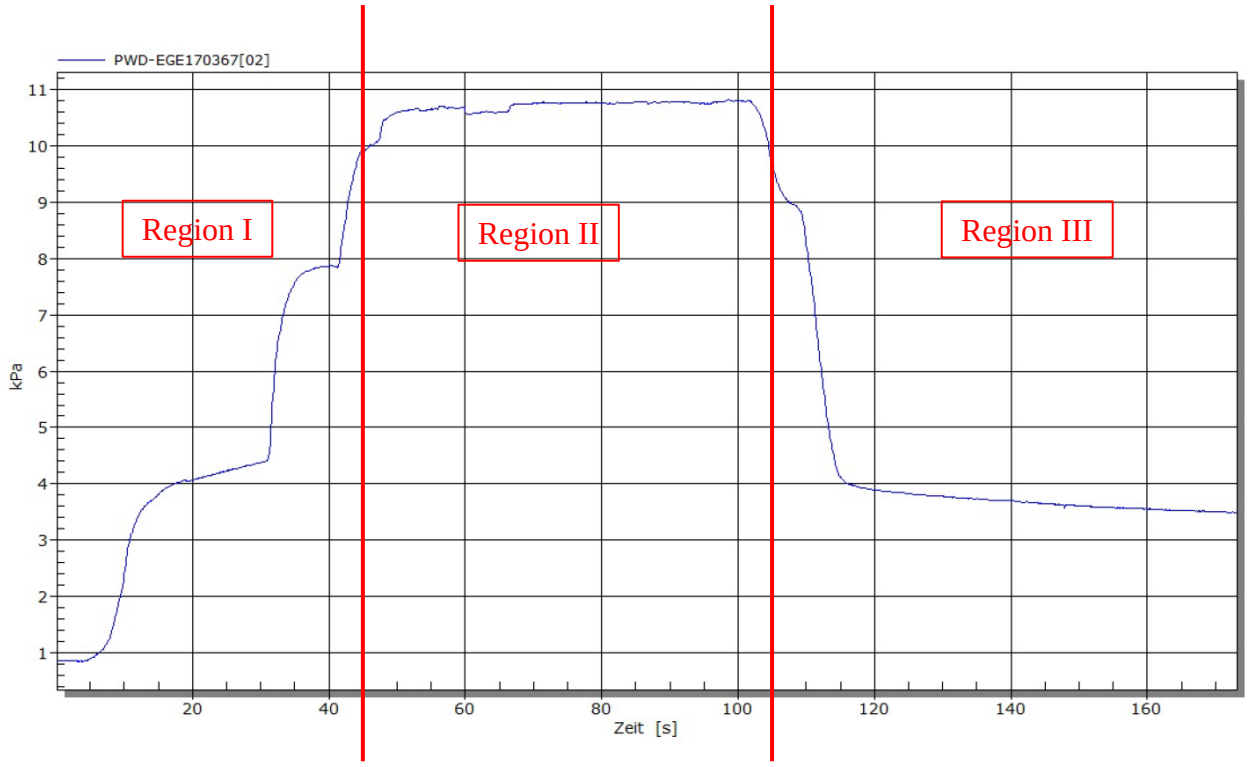

Figure 7.3: Results of the pore water pressure measurement of a sensor in the axis of the opening (reprint from (Mattner, 2018))

In order to simulate the water level nearly constant in the time span of the Region II, an algorithm is developed, which produce new water particles regularly in the left side of the model. This is in accordance with the water that flows from the water tank into the left side of the experiment tank.

The initial applied parameters for the simulation of the problem "Defect in the diaphragm wall in Cologne" are presented in the table 7.1:

Table 7.1: Initial setup parameters for the numerical simulation of the problem "Defect in diaphragm wall in Cologne"

initial water level in the left side of the experiment' tank $[m]$	1.47
initial soil level in the left side of the experiment' tank $[m]$	1.0
initial water level in the right side of the experiment' tank $[m]$	0.41
initial soil level in the right side of the experiment' tank $[m]$	0.41
number of real soil particles	1325
initial number of real water particles	1731
total number of real water particle	2108
number of neighboring soil particles	522
number of neighboring water particles	644
initial particle spacing for water and soil $[m]$	0.032
density of sand ρ_{soil} $[kg/m^3]$	2100
density of water ρ_{water} $[kg/m^3]$	1000
Young's Modulus of soil E $[MPa]$	150
internal friction angle of sand ϕ $[Degree]$	30.0

cohesion c $[kPa]$	0.0
dilatancy angle of soil $\psi[Degree]$	0.60
Poisson's ratio υ	0.30
permeability of soil k_s $[m/s]$	0.00088
porosity of soil n	0.30
time step dt $[s]$	0.0001
total time $[s]$	65
Processor (computing)	Intel® Core™ i7-6700T CPU @ 2.80GHz
Computing time [hour]	20,0

In the following figure 7.4, the results of the simulation of the defect in the diaphragm wall are illustrated:

t=45.0 s

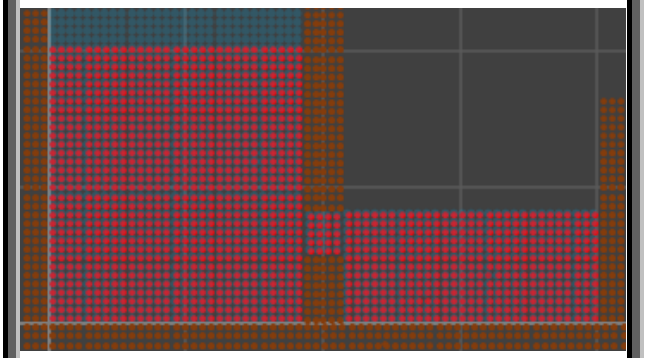

t=0.0 s

t=60.0 s

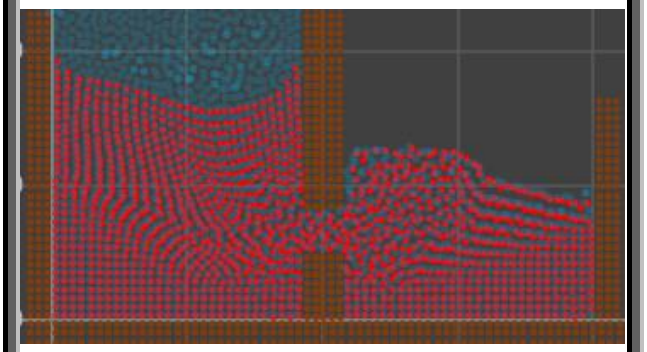

t=15.0 s

t=75.0 s

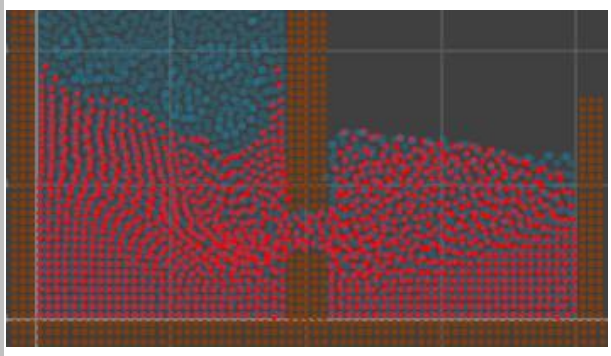

t=30.0 s

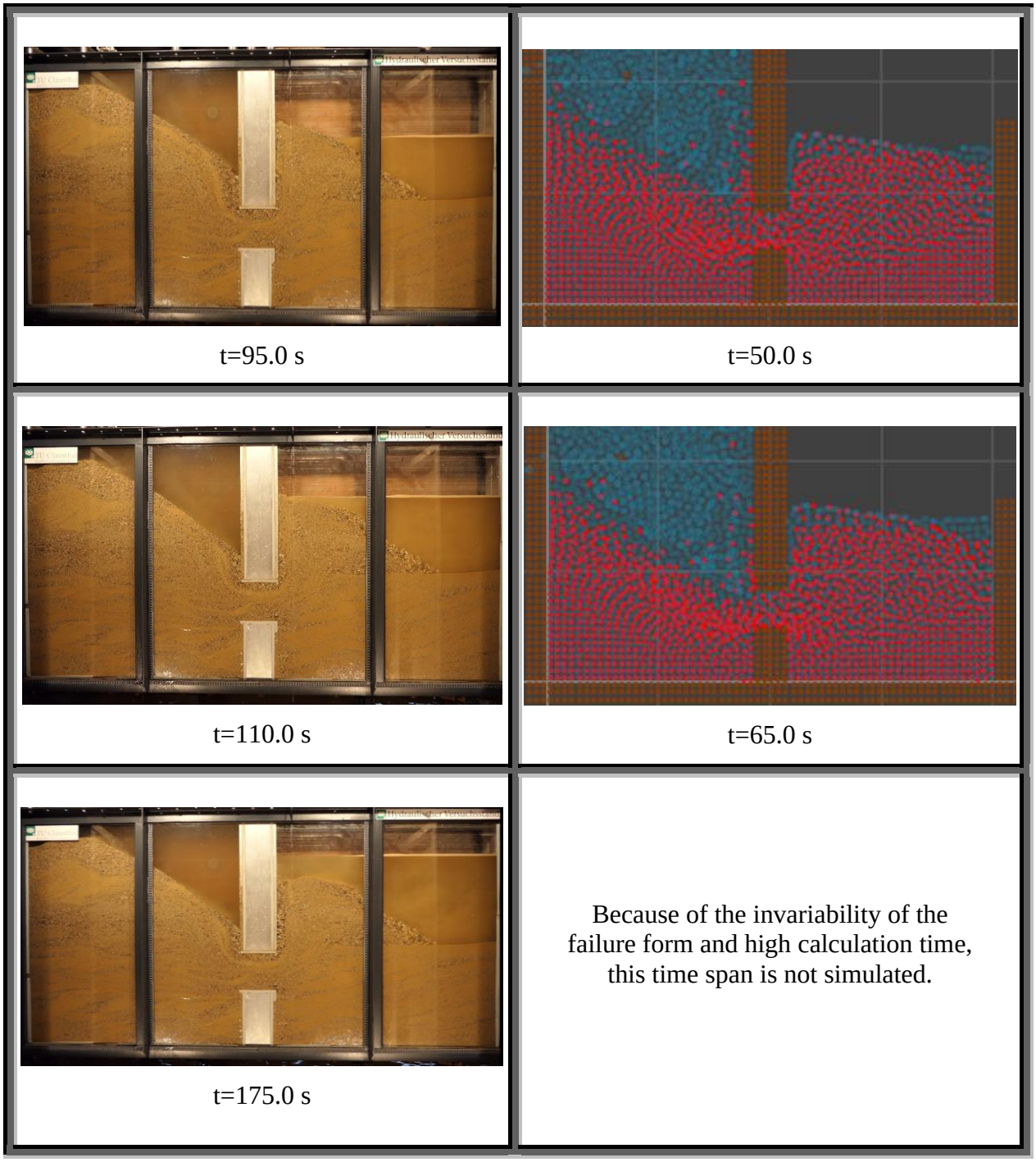

Figure 7.4: Compare between the experiment's results (reprint from (Mattner, 2018)) and the results of the numerical simulation of the problem "Defect in diaphragm wall"

After filling the left side of the experiment tank, the water level is sufficient to build a failure. Thus, the seepage force tried to find a way to go through the opening. Slowly, the movement of water and soil through the opening begins and occur the failure in the surface of the soil in the left side of the experiment's tank. Simultaneously, in the right side of the experiment tank forms a heaped pile of soil. By reaching equilibrium between forces in the left and right side of the experiment, the final form of the failure is achieved (t = 110 s in experiment). Afterwards, the final form of the soil stays unchanged but the water level increases. By specific observing the experiment, it can be seen that, there are some leakages in the experiment's tank, that leads water from left side to the right side and causes the increasing of the water level at the end of the experiment. In the figure 7.5 the main leakage is shown.

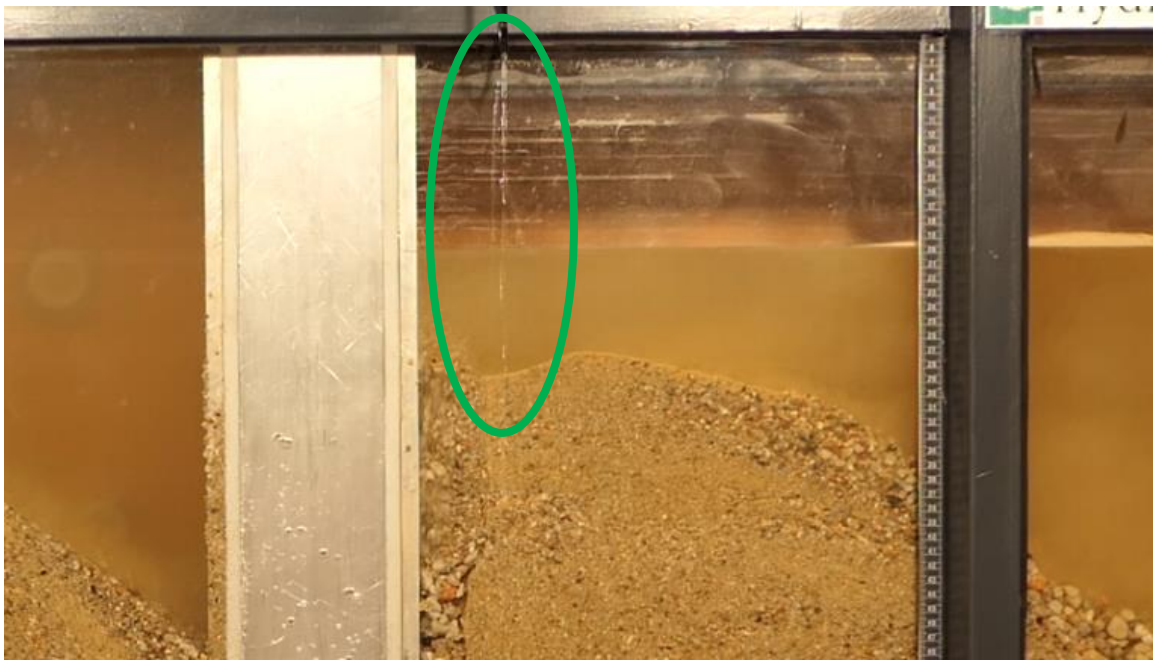

Figure 7.5: The existing leakage in the experiment

By observing and comparing the results from the experiment and numerical simulation, a nearly good agreement between the both results can be recognized. At the beginning of the simulation, some little difference in shape and form of the results are available, but over the time the difference is smaller and the final shape of the failure as well as the form

of the generated heaped pile of soil in the numerical simulation are in a good agreement with the experiment. Moreover, it can be seen that the water level is also approximately the same in the right side of the experiment and simulation. Furthermore, these results validate the ability and accuracy of the developed code.

In order to remove the problems as leakage in the above-mentioned experiment, a new series of experiments are carried out later in the Institute of Geo-Engineering in the Clausthal University of Technology. These new experiments are based on and in continue to the prior work. The new experiments are considered with the following modifications (Emker, 2020):

1. To model the real stresses in the area of the defect in the cologne Diaphragm wall, compressed air cushions are used in the experiment box. The resultant stresses are determined by means of earth pressure sensors. The positions of these sensors are shown in the following drawing:

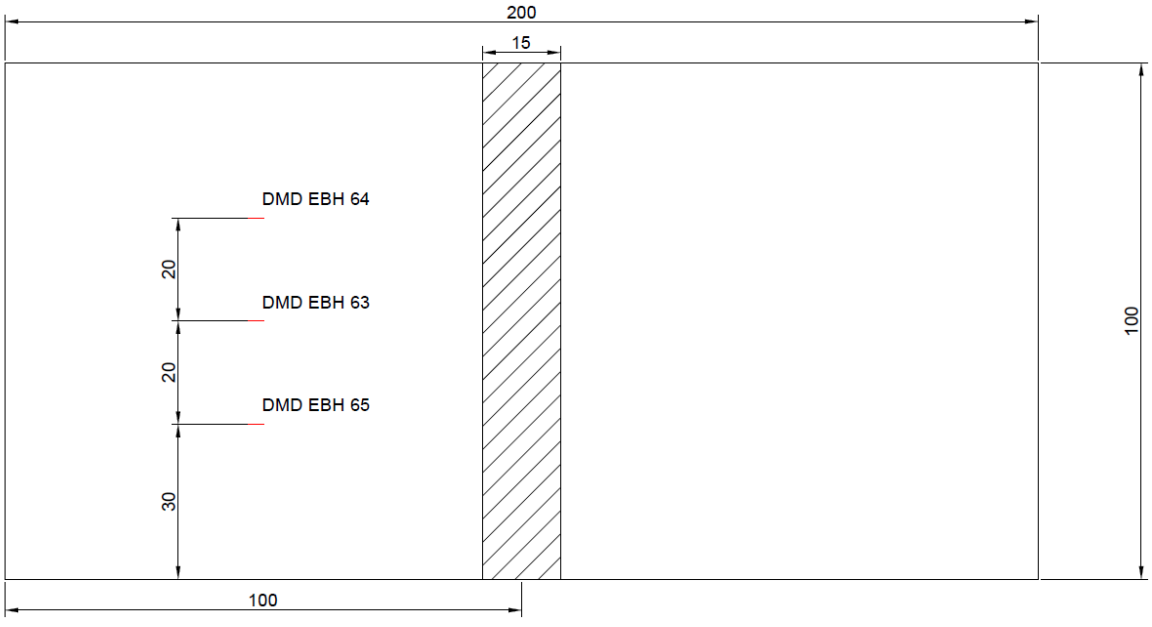

Figure 7.6: Positions of the earth pressure sensors in cm (reprint from (Emker, 2020))

2. The lower element in the middle wall-element is removed. In the following drawing (figure 7.7), the dimensions of the used element are illustrated:

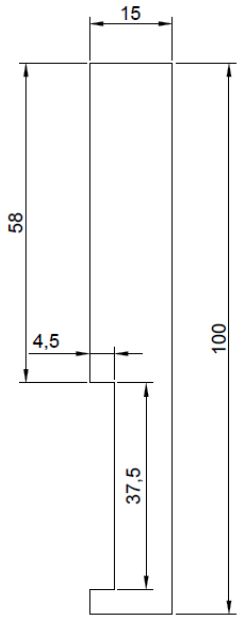

Figure 7.7: The dimensions of the middle wall-element in cm (reprint from (Emker, 2020))

3. According to the pore water pressure measurement in the new experiment the value of water pressure is more than the prior experiments in 2018. In the following diagram, the locations of the installed pore water pressure sensors are shown:

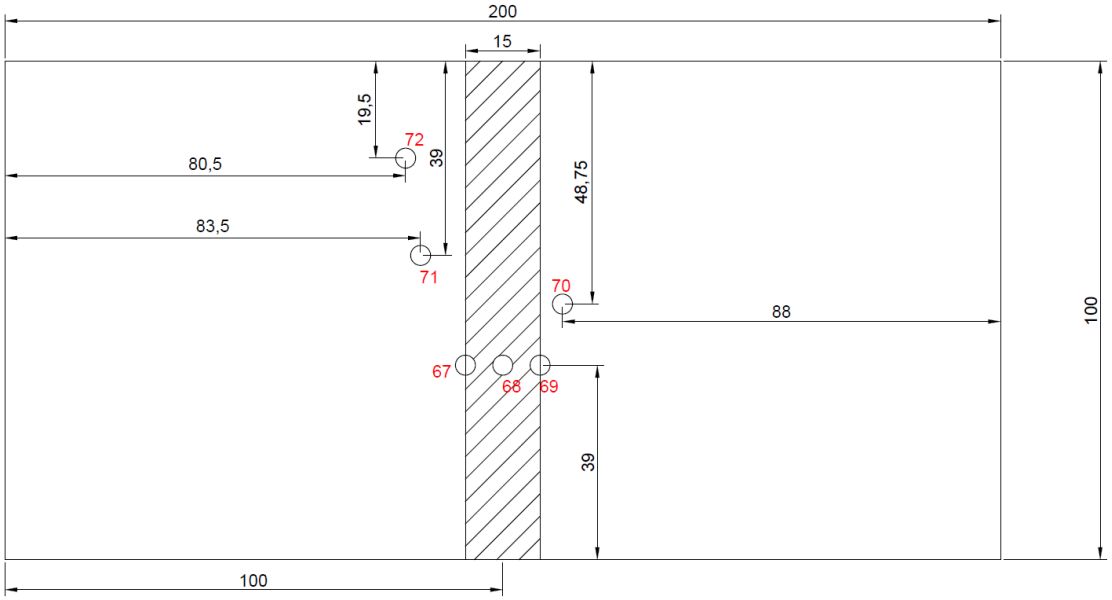

Figure 7.8: Positions of the pore water pressure sensors (reprint from (Emker, 2020))

Moreover, the results of the measurements of the stress and pore water pressure are shown in the diagram below (figure 7.9) for the experiment number 9.

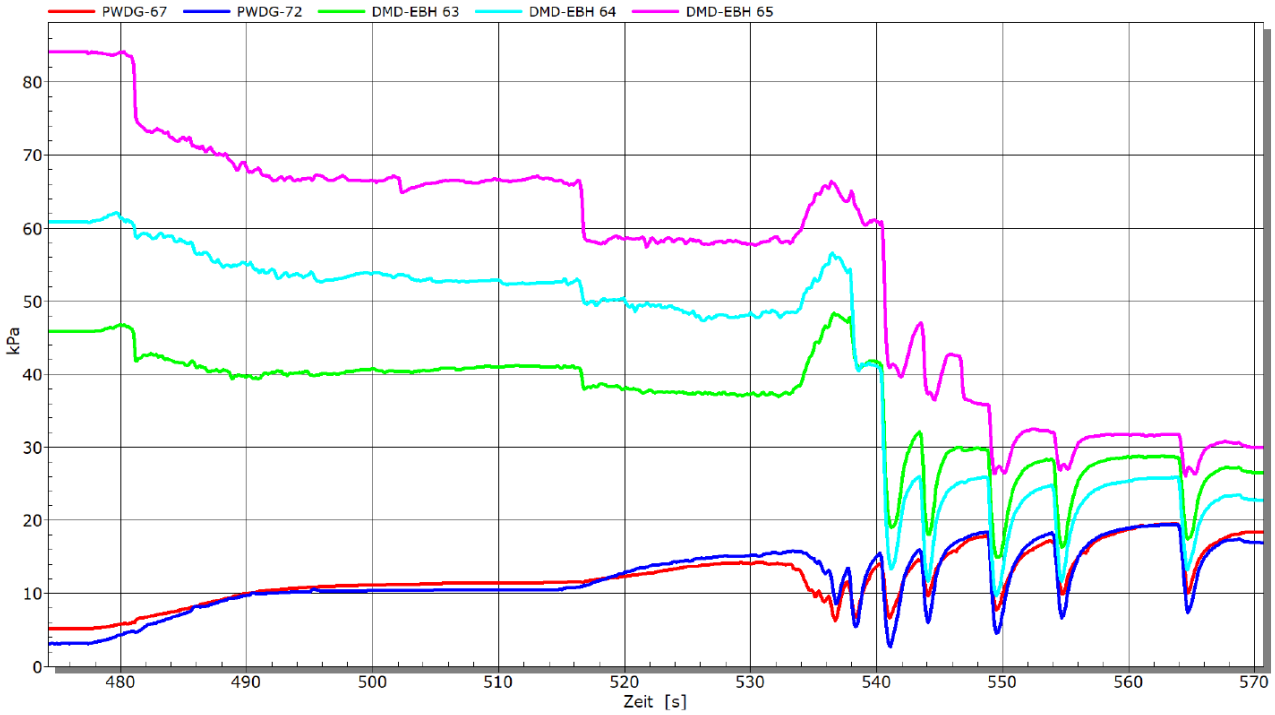

Figure 7.9: Results of the measurements in time of collapse (reprint from (Emker, 2020))

To simulate the new experiment-series, the experiment 9 is chosen. According to the results of the experiment, the failure occurred at 541 s. The effect of the failure can be easily seen by the fluctuation of the pore water measurement after 541 s. According to the measured pore water pressure of approximately 14 kPa at the sensor PWDG-67 at this time, a water column of 1,40 m above the position of this sensor is considered in the simulation as the initial water level in the left side of the experiment's box.

As above mentioned, compressed air cushions are used to increase the stress of the soil in the experiment. According to the above diagram, the stress of the soil at the sensor DMD EBH 65 shortly before the failure is 62 kPa. Therefore, the initial stress of the soil in the left side of the experiment's box is considered in accordance with this value in the simulation.

The initial applied parameters for the simulation of the problem "Defect in the diaphragm wall in Cologne" according to the new experiment are presented in the table 7.2:

Table 7.2: Initial setup parameters for the numerical simulation of the problem "Defect in diaphragm wall in Cologne" in accordance with the new experiments

initial water level in the left side of the experiment' tank $[m]$	1.80
initial soil level in the left side of the experiment' tank $[m]$	1.0
initial water level in the right side of the experiment' tank $[m]$	0.50
initial soil level in the right side of the experiment' tank $[m]$	0.46
number of real soil particles	1399
initial number of real water particles	2182
number of neighboring soil particles	482
number of neighboring water particles	684
initial particle spacing for water and soil $[m]$	0.032
density of sand ρ_{soil} $[kg/m^3]$	2100
density of water ρ_{water} $[kg/m^3]$	1000
Young's Modulus of soil E $[MPa]$	150
internal friction angle of sand ϕ $[Degree]$	30.0
cohesion c $[kPa]$	0.0
dilatancy angle of soil $\psi[Degree]$	0.60
Poisson's ratio υ	0.30
permeability of soil k_s $[m/s]$	0.0014
porosity of soil n	0.30
time step dt $[s]$	0.0001

Processor (computing)	Intel® Core™ i7-6700T CPU @ 2.80GHz
Computing time [hour]	0,35

In the figure 7.10, the results of the simulation of the defect in the diaphragm wall in accordance with the new carried-out experiment (Emker, 2020) are illustrated:

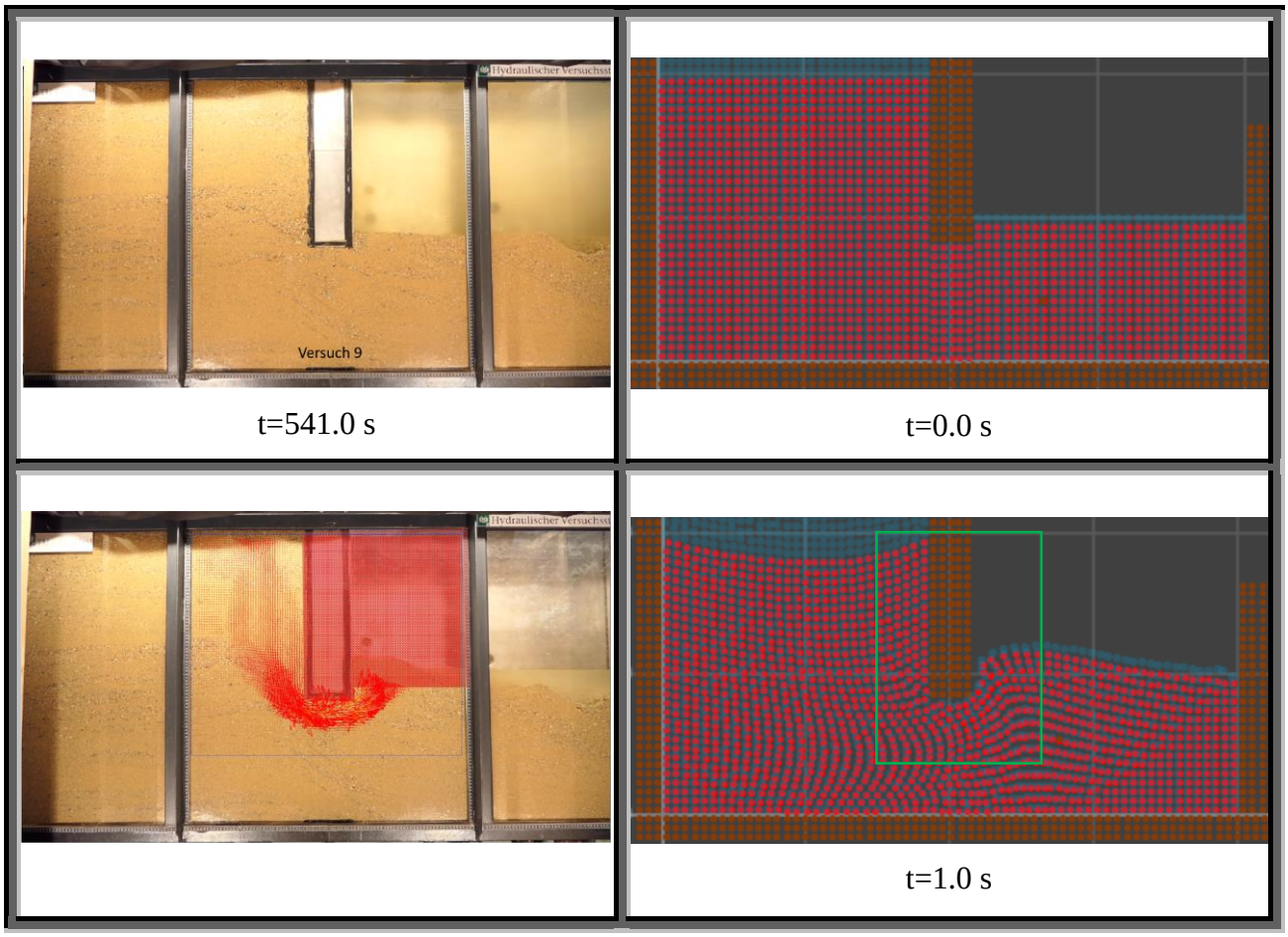

Figure 7.10: Compare between the experiment's results (reprint from (Emker, 2020)) and the results of the numerical simulation

By observing the result of the simulation and comparing it with the experiment's results, it can be clearly seen, that the form and size of the failure is very similar with the experiment. The analysis of the experiment with the PIV-method (Particle Image Velocimetry) is as well in a good agreement with the movement of the particles in the simulation.

As conclusion, it can be pointed out that the results of the numerical simulation with the SPH-method show the high ability of this method for applying to predict the behavior of the similar problems in the future.

8 Conclusions and summary

By rapidly developing the big cities nowadays, it is required further on to use the underground space immensely in order to construct various Infrastructure, skyscraper, transport systems, subterranean parking lots, etc. For Building such constructions, it is required to utilize the underground space up to 100 m. For Constructing such depths, retaining system of the excavation pit is one of the most important parts of the planning and execution of the project. Retaining systems are the main element to retain against soil and groundwater pressure in the excavation pit.

For projects with various retaining requirements, various types of retaining systems are applied. One of the prevalent retaining systems is constructing diaphragm walls, which offer many advantages and they are suitable for using almost all different soil types. Diaphragm walls also meet all requirements for the construction of a deep foundation pit as waterproofness, earth retention and load bearing foundation. Despite the remarkable advantage of diaphragm walls, many collapse are reported in the last years as the collapse of the Cologne Archive and the accident at the underground metro line U2 in Berlin. The reason of such collapses are mistakes by planning or/and execution of diaphragm walls, which cause the creation of defects in diaphragm walls.

In order to prevent such defects in diaphragm walls, the quality control during the construction phase and testing the completed works prior to the beginning of the excavation have to be carried out comprehensively.

By construction of diaphragm walls, the occurrence of insignificant imperfections is common. In such cases, it is important to assess, whether the imperfections should be considered as a normal nonsignificant imperfection, that needs no extra treatment or it is a serious defect, which necessarily require a repairing work.

Such assessments are not easy. They need many experiences and knowledge. In order to support assessments in such situations, applying of numerical methods is one of the common ways nowadays. Numerical simulations have been developed rapidly in the last decades and now the simulation of very complicated problems can be done easily with the aid of powerful computers.

In the present study, the numerical simulation of defects in diaphragm walls is investigated. For this purpose, a meshless numerical method, called Smoothed particle hydrodynamics, is applied. The fundamental rules and formulation of this technique are described in the capitals 3 and 4. Based on this approach, a Fortran-code is developed. In order to validate the code, some benchmark problems and carried-out experiments are simulated with the developed code in the capital 5. In this capital, the problems with dry soil or with saturated soil with seepage forces as failure process of dry granular materials with various shapes, collapse of a granular column into water and hydraulic heave are considered. All these problems are almost the problems with high deformation, which are complicated to model with the common grid-based methods. With comparing the results of simulations and experiments, it can be easily realized that the results of simulation with SPH-method match very good with the chosen benchmark problems. Therefore, the code is validated in this way.

It should be noted that, the illustrating the quantitative results in the SPH method is difficult. Because of the continuous changing the results between the neighboring particles, the illustrating the quantitative results for each particle cannot be done with a good accuracy. On the other hand, the results of the velocity and positions of each particle can be shown with a very high accuracy and very good agreement compared to the experiment’s results.

In order to investigate the ability and capacity of the SPH-method to simulate the geotechnical problems, further geotechnical problems in the capital 6 are modelled. These problems as failure process in a silo, excavation by a water jet and overflooded embankment are complicated geotechnical problems with large deformation and mixture of soil-water materials. The results of these problems are rational and in accordance with the known physical laws of geotechnics.

After validation of the developed code and modelling the complicated geotechnical problems and achieving good results, as the final problem in capital 7, the defect in the diaphragm wall is considered. For this problem, two model based on the carried-out experiments in the Institute of Geo Engineering in the Clausthal University of Technology are simulated. The considered geometry and applied parameters in the experiments are chosen according to the diaphragm wall in the Cologne Archive and with considering a scale factor of 1:7. For the simulation of defect in the diaphragm wall, an opening is considered in the middle Wall-Element. In order to produce the accurate pore water pressure in the model, water level is assumed in the numerical model in accordance with the results of the pore water pressure measurement of the installed sensors, which are located in the left side of the opening. The permeability of soil is chosen as well the same as the used material in the experiment. After running the model, the results of the simulations compared with the experiments. It can be observed that the results of both models are good and in a good agreement with the experiments.

As conclusion, it can be pointed out that SPH method is a robust and suitable method for simulating the behavior of soil and water as well as the interaction between water and soil especially in geotechnical problems with large deformation and post-failure. Moreover, this method is able to simulate the defects in diaphragm walls especially with high groundwater level and can be applied well as a tool to support the assessment of the imperfections in diaphragm walls.

Bibliography

Adami, S., Hu, X., & Adams, N. (2012). A generalized wall boundary condition for smoothed particle hydrodynamics. *Journal of Computational Physics 231,* 7057-7075. doi:https://doi.org/10.1016/j.jcp.2012.05.005

Alejano, L., & Bobet, A. (2012). Drucker–Prager Criterion. *Rock Mech Rock Eng 45*, 995–999. doi:10.1007/s00603-012-0278-2

Alipour, A., & Eslami, A. (2019). Design adaptations in a large and deep urban excavation: Case study. *Journal of Rock Mechanics and Geotechnical Engineering 11*, pp. 389-399. doi:https://doi.org/10.1016/j.jrmge.2018.08.014

Allen, M. (2004). Introduction to Molecular Dynamics Simulation. *Computational Soft Matter: From Synthetic Polymers to Proteins, NIC Series, Vol. 23*, pp. 1-28.

ASTM D7949-14. (2016). *www.astm.org*. Retrieved from https://www.astm.org/d7949-14.html

Aulbach, B., & Ziegler, M. (2014). Versagensform und Nachweisformat beim hydraulischen Grundbruch –Plädoyer für den Terzaghi-Körper. *geotechnik 37, Heft 1*, S. 6-18. doi:10.1002/gete.201300020

Aulbach, B., Ziegler, M., & Schüttrumpf, H. (2013). Design Aid for the Verification of Resistance to Failure by Hydraulic Heave. *Procedia Engineering 57*, pp. 113-119. doi:10.1016/j.proeng.2013.04.017

Bagui, S., Puri, S., & Subbiah, K. (2020). Cross hole sonic test results for analysis of pile load test. *Advances in Bridge Engineering 1*. doi:https://doi.org/10.1186/s43251-020-00017-4

Beckhaus, K., Larisch, M., Alehossein, H., Northey, S., Ney, P., Lucas, G., & Vanderstaay, L. (2011). New Approach for Tremie Concrete used for Deep Foundations. *Concrete Institute of Australia*.

Beeman, D. (1976). Some Multistep Methods for Use in Molecular Dynamics Calculations. *Journal of Computational Physics 20*, 130-139. doi:DOI:10.1016/0021-9991(76)90059-0

Boley, C. (2019). *Handbuch Geotechnik, Grundlagen – Anwendungen – Praxiserfahrungen.* Springer Vieweg.

Brown, D., Turner, J., Castelli, R., & Loehr, E. (2018). *FHWA NHI-18-024, Drilled Shafts: Construction Proceduresand Design Methods.* U.S. Department of Transportation, Federal Highway Administration. doi:https://danbrownandassociates.com/wp-content/uploads/2020/02/GEC10-Drilled-Shaft-Final-10-5-18.pdf

Bui, H. H., Sako, K., & Fukagawa, R. (2007). Numerical simulation of soil–water interaction using smoothed particle hydrodynamics (SPH) method. *Journal of Terramechanics 44*, pp. 339-346. doi:https://doi.org/10.1016/j.jterra.2007.10.003

Bui, H., & Fukagawa, R. (2013). An improved SPH method for saturated soils and its application to investigate the mechanisms of embankment failure: Case of hydrostatic pore-water pressure. *International Journal for numerical and analytical methods in geomechanics*, pp. 31–50. doi:10.1002/nag.1084

Bui, H., Fukagawa, R., Sako, K., & Ohno, S. (2008). Lagrangian meshfree particles method (SPH) for large deformation and failure flows of geomaterial using elastic–plastic soil constitutive model. *International Journal for Numerical and Analytical Methods in Geomechanics 32*, pp. 1537–1570. doi: https://doi.org/10.1002/nag.688

Bui, H., Fukagawa, R., Sako, K., & Wells, J. (2009). Numerical Simulation of Granular Materials Based on Smoothed Particle Hydrodynamics (SPH). *AIP Conference Proceedings 1145*, pp. 575-578. doi:https://doi.org/10.1063/1.3179991

Bui, H., Fukagawa, R., Sako, K., & Wells, J. (2011). Slope stability analysis and discontinuous slope failure simulation by elasto-plastic smoothed particle hydrodynamics (SPH). *Géotechnique Volume 61 Issue 7*, pp. 565-574. doi:https://doi.org/10.1680/geot.9.P.046

Bui, H., Kodikara, J., Bouazza, A., Haque, A., & Ranjith, P. (2014). A novel computational approach for large deformation and post-failure analyses of segmental retaining wall systems. *International Journal for numerical and analytical methods in geomechanics*, pp. 1321–1340. doi:10.1002/nag.2253

Bui, H., Kodikara, J., Bouazza, A., Haque, A., & Ranjith, P. (2014). A novel computational approach for large deformation and post-failure analyses of segmental retaining wall systems. *International Journal for Numerical and Analytical Methods in Geomechanics 38*, pp. 1321–1340. doi:10.1002/nag.2253

Calin, N., Radu, C., & Bica, I. (2017). Dewatering system of a deep of excavation in urban area - Bucharest case study. *Procedia Engineering 209*, pp. 210–215. doi:10.1016/j.proeng.2017.11.149

Chai, J., Ni, J., Ding, W., Qiao, Y., & Lu, X. (2021). Deep excavation in under-consolidated clayey deposit. *Underground Space 6*, pp. 455–468. doi:https://doi.org/10.1016/j.undsp.2020.08.001

Chang, T.-J., Kao, H.-M., Chang, K.-H., & Hsu, M.-H. (2011, September). Numerical simulation of shallow-water dam break flows in open channels using smoothed particle hydrodynamics. *Journal of Hydrology*, pp. 408: 78-90. doi:https://doi.org/10.1016/j.jhydrol.2011.07.023

Chen, J.-Y., Lien, F.-S., Peng, C., & Yee, E. (2020). GPU-accelerated smoothed particle hydrodynamics modeling of granular flow. *Powder Technology 359*, pp. 94-106. doi:10.1016/j.powtec.2019.10.017

Chen, W.-F., & Mizuno, E. (1990). *Nonlinear analysis in soil mechanics : theory and implementation.* Amsterdam ; New York : Elsevier.

Chow, A., Rogers, B., Lind, S., & Stansby, P. (2018). Incompressible SPH (ISPH) with fast Poisson solver on a GPU. *Computer Physics Communications 226*, pp. 81-103. doi:https://doi.org/10.1016/j.cpc.2018.01.005

Civil Engineering RWTH Aachen University_youtube. (07. December 2016). *https://www.youtube.com*. Von https://www.youtube.com/watch?v=ZQvtz3KjSvw abgerufen

Daghighi, Sammy;. (2019). *Cross-hole Sonic Logging*. Retrieved from www.twininginc.com: https://www.twininginc.com/cross-hole-sonic-logging/

Daghighi, Sammy;. (2019). *Cross-hole Sonic Logging*. Retrieved from www.twininginc.com: https://www.twininginc.com/cross-hole-sonic-logging/

Dávalos, C., Cante, J., Hernández, J., & Oliver, J. (2015). On the numerical modeling of granular material flows via the Particle Finite Element Method (PFEM). *International Journal of Solids and Structures 71*, pp. 99-125. doi:https://doi.org/10.1016/j.ijsolstr.2015.06.013

Domínguez, J., Crespo, A., Gómez-Gesteira, M., & Marongiu, J. (2010). Neighbour lists in smoothed particle hydrodynamics. *International Journal for numerical methods in Fluids 67*, pp. 2026-2042. doi:10.1002/fld.2481

Drucker, D., & Prager, W. (1952). Soil mechanics and plastic analysis or limit design. *Quarterly of Applied Mathematics 10*, 157-165.

EFFC/DFI Guide. (2018). Guide to Tremie Concrete for Deep Foundations / By the joint EFFC/DFI Concrete Task Group. *European Federation of Foundation Contractors*.

El Zein, A., Vanhove, Y., Djelal, C., Madec, O., & Gotteland, P. (2021). Evaluation of internal bleeding in concrete foundation from the Terzaghi's effective stress postulate. *Materials and Structures 54:231*. doi:https://doi.org/10.1617/s11527-021-01828-1(0123456789().,-volV() 0123458697().,-volV)

Emker, M. (2020). *Weiterentwicklung eines Versuchsstandes zur systematischen Untersuchung von möglichen Fehlstellen in Dichtwänden.*

Encyclopedia of Ocean Sciences (Second Edition). (2001). Retrieved from https://www.sciencedirect.com/topics/earth-and-planetary-sciences/thermistor

Ewald, K., & Schneider, N. (2015). Vermeidung von Schäden an Schlitzwandfugen durch den Einsatz geeigneter Qualitätssicherungssysteme. *Bautechnik 92, Heft 9*. doi:10.1002 / bate.201500047

Fa´vero Neto, A., & Borja, R. (2018). Continuum hydrodynamics of dry granular flows employing multiplicative elastoplasticity. *Acta Geotechnica 13*, pp. 1027–1040. doi:https://doi.org/10.1007/s11440-018-0700-3

Fern, E., & Soga, K. (2017). Granular Column Collapse of Wet Sand. *Procedia Engineering 175*, pp. 14-20. doi:https://doi.org/10.1016/j.proeng.2017.01.005

Fourtakas, G., & Rogers, B. (2016, June). Modelling multi-phase liquid-sediment scour and resuspension induced by rapid flows using Smoothed Particle Hydrodynamics (SPH) accelerated with a Graphics Processing Unit (GPU). *Advances in Water Resources*, pp. 92: 186-199. doi:https://doi.org/10.1016/j.advwatres.2016.04.009

G.Panicker, P., Goel, A., & R.Iyer, H. (2015). Numerical Modeling of Advancing Wave Front in Dam Break Problem by Incompressible Navier-stokes Solver. *Aquatic Procedia*, pp. 4: 861-867. doi:https://doi.org/10.1016/j.aqpro.2015.02.108

Gholami Korzani, M. (n.d.). *www.m2clab.com*. Retrieved from https://www.m2clab.com

Gholami Korzani, M., Galindo Torres, S., William, D., & Scheuermann, A. (2014). Numerical simulation of tank discharge using smoothed particle hydrodynamics. *Applied Mechanics and Materials, Vol. 553*, pp. 168-173.

Gholami Korzani, M., Galindo-Torres, S. A., Scheuermann, A., & Williams, D. J. (2018). Smoothed Particle Hydrodynamics for investigating hydraulic and mechanical behaviour of an embankment unter action of flooding and overburden loads. *Computers and Geotechnics 94*, pp. 31-45. doi:https://doi.org/10.1016/j.compgeo.2017.08.014

Gholami Korzani, M., Galindo-Torres, S., Scheuermann, A., & J. Williams, D. (2016). Smoothed Particle Hydrodynamics into the Fluid Dynamics of Classical Problems. *Applied Mechanics and Materials 1662-7482, Vol. 846*, pp. 73-78. doi:10.4028/www.scientific.net/AMM.846.73

Gholami Korzani, M., Galindo-Torres, S., Scheuermann, A., & Williams, D. (2018). SPH approach for simulating hydro-mechanical processes with large deformations and variable permeabilities. *Acta Geotechnica 13*, pp. 303-316.

Gingold, R., & Monaghan, J. (1977). Smoothed particle hydrodynamics: theory and application to non-spherical stars. *Monthly Notices of the Royal Astronomical Society*, S. 375-389.

Gingold, R., & Monaghan, J. (1982). Kernel Estimates as a Basis for General Particle Methods in Hydrodynamics. *Journal of Computational Physics 46*, pp. 429-453.

Goeminne, E., Brutin, M., Benoot, J., Couck, J., & Vos, L. (2017). Measuring vertical strains and temperature with fiber optics in diaphragm walls. *SMAR 2017-Forth Conference on Smart Monitoring, Assessment and Rehabilitation of Civil Structures*.

Gong, K., Shao, S., Liu, H., Wang, B., & Tan, S.-K. (2016, August). Two-phase SPH simulation of fluid–structure interactions. *Journal of Fluids and Structures*, pp. 65: 155-179. doi:https://doi.org/10.1016/j.jfluidstructs.2016.05.012

Grabe, J., & Stefanova, B. (geotechnik 37 (2014), Heft 3). *Numerical modeling of saturated soils, based on Smoothed Particle Hydrodynamics (SPH), Part 1: Seepage analysis.* Berlin: Ernst & Sohn Verlag für Architektur und technische Wissenschaften GmbH & Co. KG. doi:10.1002/gete.201300024

Grabe, J., & Stefanova, B. (geotechnik 38 (2015), Heft 3). *Numerical modeling of saturated soils based on smoothed particle hydrodynamics (SPH), Part 2: Coupled analysis.* Berlin: Ernst & Sohn Verlag für Architektur und technische Wissenschaften GmbH & Co. KG. doi:10.1002/gete.201400027

Hajali, M., & Abishdid, C. (2014). Cross-Hole Sonic Logging and Frequency Tomography Analysis of Drilled Shaft Foundations to Better Evaluate Anomalies Locations. *The Journal of the Deep Foundations Institute, Volume 8, Issue 1*. doi:10.1179/TBC14Z.0000000001

Hill, M., & Thorp, A. (2021). Use of tremie concrete in New Zealand deep foundations. *21st NZGS Symposium*.

hmagrp.com. (2021). Retrieved from https://hmagrp.com/wp-content/uploads/2021/04/GEO-DS-0082-Thermistor-Strings.pdf

Holmes, D., Williams, J., & Tilke, P. (2011). Smooth particle hydrodynamics simulations of low Reynolds number flows through porous media. *International Journal for Numerical Analytical Methods in Geomechanics 35*, 419–437. doi:10.1002/nag.898

https://bauerfoundations.com. (n.d.). Retrieved from https://bauerfoundations.com/en/construction_methods/diaphragm_wall/

https://en-academic.com. (n.d.). Retrieved from https://en-academic.com/dic.nsf/enwiki/4730467

https://fugeninspektor.de/. (n.d.).

https://olsoninstruments.com. (n.d.). Retrieved from https://www.pcte.com.au/crosshole-sonic-logging-and-crosshole-tomography

https://olsoninstruments.com. (n.d.). Retrieved from https://olsoninstruments.com/wp-content/uploads/CSL_Catalog_Flyer.pdf

https://railsystem.net. (n.d.). Retrieved from https://railsystem.net/diaphragm-wall-construction/

https://video.bauer.de. (n.d.). Retrieved from BAUER Gruppe: https://video.bauer.de/bst/flippingbook/BAUER-Diaphragm-and-Cut-off%20Walls/files/assets/common/downloads_98cd748f/publication.pdf

https://www.dw.com. (03. 03 2019). Von https://www.dw.com/de/k%C3%B6ln-erinnert-an-stadtarchiv-einsturz/a-47758700 abgerufen

https://www.eiengineering.com.au. (n.d.). Retrieved from https://www.eiengineering.com.au/2017/02/23/mechanical-vs-hydraulic-excavator-grapple-whats-the-difference-infographic/

https://www.geotech.net.au. (n.d.). Retrieved from https://www.geotech.net.au/capabilities/basement-construction/diaphragm-wall.html

https://www.liebherr.com. (n.d.). Retrieved from https://www.liebherr.com/en/int/products/construction-machines/deep-foundation/methods/slurry-wall-production/hydromill-cutter/hydromill-cutter.html

Huang, Y., Dai, Z., & Zhang, W. (2014). *Geo-disaster Modeling and Analysis: An SPH-based Approach.* Springer-Verlag Berlin Heidelberg. doi:10.1007/978-3-662-44211-1

Jin, S.-Q., Zheng, X., Duan, W.-Y., & Niu, K.-N. (2015). A new boundary treatment method for smoothed particle hydrodynamics. *Procedia Engineering 126*, 655 – 659. doi:10.1016/j.proeng.2015.11.256

Jouniaux, L., Maineult, A., Naudet, V., Pessel, M., & Sailhac, P. (2009). Review of self-potential methods in hydrogeophysics. *C. R. Geoscience 341*, pp. 928–936. doi:10.1016/j.crte.2009.08.008

Kermani, E., & Qiu, T. (2020). Simulation of quasi-static axisymmetric collapse of granular columns using smoothed particle hydrodynamics and discrete element methods. *Acta Geotechnica 15*, pp. 423–437. doi:https://doi.org/10.1007/s11440-018-0707-9

Koltuk, S., & Azzam, R. (2016). Design Charts for Circular-Shaped Sheeted Excavation Pits against Seepage Failure by Heave. *Periodica polytechnica / Civil engineering 60(3)*, pp. 421-426. doi:10.3311/PPci.8522

Koltuk, S., Song, J., Iyisan, R., & Azzam, R. (2019). Seepage failure by heave in sheeted excavation pits constructed in stratified cohesionless soils. *Front. Struct. Civ. Eng. 13(6)*, pp. 1415–1431. doi:https://doi.org/10.1007/s11709-019-0565-z

Korzani, M. (n.d.). Retrieved from https://www.m2clab.com/

Lajeunesse, E., Mangeney-Castelnau, A., & Vilotte, J. (2004). Spreading of a granular mass on a horizontal plane. *Physics of Fluids 16*, pp. 2371-2381. doi:https://doi.org/10.1063/1.1736611

Li, Z., Soga, K., & Kechavarzi, C. (2018). Distributed fibre optic sensing of a deep excavation adjacent to pre-existing tunnels. *Géotechnique Letters, Volume 8 Issue 3*, 171-177. doi:https://doi.org/10.1680/jgele.18.00031

Libano, D. (2014). Sao Paulo Metro's Brooklin Station: A Hydromill Saves the Day. *Deep Foundation*.

Libersky, L., Petschek, A., Carney, T., Hipp, J., & Allahdadi, F. (1993). High Strain Lagrangian Hydrodynamics. *Journal of Computational Physics 109*, 67-75.

Liu, G., & Liu, M. (2003). *Smoothed Particle Hydrodynamics: A meshfree particle method*. Singapore: World Scientific Publishing Co. Pte. Ltd.

Liu, M., Xie, W., & Liu, G. (2005). Modeling incompressible flows using a finite particle method. *Applied Mathematical Modelling 29*, pp. 1252–1270. doi:10.1016/j.apm.2005.05.003

Lubach, A. (2010). Bentonite cavities in diaphragm walls, Case studies, process decomposition, scenario analysis and laboratory experiments. *MSc Thesis*.

Lucy, L. (1977, December). A numerical approach to the testing of the fission hypothesis. *Astronomical Journal*.

M. Abdelrazek, A., Kimura, I., & Shimizu, Y. (2016). Simulation of three-dimensional rapid free-surface granular flow past different types of obstructions using the SPH method. *Journal of Glaciology, 62(232)*, pp. 335–347. doi:10.1017/jog.2016.22

Mangushev, R., Rybnov, E., Lashkova, E., & Osokin, A. (2016). Examples of the construction of deep excavation ditches in weak Soils. *Procedia Engineering 165*, pp. 673 – 681. doi:10.1016/j.proeng.2016.11.765

Mattner, K. (2018). Bachelorarbeit: Inbetriebnahme eines Modellversuchsstands zur Untersuchung des Durchbruchverhaltens in einer Fehlstelle einer Baugrubenwand. Clausthal University of Technology .

Mendez, J., Rausche, F., & Paulin, J. (2012). Quality Control of Diaphragm Walls by Crosshole Sonic Logging. *GeoCongress 2012, Oakland, California, United States* . doi:https://doi.org/10.1061/9780784412084.0045

Mirmohammadi, A., & Ketabdari, M. (2011). Numerical simulation of wave scouring beneath marine pipeline using smoothed particle hydrodynamics. *International Journal of Sediment Research 26*, pp. 331-342.

Mironov, D., Osokin, A., Loseva, E., & Kuzhelev, A. (2020). Specific features of diaphragm wall construction. *IOP Conf. Series: Materials Science and Engineering 775*. doi:10.1088/1757-899X/775/1/012051

Monaghan, J. (1989). On the Problem of Penetration in Particle Methods. *Journal of Computational Physics 82*, pp. 1-15. doi:https://doi.org/10.1016/0021-9991(89)90032-6

Monaghan, J. (1992). Smoothed Particle Hydrodynamics. *Annu. Rev. Astron. Astrophys. 30*, pp. 543-574.

Monaghan, J. (1994). Simulating Free Surface Flows with SPH. *Journal of Computational Physics 110*, pp. 399-406.

Monaghan, J. (2000). SPH without a Tensile Instability. *Journal of Computational Physics 159*, S. 290-311.

Monaghan, J. (2001). Smoothed Particle Hydrodynamics Code Basics. *Journal of the Korean Astronomical Society*, pp. 203-207.

Monaghan, J. (2012). Smoothed Particle Hydrodynamics and Its Diverse Applications. *The Annual Review of Fluid Mechanics 44*, pp. 323–46. doi:10.1146/annurev-fluid-120710-101220

Monaghan, J. J. (1988). An Introduction to SPH. *Computer Physics Communications 48*, pp. 89-96.

Monaghan, J., & Gingold, R. (1983). Shock Simulation by the Particle Method SPH. *Journal of computational physics*, pp. 374-389.

Monaghan, J., & Kocharyan, A. (1995). SPH simulation of multi-phase flow. *Computer Physics Communications*, pp. 225-235.

Morris, J., & Monaghan, J. (1997). A Switch to Reduce SPH Viscosity. *Journal of Computational Physics 136*, pp. 41-50.

Nguyen, C., Bui, H., & Fukagawa, R. (2013). Two-dimensional numerical modelling of Modular-block soil retaining wall collapse using meshfree method. *Int. J. of GEOMATE, Vol. 5, No. 1 (Sl. No. 9)*, pp. 647-652.

Nguyen, C., Nguyen, C., Bui, H., Nguyen, G., & Fukagawa, R. (2016). A new SPH-based approach to simulation of granularflows using viscous damping and stress regularisation. *Landslides 14*, 69–81. doi:DOI 10.1007/s10346-016-0681-y

Nonoyama, H., Moriguchi, S., Sawada, K., & Yashima, A. (2015). Slope stability analysis using smoothed particle hydrodynamics (SPH) method. *Soils and Foundations 55(2)*, 458-470. doi:10.1016/j.sandf.2015.02.019

P. Morris, J., J. Fox, P., & Zhu, Y. (1997). Modeling Low Reynolds Number Incompressible Flows Using SPH. *Journal of computational physics 136*, pp. 214–226.

Pan, K., Pramanik, R., Jones, B., Douillet-Grellier, T., Albaiz, A., & Williams, J. (2016). Development of fluid-solid coupling for the study of hydraulic fracturing using SPH. *11th international SPHERIC workshop*. Munich, Germany.

Peng, C., Wang, S., Wu, W., Yu, H.-s., Wang, C., & Chen, J.-y. (2019). LOQUAT: an open-source GPU-accelerated SPH solver for geotechnical modeling. *Acta Geotechnica 14*, pp. 1269–1287. doi:https://doi.org/10.1007/s11440-019-00839-1

Peng, C., Wu, W., Yu, H.-s., & Wang, C. (2015). A SPH approach for large deformation analysis with hypoplastic constitutive model. *Acta Geotechnica*, 10: 703–717. doi:10.1007/s11440-015-0399-3

Peng, C., Xu, G., Wu, W., Yu, H.-s., & Wang, C. (2017). Multiphase SPH modeling of free surface flow in porous media with variable porosity. *Computers and*

Geotechnics, pp. 81: 239-248. doi:https://doi.org/10.1016/j.compgeo.2016.08.022

Pereira, G. G., Prakash, M., & Cleary, P. W. (2011). SPH modelling of fluid at the grain level in a porous medium. *Applied Mathematical Modelling 35*, pp. 1666–1675. doi:10.1016/j.apm.2010.09.043

Qianchen Sun, J., & Z.E.B. Elshafie, M. (2019). A New Thermal Integrity Method for Pile Anomaly Detection. *Conference: Structural Health Monitoring*. doi:10.12783/shm2019/32405

Randles, P., & Libersky, L. (1996). Smoothed Particle Hydrodynamics: Some recent improvements and applications. *Computer Methods in Applied Mechanics and Engineering 139*, pp. 375-408. doi:https://doi.org/10.1016/S0045-7825(96)01090-0

Rondon, L., Pouliquen, O., & Aussillous, P. (2011). Granular collapse in a fluid: Role of the initial volume fraction. *Physics of Fluids 23 (073301)*, pp. 1-7. doi:10.1063/1.3594200

Roselli, R., Vernengo, G., Brizzolara, S., & Guercio, R. (2019, March). SPH simulation of periodic wave breaking in the surf zone - A detailed fluid dynamic validation. *Ocean Engineering*, pp. 176: 20-30. doi:https://doi.org/10.1016/j.oceaneng.2019.02.013

Schneider, N. (2013). A New Method of Quality Control for Construction Joints in Diaphragm Walls. (www.fugeninspektor.de, Ed.)

Schober, P., Boley, C., & Odenwald, B. (2011). *Hydraulic Heave Safety at Excavations with Surcharge Filters.* ISGSR 2011 - Vogt, Schuppener, Straub & Bräu (eds) - © 2011 Bundesanstalt für Wasserbau.

Spruit, R., Hopman, V., & van Tol, A. (2012). Detection of imperfections in diaphragm walls with geophysical measurements. *Geotechnical Aspects of Underground Construction in Soft Ground*.

Spruit, R., Hopman, V., van Tol, F., & Broere, W. (2011). Detecting defects in diaphragm walls prior to excavation. *Conference: 8th International Symposium on Field Measurements in GeoMechanics (FMGM), Berlin (Germany)*.

Spruit, R., van Tol, F., Broere, W., Doornenbal, P., & Hopman, V. (2017). Distributed temperature sensing applied during diaphragm wall construction. *Canadian Geotechnical Journal 54*, pp. 219-233. doi:https://doi.org/10.1139/cgj-2014-0522

Spruit, R., van Tol, F., Broere, W., Slob, E., & Niederleithinger, E. (2014). Detection of anomalies in diaphragm walls with crosshole sonic logging. *Canadian Geotechnical Journal 51*. doi:https://doi.org/10.1139/cgj-2013-0204

Staron, L., & Hinch, E. (2005). Study of the collapse of granular columns using two-dimensional discrete-grain simulation. *J. Fluid Mech. 545*, pp. 1-27. doi:doi:10.1017/S0022112005006415

Stellingwerf, R., & Wingate, C. (1993). Impact Modeling with Smooth Particle Hydrodynamics. *Int. J. Impact Engng Vol. 14*, pp. 707-718.

Swegle, J., Hicks, D., & Attaway, S. (1995). Smoothed Particle Hydrodynamics Stability Analysis. *Journal of Computational Physics 116(1)*, 123-134. doi:10.1006/jcph.1995.1010

Takeda, H., M. Miyama, S., & Sekiya, M. (1994). Numerical Simulation of Viscous Flow by Smoothed Particle Hydrodynamics. *Progress of Theoretical Physics, Vol. 92, No.5*.

Tartakovsky, A., Trask, N., Pan, K., Jones, B., Pan, W., & Williams, J. (2016). Smoothed particle hydrodynamics and its applications for multiphase flow and reactive transport in porous media. *Comput Geosci 20*, 807–834. doi:10.1007/s10596-015-9468-9

Thompson, E., & Huppert, H. (2007). Granular column collapses: further experimental results. *J. Fluid Mech. 575*, pp. 177–186. doi:10.1017/S0022112006004563

Tomczak, U., & Mielczarek, Ł. (2016). Two-level Structure for Tram and Road Traffic in the Centre of City – Lodz in Poland. *Procedia Engineering, Volume 143*, pp. 574–581. doi:10.1016/j.proeng.2016.06.075

Viccione, G., Bovolin, V., & Pugliese Carratelli, E. (2008). Defining and optimizing algorithms for neighbouring particle identification in SPH fluid simulations. *International Journal for Numerical Methods in Fluids 58*, pp. 625-638. doi:https://doi.org/10.1002/fld.1761

W. Cleary, P., & J. Monaghan, J. (1999). Conduction Modelling Using Smoothed Particle Hydrodynamics. *Journal of Computational Physics*, pp. 148: 227–264.

Wang, C., Wang, Y., Peng, C., & Meng, X. (2017). Dilatancy and compaction effects on the submerged granular column collapse. *Physics of Fluids 29 (103307)*, pp. 1-10. doi:https://doi.org/10.1063/1.4986502

Wang, C., Wang, Y., Peng, C., & Meng, X. (2017). Dilatancy and compaction effects on the submerged granular column collapse. *Physics of Fluids 29, 103307*. doi:https://doi.org/10.1063/1.4986502

Wang, G., Riaz, A., & Balachandran, B. (2020). Smooth particle hydrodynamics studies of wet granular column collapses. *Acta Geotechnica 15*, pp. 1205–1217. doi:https://doi.org/10.1007/s11440-019-00828-4

Wang, J., & Chan, D. (2014). Frictional contact algorithms in SPH for the simulation of soil–structure interaction. *International Journal for Numerical and Analytical Methods in Geomechanics 38*, pp. 747–770. doi:10.1002/nag.2233

Wen, H., Ren, B., & Wang, G. (2018, June). 3D SPH porous flow model for wave interaction with permeable structures. *Applied Ocean Research*, pp. 75: 223-233. doi:https://doi.org/10.1016/j.apor.2018.04.003

Weng, Q., Xu, Z., Wu, Z., & Liu, R. (2016). Design and performance of the deep excavation of a substation constructed by top-down method in Shanghai soft soils. *Procedia Engineering 165*, pp. 682 – 694. doi:10.1016/j.proeng.2016.11.766

White, B., Nagy, M., & Allin, R. (2008). Comparing cross-hole sonic logging and low-strain integrity testing results.

Winkler, D., Rezavand, M., & Rauch, W. (2018). Neighbour lists for smoothed particle hydrodynamics on GPUs. *Computer Physics Communications 225*, pp. 140–148. doi:https://doi.org/10.1016/j.cpc.2017.12.014

Wu, Q., An, Y., & Liu, Q.-q. (2015). SPH-Based Simulations for Slope Failure Considering Soil-Rock Interaction. *Procedia Engineering, Volume 102*, pp. 1842-1849. doi:https://doi.org/10.1016/j.proeng.2015.01.322

www.balfourbeatty.com. (n.d.). Retrieved from https://www.balfourbeatty.com/media/29507/diaphragm-wall.pdf

www.bauer.de. (n.d.). Retrieved from BAUER Gruppe: https://www.bauer.de/export/shared/documents/pdf/bma/datenblatter/BC_trench/BC_Trench_Cutter_Systems_EN_905_853_2.pdf

www.brasfond.com. (n.d.). Retrieved from http://www.brasfond.com/hidrofresa.html

www.casagrandegroup.com. (n.d.). *S.p.A., Casagrande*. Retrieved from https://www.casagrandegroup.com/diaphragm-wall/hydromills/fd60-hydromill/

www.geokon.com. (n.d.). Retrieved from https://www.geokon.com/3800

www.geosense.co.uk. (n.d.). Retrieved from https://www.geosense.co.uk/products/thermistors/

www.gkmconsultants.com. (2017). Von https://www.gkmconsultants.com/assets/documents/instruments/pdf/3800_thermistors_3810_and_3810a_thermistor_strings-rev-d-6%20copy(1).pdf abgerufen

www.grlengineers.com. (n.d.). *GRL Engineers, Inc.* Retrieved from https://www.grlengineers.com/services/shape/

www.jointinspector.com. (n.d.). *www.jointinspector.com*. Retrieved from https://www.jointinspector.com/diaphragm-walls/joints/

www.liebherr.com. (n.d.). Retrieved from https://www.liebherr.com/en/int/products/construction-machines/deep-foundation/methods/slurry-wall-production/hydromill-cutter/hydromill-cutter.html

www.model-co.com. (n.d.). Retrieved from https://www.model-co.com/en/foundation_equipment/diaphragm_wall/mechanical_grabs/cml300_diaphragm_wall_mechanical_grab.asp

www.pcte.com.au. (n.d.). Retrieved from https://www.pcte.com.au/crosshole-sonic-logging-and-crosshole-tomography

www.pile.com. (n.d.). Retrieved from https://www.pile.com/products/shape-2

www.sb-canada.com. (n.d.). (Canada, Soletanche Bachy) Retrieved from https://www.sb-canada.com/techniques/special-techniques/slurry-diaphragm-walls/

www.stadt-koeln.de. (2009). Retrieved from https://www.stadt-koeln.de/artikel/07168/index.html

Yang, C., Liu, S., Ding, E., Yang, H., & Xie, J. (2020). Evaluation of Electrical Resistivity for Non-destructive Seepage Detection on an Urban Underground Diaphragm Wall. *Journal of Environmental and Engineering Geophysics, Volume 25, Issue 1*. doi:https://doi.org/10.2113/JEEG18-091

Ye, Z., & Zhao, X. (2017, May). Investigation of water-water interface in dam break flow with a wet bed. *Journal of Hydrology*, pp. 548: 104-120. doi:https://doi.org/10.1016/j.jhydrol.2017.02.055

You, Y., Yan, C., Xu, B., Liu, S., & Che, C. (2018). Optimization of dewatering schemes for a deep foundation pit near the Yangtze River, China. *Journal of Rock Mechanics and Geotechnical Engineering 10*, pp. 555-566. doi:https://doi.org/10.1016/j.jrmge.2018.02.002

Nomenclature

Abbreviations and acronyms

CCTV	closed-circuit television method
CFL	Courant-Friedrichs-Lewy
CSL	Crosshole Sonic Logging
DFI	Deep Foundations Institute
DFOS	Distributed fiber optic sensing
EFFC	European Federation of Foundation Contractors
FDM	Finite Difference Methods
FEM	Finite Element Method
FVM	Finite Volume Method
PIV	Particle Image Velocimetry
PVC	Polyvinyl chloride
SHAPE	Shaft Area Profile Evaluator
SPH	Smoothed Particle Hydrodynamics
TIP	Thermal Integrity Profiling
VMAs	viscosity modifying admixtures
WCSPH	weak compressibility Smoothed Particle Hydrodynamics
XSPH	extended Smoothed Particle Hydrodynamics

Latin Variables or Constants

c	cohesion of soil
c_0	speed of sound
$\overline{c_{ij}}$	average of the sound speed of particle i and j
D	problem dependent parameter for repulsive force method
dt	time step
E	Young's modulus
f^{α}	external force
F_a^{α}	body force applied on the particle a in the direction α
g	gravity force
g_a	external force
g_p	plastic potential function
G	shear modulus
h	smoothing length
I_1	first invariants of the stress tensor
J_2	second invariants of the stress tensor
k	constant number related to the kernel function to define the effective area
k_c	Drucker-Prager's constant
k_s	soil permeability
K	bulk modulus
K_0	earth pressure coefficient
m	mass of a particle
n	porosity of soil
N	number of the neighboring particles of each particle
P	isotropic pressure
P_a	pressure at particle a
P_1 and P_2	constant numbers for repulsive force method
q	number of dimensions of kernel function
r_{ij}	distance between particle i and its neighboring particle j

$s^{\alpha\beta}$	deviatoric shear stress
v_i	velocity of the particle i
v^{α}	velocity component
V_a	velocity of particle a
V_{max}	maximum possible occurring velocity of the particles in whole domain
$W(x-x',h)$	smoothing kernel function
$Y(I_1,J_2)$	yield function

Greek Variables or Constants

α	initial aspect ratio
α_{ϕ}	Drucker-Prager's constant
α_{ψ}	dilatancy factor
β_{max}	constant number for fixed boundary particles
γ	constant number in equation of state
γ_w	unit weight of water
$\delta(x-x')$	Delta function
Δt	time step
Δx	initial spacing between particles
$\dot{\varepsilon}^{\alpha\beta}$	shear strain rate
$\varepsilon^{\gamma\gamma}$	volumetric strain
$\dot{\varepsilon}^{\gamma\gamma}$	summation of the three normal strain-rate components
ζ	a safety parameter in Verlet method
η^2	constant number for artificial viscosity method
λ	plastic multiplier
μ	dynamic viscosity
ν	Poisson's ratio
ν_k	kinematic viscosity.
ρ_0	reference density
ρ_a	density of particle a

$\sigma^{\alpha\beta}$	total stress tensor
$\sigma^{\gamma\gamma}$	summation of stress components in x, y and z direction
$\dot{\hat{\sigma}}^{\alpha\beta}$	Jaumann stress rate
$\tau^{\alpha\beta}$	viscous stress
ϕ	internal friction angle
ψ	dilatancy angle
χ	CFL coefficient
ω	constant factor of kernel function

Dimensionless Characteristic Number, Indices

$\Delta V/V$	volumetric strain
∇	gradient
X	coordinate axis in the Cartesian coordinate system
Y	coordinate axis in the Cartesian coordinate system